Non-Destructive Evaluation of Impact Damage in Carbon Fibre Reinforced Polymer Using Infrared Thermography and Shearography

by

Ali KHADEMI FAR

THESIS PRESENTED TO ÉCOLE DE TECHNOLOGIE SUPÉRIEURE
IN PARTIAL FULFILLMENT FOR A MASTER'S DEGREE
WITH THESIS IN MECHANICAL ENGINEERING
M.A.Sc

MONTREAL, June 23, 2020

ÉCOLE DE TECHNOLOGIE SUPÉRIEURE
UNIVERSITÉ DU QUÉBEC

BOARD OF EXAMINERS

THIS THESIS HAS BEEN EVALUATED

BY THE FOLLOWING BOARD OF EXAMINERS

Mr. Martin Viens, Thesis Supervisor
Department of mechanical engineering at École de Technologie Supérieure

Mr. Hakim Bendada, Thesis Co-supervisor
Department of Electrical and Computer Engineering at Laval University

Mr. François Blanchard, President of the Board of Examiners
Department of Electrical and Computer Engineering at École de Technologie Supérieure

Jean-François Chatelain, Member of the jury
Department of mechanical engineering at École de Technologie Supérieure

Mr. Xavier Maldague, External Evaluator
Department of Electrical and Computer Engineering at Laval University

THIS THESIS WAS PRESENTED AND DEFENDED

IN THE PRESENCE OF A BOARD OF EXAMINERS AND PUBLIC

May 26, 2020

AT ÉCOLE DE TECHNOLOGIE SUPÉRIEURE

ACKNOWLEDGMENT

I would like to express my sincerest gratitude to my advisor, Dr. Martin Viens, and I am very thankful to him for guiding me during this research. This work would not have been possible without his advice and supports. He gave me lots of freedom to explore the problems that interested me while providing me with the direction that I needed. This thesis is a dedication to him for the willingly supports.

I am grateful for the supervising of Dr. Hakim Bendada. The success of this project would not have been possible without his continued contribution and supports.

Also, I would like to acknowledge *oNDuTy!* Canada team. The great committee for NDT research and development in Canada, for giving me this opportunity and supporting me emotionally and financially during my M.Sc. degree study. I wish to acknowledge Dr. Celemte Ibarrac, the coordinator, Dr. Xavier Maldague, the director of the program, and the other faculty members and students.

Also, I would like to acknowledge our research partner Centre Technologique en Aérospatiale (CTA) and its staff, Louis Daniel, Julian Walter and Olivier Ares, for giving me this opportunity and supporting me technically during the work.

The support of the Mechanical department's faculty and staff at ETS is appreciated. It is an honour for me to get my Master's degree from this great university.

This thesis is proudly dedicated to:

my beautiful wife, Mozhdeh,

for her endless love, support and encouragement

,

my mother, Mahvash B. Ahmadi

and my father Ardeshir K. Far

who have supported me through every step of my journey

Évaluation non destructive des dommages par impact dans un polymère renforcé de fibres de carbone par thermographie infrarouge et shearographie

Ali KHADEMI FAR

Résumé

L'impact à faible vitesse dans les polymères renforcés de fibres de carbone (PRFC) est reconnu comme une cause majeure de défaillance dans les structures aérospatiales. Pour évaluer les défauts dans les PRFC, des contrôles non destructifs (CND) sont utilisés. L'objectif de cette thèse est de comparer les caractéristiques et le potentiel des différentes méthodes de CND pour révéler et dimensionner les dommages par impact dans des panneaux de PRFC. Pour évaluer de tels dommages, des contrôles par ultrasons, thermographie et shearographie ont été effectués. Ces méthodes ont été appliquées pour évaluer les dommages résultant de différents niveaux d'impact sur des composites stratifiés. La taille des dommages est mesurée à l'aide de contrôle par ultrasons. Sur la base des mesures ultrasonores, l'aptitude de la thermographie et de la shearographie à caractériser quantitativement les défauts est étudiée. Les essais expérimentaux montrent que la thermographie infrarouge et la shearographie sont capables d'évaluer quantitativement l'endommagement. Par exemple, dans ces expériences, la shearographie présente une corrélation empirique entre la densité des franges et le niveau d'énergie des impacts. Outre les essais expérimentaux, des simulations par éléments finis ont été effectuées. Ainsi, grâce à des essais virtuels, un modèle numérique permet d'évaluer les performances des méthodes de détection étudiées.

Mots-clés: technique de thermographie infrarouge, contrôle par ultrasons, shearographie, PRFC, dommage par impact, contrôle non destructif, simulation par éléments finis

Non-destructive evaluation of impact damage in carbon fibre reinforced polymer using infrared thermography and shearography

Ali KHADEMI FAR

ABSTRACT

Low-velocity impact in carbon fibre reinforced polymer (CFRP) is known as a major reason for failure in aerospace structures. To evaluate defects in CFRPs, nondestructive testing (NDT) is used. The objective of the thesis is to compare the features and abilities of different NDT methods to reveal and size impact damages in CFRP panels. To assess the damages, ultrasonic testing, thermography, and shearography are conducted. These methods are applied to evaluate damages for different impact levels on composite laminates. The size of the damages is measured using ultrasonic testing. Based on the ultrasound measurements, the defect quantifying abilities of thermography and shearography are investigated. The tests show that infrared thermography and shearography are able to quantify the damages. In the experiments, shearography presents a qualitative correlation between fringe density and level of impact energy. Besides the experimental testing, finite element simulation is used. The simulation can evaluate the methods' detecting performances through the virtual test.

Keywords: infrared thermography technique, ultrasonic testing, shearography, CFRP, impact damage, non-destructive testing, finite element simulation

TABLE OF CONTENTS

LIST OF TABLES

LIST OF FIGURES

Page

LIST OF ABBREVIATIONS

LVID	Low-velocity impact damage
HVID	high-velocity impact damage
BVID	Barely visible impact damage
WWII	World War II
IRT	Infrared thermography testing
VT	Visual testing
UT	Ultrasonic testing
RT	Radiography testing
LPT	Liquid penetrant testing
MPT	Magnetic particle testing
ECT	Eddy-current testing
MIA	Mechanical impedance analysis
SMT	Strain monitoring testing
AET	Acoustic emission testing
TOF	Time-of-Flight
FOD	Foreign object damages
FFT	Fast Fourier Transform
DFT	Discrete Fourier Transform
PT	Pulse thermography
ERT	Early Recorded Thermogram
LRT	Last Recorded Thermogram

LIST OF SYMBOLS

Z_1	CFRP acoustic impedance, [$kg/\mathrm{m}^2\mathrm{s}$]
Z_2	Water acoustic impedance, [$kg/\mathrm{m}^2\mathrm{s}$]
NF	Near field margin, [m]
$\alpha/2$	Half angle of beam spread
f	Frequency, [Hz]
D	Transducer crystal diameter, [m]
c	Sound velocity in the medium, $[m/s]$
T	Temprature, [° C, K]
mm	millimetre
J	Joules
$N_{\lambda,b}$	Spectral radiance from a blackbody
λ	Wavelength [m]
N_λ	Spectral radiance for real object
α	Diffusivity, $[m^2/s]$
ε	Emissivity
h	Planck's constant, $[J.s]$
K	Boltzmann's constant
μ	Micro
t	Time, [s]
F_n	Discrete Fourier Transform
ϕ	Phase delay, [rad]
Im	Imaginary part of Discrete Fourier Transform
Re	Real part of Discrete Fourier Transform
U	Dimensionless temperature
$w(t)$	Truncation window, [s]
u	Displacement vector

v	Displacement vector
w	Displacement vector
k	Cartesian component
Δ	Phase change, [rad]
δ	Shearig amount, $[mm]$

INTRODUCTION

0.1 Overview

Typical damage scenario in aerospace carbon fibre reinforced polymer (CFRP) components is the low-velocity impact. In most of the cases, due to no visible exterior signs, they are not detectable visually. Among the different non-destructive testing (NDT) approaches available, ultrasonic testing, infrared thermography and shearography testing have been found of practical use to detect and evaluate such internal damages. The former of these methods being in contact while the latter two being non-contact, each of them has its own abilities and weaknesses in flaw detection. On the other hand, applying a reliable NDT method to reveal a specific discontinuity needs a proper assessment of the test performance. In such a case, besides the experimental testing, mathematical simulation is used to evaluate the NDT methods since it can evaluate detecting performance through virtual tests.

0.2 Literature review

Due to the increasing use of composites instead of metallic parts in new commercial aircraft, the need for new inspection techniques has arisen in the aerospace industry. In this section, a review of these NDT methods, which are used to test CFRP components, is presented. The section is followed by a discussion of their abilities and limitations. Finally, an effort is made to review the rules related to numerical simulation in NDT.

0.3 Carbon fibre reinforced polymers

CFRP is a combination of two different materials, reinforcement and matrix. The reinforcement is long, thin and flexible fibres of carbon that provide no strength in any direction other than a tensile toughness. The matrix, made by a polymer, provides the shape, holds the fibres in place, and transfers loads between them.

Use of CFRPs is growing in the field of engineering design. Since it has a high strength to weight ratios, high stiffness, and it is corrosion-resistant, CFRP takes over the market for high-performance structures [1].

The performance of aircraft mainly depends on the weight to strength ratio of their parts. Consequently, new designs tend to replace metallic parts with other materials to improve this ratio. Composites are thus considered to be a practical choice. For instance, modern planes such as the Boeing 787 Dreamliner and Airbus A350 rely on CFRP parts [2].

As with other materials, composite structures need to be inspected. Due to the non-homogenous properties of CFRP, evaluating their integrity is challenging [3]. Failure in CFRPs involves a sequential accumulation of different types of damages, which gradually leads to the loss of the design load capacity [4]. Examples of flaws in CFRP are disbonds, porosity, inclusion, environmental ingress, matrix cracks, fibre breakage and delamination. In some cases, the imperfection or damage constitutes a combination of the mention flaws. For instance, an impact damages can be a combination of matrix cracks, fibre breakage and multiple delaminations [5].

0.4 Impact damage

Impact damage is categorized into low-velocity impact damage (LVID) and high-velocity impact damage (HVID). The low-velocity impact is caused by quasi-static force, the higher limit of impactor velocity ranging from one to a few tens of ms^{-1} depending on the material's and impactor's properties. In HVID, boundary condition effects are negligible because the impact event is over before the stress waves have reached the edge of the structure. HVID is characterized by impactor penetration and induced fibre breakage, while LVID results in delamination and matrix cracking. Matrix cracks typically occur near the impact location. The cracks do not affect the laminate strength significantly, although they are usually the first failure mode to occur in delamination, Fig. 1-1 [6], [7].

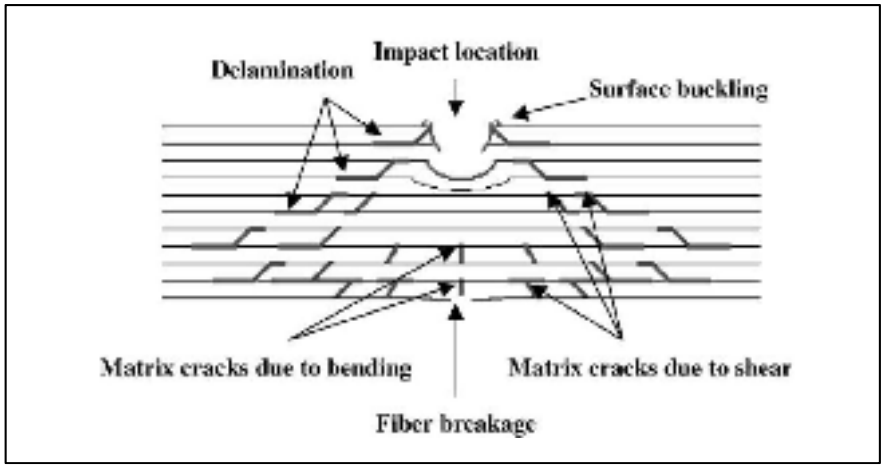

Figure 0-1 Typical impact damage mode for CFRP laminate [7]

The delamination pattern is dependent on the structure of the fabric. Typically, multiple butterfly-shaped delaminations are observed in the impacted area. They are extended through the axis parallel to the fibre direction. The delaminations are expanded in size, with an increase of the impact load. They rotate from the depressed surface to the bottom layer [7], [8]. LVID on aircraft is due to either operational or maintenance events. In service, hailstone strikes, birds and runway debris are the primary causes of LVID. In maintenance operation, LVID is due to accidental tool drops. Such blunt impactors could cause little permanent indentations and barely visible impact damage (BVID), which may end-up contributing to large delaminations [9]. Boeing damage definition classifies BVID as small damage, which may not be found during heavy maintenance general visual inspections, using typical lighting conditions, from a distance of five feet. Damage dent depth is typically 0.01 to 0.02 inches [10]. This type of damage can have a significant effect on the strength and durability of the structure. Therefore it is a primary concern for the design and the maintenance of composite structures. A wide range of characterization techniques, both destructive and non-destructive, can be employed to improve our understanding of the damage mechanisms occurring in CFRP panels. However, destructive tests have a significant limitation, which is the partial or total loss of the test part [11].

0.5 Non-destructive inspection

The terms of nondestructive evaluation (NDE) or nondestructive testing are defined for a vast range of analysis techniques performed on structures or materials to determine the existence or absence of discontinuities without damaging the object [5]. Although NDT is not able to guarantee that failures will not occur, it has a significant role in reducing the potential of failure in structures. Other factors, such as weakness in design and improper application of the object, may contribute to failure even if NDT is appropriately applied. In other words, NDT is an extension of the human senses with the use of electronic and mechanical instrumentation. According to historical evidence, the use of NDT dates back to Roman times. They detected cracks in marble slabs by using flour and oil. The other early recorded application of NDT was in 1868 when S.H. Saxby applied a compass to find cracks in gun barrels. Many kinds of primary NDT methods were developed during World War II (WWII). In that time, NDT began to be recognized as an independent technology, through the establishment in 1941 of The American Industrial Radium and X-Ray Society which is known today as ASNT. Before WWII, design engineers were relying on unusually high safety factors. As a result of the war, the relationship of discontinuities to the lifetime of structures became a concern. Besides, there were a significant number of catastrophic failures linked to product inadequacies [12]. The evolution of non-destructive testing can be directly connected to increased concern for safety, the reduction of safety factors, the development of new materials, and the overall quest for more product reliability [13]. Nowadays, nondestructive testing is used effectively for the analysis of raw materials before processing, to control a manufacturing process, to evaluate final products, and to monitor structures in service.

Aerospace industry and NDT

Inspection criteria for aerospace structure tend to be one of the most critical among industries. The restriction on the weight, to create effective and economic structures, limits the safety margin in the design parameters. High safety margin of about four or higher is considered for critical components in other industries while, for aerospace applications, this factor typically

ranges from 1.15 to 1.5. Therefore, nondestructive testing in aerospace industries concerns even smaller discontinuities size that will not grow to critical size during the operational cycle [12]. As mentioned before, aerospace structures are a compromise between low weight and high safety. Therefore, the use of CFRP is appropriate in terms of weight reduction and fuel economy. On the other hand, the manufacturing process and the monitoring of these structures in service constitute a novel challenge for NDT. The selected inspection methods should, therefore, be very sensitive while being reliable.

0.6 NDT on CFRP structures

The six primary NDT techniques developed for the steel industry are visual testing (VT), ultrasonics (UT), X-ray radiography (RT), liquid penetrant testing (LPT), magnetic particle testing (MPT) and eddy-current testing (ECT). VT, UT and, to a lesser degree, RT and ECT could be applied to the inspection of CFRP structures. In addition, numerous alternative techniques such as mechanical impedance testing (MIA), strain monitoring testing (SMT), Acoustic emission testing (AET), infrared thermography (IRT) and shearography (ST) are used in the composite NDT field [14]-[16].

NDT methods are generally classified into two groups, point-by-point and full-field methods (Table 0-1). Both of them have their specific applications in testing and evaluating the CFRP laminates. In most of the case, point-by-point NDT techniques require a contact medium, between the sensor and the test part, to obtain a reliable analysis. In terms of full-field methods, due to the elimination of physical contact, between the sensor and tested structure, they tend to speed up the data collection process.

Table 0-1 Point-by-point and Full-field NDT approaches

Point-by-point methods	Full-filed methods
Ultrasonic testing	Radiography testing
Mechanical impedance analysis	Thermography
Electromagnetic testing	Laser interferometry
	Visual inspection

0.7 Point-by-point NDT methods

As a point-by-point NDT method, MIA measures the mechanical impedance of a point on the surface of a structure by applying a harmonic force to it at a single frequency (1 to 10 kHz). In fact, the stiffness of the part under test affects the mechanical loading of the probe that sits on it; going from good to flawed areas changes the phase and the amplitude of the mechanical vibration induced by the probe. Because they significantly reduce local stiffness of a part, debonds in adhesive joints as well as delamination and voids in laminated structures affect the dynamic properties of a part and are thus good candidates for MIA inspection. The sensitivity of the method changes with frequency, so selecting appropriate driving frequency is critical to obtain the greatest difference between good and bad parts [14].

In AET, sound wave pulses are triggered by an external loading which is often provided by regular operating conditions of the monitored structure. These acoustic pulses are caused by a sudden release of the energy stored in discontinuities that are growing under the applied stress [16]. In a typical test, a piezoelectric transducer is mounted on the surface of the test part. It converts the elastic wave into electrical signals that are amplified and digitized for further numerical processing. In most of the cases, data extracted from AET signals are more difficult to interpret than signals extracted from other NDT methods [12], [17].

ECT is based on electromagnetic induction. A coil is driven by an alternating current so as to produce magnetic flux. Eddy currents are induced in an electrically conductive part exposed to this flux. Variation of eddy current intensity results in changes in the electrical impedance of the test probe. This method is broadly used for detecting cracks and corrosion in metals. Although electrical conductivity is lower in CFRP as compared to metallic parts, ECT has the potential to inspect them. However, it is challenging to apply conventional ECT methods to CFRP because of low conductivity and the anisotropic properties of the CFRPs [18].

UT is the most frequently used NDT method to detect internal flaws in CFRP laminates. An ultrasonic system consists of a transmitter and a receiver circuit, a transducer tool, and a display device. Based on the information carried by the signal, location, size and orientation of the flaws are characterized [19]. Pulse-echo is a conventional ultrasonic testing mode also named

as a reflection method. It is based on an ultrasonic energy beam reflected from the medium interfaces. When ultrasonic waves encounter a defect, the reflected energy can be distinguished from a back wall echo of the sound area. For damage detection on a CFRP laminate, the pulse-echo technique has limitations on distinguishing the layer-by-layer information signals. As a result, Time-of-Flight (TOF) scan has been developed to allow delamination or cracking to be identified and localized with better accuracy. UT has an excellent ability in sizing and revealing the location of flaws such as matrix crack and delamination in CFRP, although UT is time-consuming and requires a contact medium [20]-[21].

0.8 Full-field NDT methods

In today's competitive aerospace industries, high-speed inspection technology is needed. Full-field NDT methods are providing a faster inspecting speed for new aircraft both during the manufacturing process and in the field. For instance, a point-by-point inspection method, such as UT C-scan, have a slow-pace inspection of about 10 sq. ft ./hour. On the other hand, for a full-field method such as shearography and thermography, an inspection rate of 25 to 1200 sq. ft per hour is achievable. Therefore, a fast, full-field and real-time technique is essential to ensure quality and reliability at the lowest possible cost and time [22].

Among available full-field NDE methods, VT is, at the same time, the simplest and the fastest one. However, VT has an inherent disadvantage in the characterization of interior damages. In some cases, the internal failure mechanism absorbs impact energy without showing any external sign of the flaw. Although the visual inspection is a routinely performed task as part of an aerospace maintenance schedule, its definition varies notably from one source to another. In general, we can say that it is an evaluation method based on human sensory systems aided only by mechanical tools such as magnifiers and borescopes [6], [23].

RT is a widely-used NDT damage analysis method. An X-ray source transmits a beam of photons through the specimen and a sensitive film or sensor is used to image the intensity of the transmitted X-rays. The darker regions on the film received more X-ray photons than the brighter areas. The absorption of X-rays varies with the thickness and the density of the test material. Any defect that changes at least one of these two parameters will thus create a contrast

in the radiographic image. Radiography shows excellent performance in detecting voids and inclusions. However, this technique is susceptible to the angle of the incident beam with respect to the defect orientation. Therefore, delamination is not detectable as the incident X-ray beam is perpendicular to the plane defect [24].

Thermography and shearography are both full-field and real-time methods to evaluate the nature and the severity of defects such as delamination in laminar composites [15], [25]–[29]. Since delamination is the primary feature of impact damages, high performance and reliability are expected from these methods to assess this type of damage.

0.8 Infrared thermography

IRT (infrared thermography) is reported as an applicable method to evaluate the nature and the extent of defect in CFRPs [30]–[32]. It is conducted in aerospace industries mostly to detect delamination and moisture ingress in composites wherein the variation in thermal diffusivity between CFRP and the flaws produces excellent NDT indications. IRT techniques are based on thermal contrast, which is recorded from the surface of the test material. On top of a defect, parts' surface temperature will be different in comparison to the sound area. In this method, a thermal excitation source heats the specimen while the surface temperature of the test part is monitored by an infrared camera. The heating process can vary in terms of application area (surface, line or point) or the type of modulation (step, pulse or periodic forms). The thermal response is captured for a determined period, deeper defects requiring a longer observation period. In fact, temperature variation is a function of the discontinuity depth and the thermal proprieties of the defect and the test part [33].

IRT techniques can be classified by the arrangement of the specimen, infrared camera, and thermal stimulation source. Practically, in most of the cases, the advantages of thermographic non-destructive testing are demonstrated in a one-side procedure, which is called the reflection mode. In this case, both camera and heating sources are located on the same side of the specimen. On the other hand, a two-sided, or transmission test, requires that the heat flow crosses the thickness of the part and, therefore, can not be applied to thick or thermally-insulating materials [34].

IRT indications can be degraded by many factors such as noise, external heating, and cooling sources and uneven characteristics of the object's surface. Therefore, raw infrared images are many times not appropriate. In these situations, the solution is to apply post-processing methods such as normalized temperature contrast [35], Fourier transforms [36], cold image subtraction (CIS) and median filtering [37].

0.9 Shearography

Optical interferometric non-destructive testing methods such as holography, electronic speckle pattern interferometry (ESPI) and shearography are based on laser speckle images. They are used to indicate, size, and evaluate surface and internal anomalies in a structure when appropriate stress is applied. Even though the laser beam does not penetrate the test material, these methods can evaluate interior defects. They are applied to aerospace structures to detect discontinuities such as delaminations, inclusions, porosities and cracks. Among the different interferometric methods mentioned above, shearography is the one that best suits industrial requirements because of its immunity to vibrations and its less stringent requirement on laser performance.

Shearography is a full field and real-time method to evaluate the nature and the severity of a defect in laminar composites. Shearography makes it possible to visualize the spatial derivative of surface displacement i.e. its local strain. The basic principle of speckle interferometry involves the comparison of speckle patterns before and after the loading of the test part. In this work, thermal stress is used to load the test part and to produce shearograms [38]. Processing of these speckle patterns leads to a fringe pattern which could be converted to a phase map using a phase unwrapping algorithm. Based on the laser wavelength, this phase map could be further converted to the spatial derivative of surface displacements [39]. Discontinuities in laminated composites are depicted as anomalies of the strain on the surface of the inspected part. As a matter of fact, under loading conditions, structural defects in CFRP cause strain concentration.

0.10 NDT simulation

With the help of computer-aided engineering, a test procedure can be simulated with mathematical algorithms. Simulation in the NDT field has become increasingly diverse over the years. NDT simulation is used in a wide range of different applications such as performance demonstration of existing methods, Probability of Detection (POD) studies, the study of the inspectability of components and design, and optimization of methods [40]. Virtual testings lead to a better understanding of the test's physics. Also, predicting and explanation of test results for different situations by validation data are the key points when using NDT simulation [41]. Many NDT commercial simulation softwares are available for different NDT techniques but not for all of them, such as thermography and shearography. Physical complexity and novelty of the tests and their techniques could be the reasons for this. However, several works have been done to develop test models in these areas [39]–[45]. Among the various numerical methods used to solve mathematical models, finite elements are often preferred to analytical solutions for complex models. Following the validation of such a finite element model (FEM) through proper experiments, engineers use this virtual approach to increase the understanding of the test phenomena and to optimize the testing parameters for a specific part.

0.11 Objective

In this study, a combination of NDT methods is performed experimentally to evaluate the low-velocity impact damage in CFRP coupons. Infrared thermography and shearography testing are conducted to evaluate the detectability and the sizing capability of the methods for different levels of impact damage in the CFRP panels. The indications are discussed, and sizing capabilities are compared with ultrasonic testing results.

Moreover, the detection principles of these methods are investigated through FEM whose solutions replicate experimental tests.

0.12 Thesis plan

Using a drop-weight impact system according to ASTM D7136/D7136M-15 standard, impacted CFRP panels at energy levels of 10J, 15J and 25J, are used as the test parts for the current work. Firstly, the ultrasonic time of flight C-scan is conducted to quantify the configuration of the impact damage on the CFRP components. This inspection is performed in immersion using a Zetec Topaz device, a 64-element 5 MHz probe, and two encoders. This technique reveals the size and the depth of the delamination in the impacted area and is considered as the reference data to compare the other inspection technics with. Infrared thermography techniques, including pulse and step heating, are applied to study the thermal signals of the defective and the sound areas. In this study, the 640 × 512 detectors of a cooled Telops infrared camera is used to record thermograms, while two 3 and 6.4 kJ flash lamp are used to stimulate the coupons. IR-View and Matlab softwares are then employed to process experimental data. Heating stimulation is also applied to the component so as to be able to get a thermo-mechanical response that could be analyzed by shearography. To do so, a DANTEC Q-800 portable system with eight 120mW lasers at a wavelength of 660 nm is used. The signals are analyzed by the ISTRA 4D X86 software. Afterward, the NDE results are compared to each other to investigate their capabilities and limitations. Finite element models are finally designed to simulate infrared thermography and shearography inspection process. The anisotropic thermal and mechanical properties of CFRP components are modelled in ANSYS Workbench. ANSYS ACP module is used to simulate the configuration of the CFRP layup and the component's geometry. Defects are considered as delamination in different layers. Finally, It leads to a study of the inspectability, different test parameters and data processing through the virtual testing.

0.13 Sequence of thesis

- Section 1: Literature review on non-destructive testing, NDT on CFRP including contact and non-contact methods, developments in infrared thermography, shearography and FEM simulation of these NDT methods, thesis objectives and plan.

- Section 2: Discussion about impact damage, test coupon specifications, and a report on the inspection of the coupons by ultrasonic testing.
- Section 3: Thermography testing, the basic concept and theory, pulse thermography, experimental setup and data acquisition, infrared thermography post-processing methods and experimental results.
- Section 4: Shearography testing, principles and basic concept, experimental setup, data acquisition and experimental results.
- Section 5: Thermography and shearography simulation; boundary conditions, geometry, meshing and simulation results.
- Section 6: conclusion.

CHAPTER 1

TEST SPECIMEN

1.1 Overview

This chapter starts with an introduction that explains the application of CFRP components in new airliners. It is followed by elaborating on impact damage, specifically BVID. As mentioned before, the ultrasonic test is conducted to evaluate impact damage in the CFRP panels. Therefore, in this chapter, the specification of the inspected specimens is described. Then, the ultrasonic testing background and the implemented test procedure are presented. Finally, the test results are obtained which reveal the size and configuration of the damaged area.

1.2 Introduction

CFRP components are rapidly replacing aluminum parts in modern commercial aircraft (Fig. 1-1). These composite components are durable, stiff, and more corrosion resistant as compared to the metallic parts. By using these composite parts, aircraft and their engines can be designed lighter and, as a result, fuel consumption can be reduced.

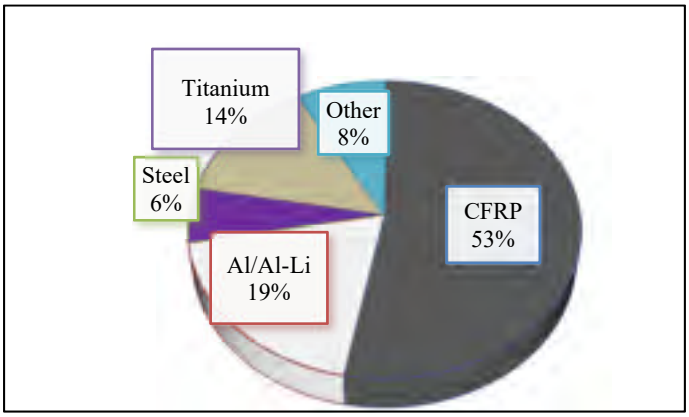

Figure 1-1 Material usage in Airbus A350 XWB
[87]

However, implementing these composite materials to the structural design of an aircraft is a complex problem. One of the complexities is that CFRP laminate failure modes are much harder to predict as compared to the metallic parts. Besides, anisotropic properties and complicated morphologies of the components is a challenge for NDT inspections [20].

1.3 Impact damage

In new aircrafts, as long as metallic parts of the fuselage, wings, and control surfaces are replaced with composite laminate [46], more CFRP components are exposed to in service and maintenance impact damages. Fig. 1-2 is demonstrating typical impact damage scenarios corresponding to different aircraft parts such as hail strick, bird strick, tool drop, ground equipment impact and foreign object damages (FOD).

Figure 1-2 Impact damage scenario

This type of impact creates an indentation on metallic parts. However, in impacted CFRP laminates, although impact can create severe interlaminar damage, surface layers tend to revert to their original shape without any visible indication of damages. This behaviour makes the visual inspection of laminates harder. Table 1-1 is showing typical impact damage scenarios and their severity in an aircraft's wing [6].

Table 1-1 Typical impact threats for aircraft wing structures

Area of Aircraft		Impact Risk	Energy J
Upper wing skin	Near fuselage (inboard)	Falling Tools	4
		Aircraft lifting equipment	20
		Refuelling by gravity	20
Lower wing skin	Outboard	Falling Tools	4
	Outboard & inboard	Hail Impacts	30-35
	Outboard	Loading of pylons	16
	Inboard	Runway debris	12-22

1.4 Barely visible impact damage (BVID)

Damage detectability can be categorized into four groups: Undetectable, Detectable, Readily detectable and Immediately obvious. Figure 1-3 depicts a typical relationship between damage size and the residual strength of the component. It also shows the damage detectability categories together with the design load.

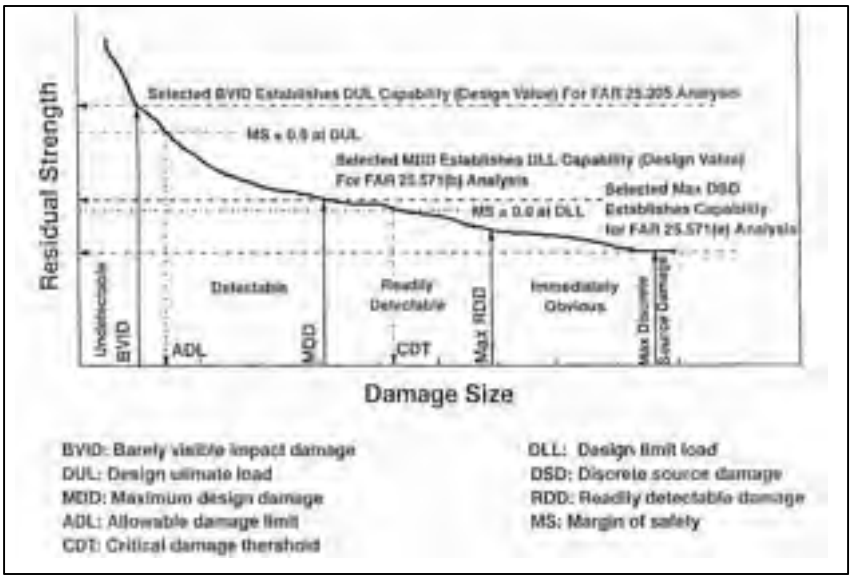

Figure 1-3 Damage category [23]

BVID falls in between undetectable and detectable regions. BVID is a crucial concept in the design of composite aircraft structures. The BVID size as an acceptable flaw in the inspection

procedures is determined using the design ultimate load (DUL) or the maximum expected in-service load. The design criteria are that BVID should demonstrate no-growth up to DUL. Fundamentally, impact damage reduces the compressive load performance of a laminate, although, for damages below the undetectable threshold, the structures are designed to be able to sustain the ultimate design load. Based on a safe life design, the damaged structure can be in-service until the part is replaced due to defined usage or time limits [47].

1.5 Test specimen

DPHM 501 [48] is a university-industry collaborative research project under the CRIAQ consortium. In this project, an extensive list of aerospace structures was identified by industrial partners, including military and civil aircraft manufacturers. Besides, based on maintenance, in-service manuals, and damage tolerance analysis reports, a list of in-service damages was provided. According to collected data, academic partners proposed relevant structures with artificial defects for experimental and numerical parametric studies. In this thesis, the test components are selected from the DPHM 501 parts. The coupons include three 30 cm × 30 cm CFRP panels which are composed of 16 plies, unidirectional prepreg tapes (Cycom 5276) with a quasi-isotropic layup $[45/0/-45/90]_{2s}$, Fig. 1-4. The thickness of each lamina is 0.15 mm.

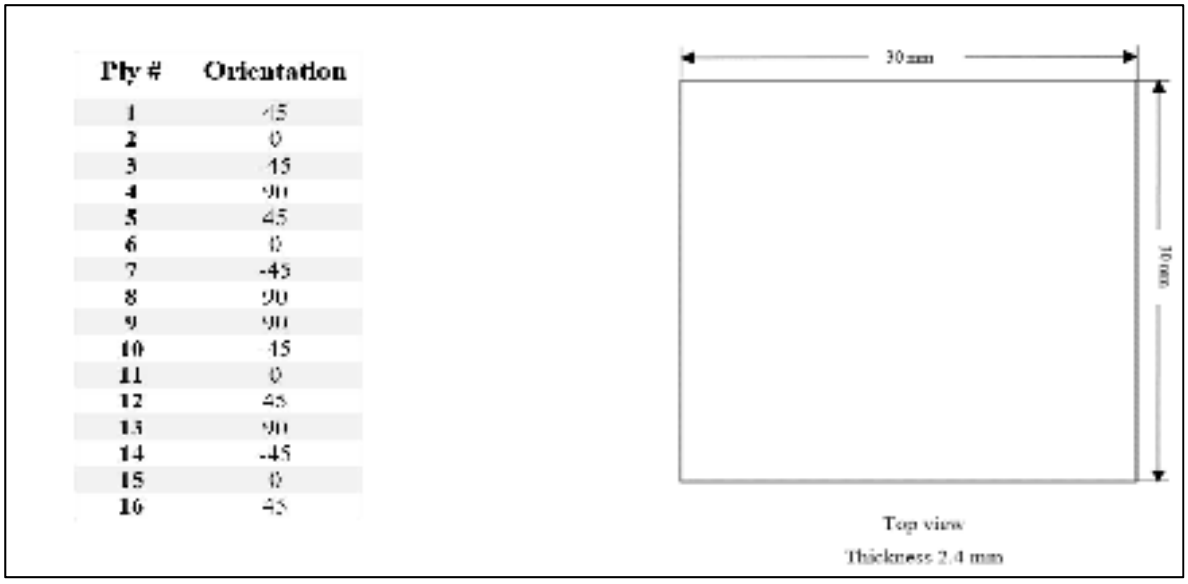

Figure 1-4 Layup configuration and dimension of the laminates

Therefore, the total thickness of the samples is 2.4 mm. All the coupons are laid up, vacuum bagged and cured in an autoclave.

The coupons are impacted at the center using a drop-weight impact system adhering to ASTM D7136/D7136M-15 standard [49] with energy levels of 10J, 20J and 25J. As mentioned in the standard, the weight of the impactor is 5.5 ± 0.25 kg and has a 16 mm diameter hemispherical striker tip. The hardness of the impactor ranges from 60 to 62 HRC. A summary of the four samples is given in Table 1-2.

Table 1-2 Coupons list

Coupons	Impact Energy
SC1.1-E2	--
SC1.1-E2	10J
SC1.1-E3	20J
SC1.1-E4	25J

1.6 Ultrasonic testing

In this work, ultrasonic testing is performed to locate and size impact damages on the laminates. C-scan and B-scan [20] reveal the size and depth of the defects. Before discussing the test procedure, a brief background of ultrasonic testing is presented in the subsequent section.

1.6.1 UT background

Ultrasonic testing is based on 0.1-15 MHz sound waves travelling in a test specimen. In most of the cases, very short ultrasonic pulses are transmitted into the test part, and the reflection of the sound beam from acoustic impedance discontinuities is analyzed to detect and map defects. In the following section, a few concepts of the test will be discussed.

1.6.2 Sound reflection

In ultrasonic testing, an interface is defined as a boundary between two different media. At the interface, part of a sound beam is transmitted to the second medium, while the remaining part is reflected back into the first one. The value of the reflected and the transmitted proportion depends upon the mismatch of the acoustic impedance at the interface (Eq. 1-1). In the case of a CFRP to water interface, 27.5% of the energy is reflected, and 72.5% is transmitted into the water. However, the situation changes for CFRP to air interface, where almost all the energy reflects, and none goes into the air.

Z_1 = CFRP acoustic impedance = 4.75 $kg/\mathrm{m}^2\mathrm{s}$

Z_2 = Water acoustic impedance= 1.48 $kg/\mathrm{m}^2\mathrm{s}$

$$\begin{aligned} Reflelected\ energy &= \left(\frac{Z_1 - Z_2}{Z_1 + Z_2}\right)^2 \times 100\% \\ &= \left(\frac{4.75 - 1.48}{4.75 + 1.48}\right)^2 \times 100\% = 27.5\% \end{aligned} \tag{1-1}$$

If the interface consists of CFRP to air, the reflected energy would be as follows:

Z_1 = CFRP acoustic impedance = 4.75 $kg/\mathrm{m}^2\mathrm{s}$

Z_2 = air acoustic impedance= 0.0004 $kg/\mathrm{m}^2\mathrm{s}$

$$Reflected\ energy = \left(\frac{4.75 - 0.0004}{4.75 + 0.0004}\right)^2 \times 100\% = 99.8\%$$

This property of sound waves allows the detection of discontinuities in ultrasonic testing. In a conventional UT, a couplant such as oil or gel is used between test items and transducer. Thereby making the transmission of the ultrasonic waves more efficient. By immersion technique, the tested part and transducer are submerged in a water tank. In this case, while a consistent distance between probe and component is maintained, more efficient sound-travel from the transducer to the specimen is realized [50].

1.6.3 Beam characteristics

In ultrasonic testing, a transducer converts a pulse of electrical energy into mechanical energy. The mechanical energy in the form of sound waves travels through the test part. The sound beam can be divided into two distinct zones called near-field and far-field. Near the ultrasonic transducer (near field) there are significant fluctuations in the sound intensity. The fluctuations are due to the constructive and destructive interference of the multiple wave patterns irradiated from the transducer surface, Fig 1-5. Because of the intensity variations, it is difficult to inspect materials in this area. The near field margin, NF, can be calculated from Eq. 1-2.

$$NF = \frac{D^2 \times f}{4 \times c} \tag{1-2}$$

D = Transducer diameter

f = Transducer frequency

c = Sound velocity

In the case of the immersion technique, it is suggested that the test specimen be placed at a distance beyond the transducer's nearfield so that, uniform wavefronts are transmitted into the specimen.

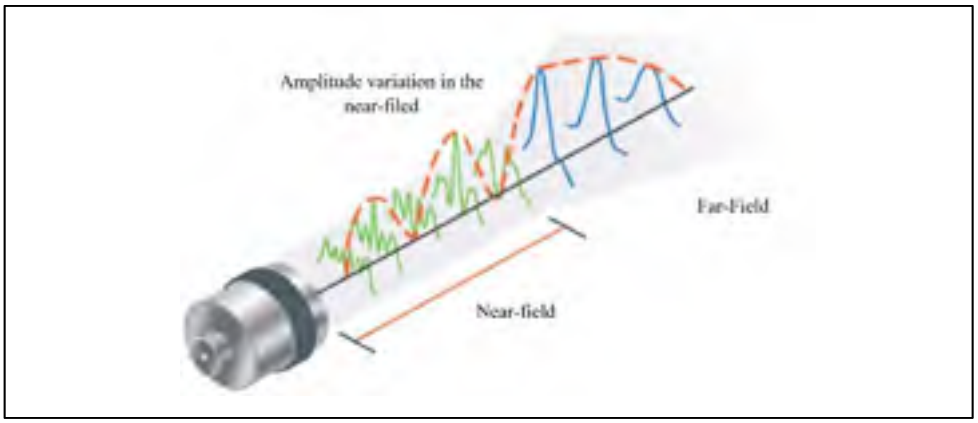

Figure 1-5 Visual depiction of near-field and far-field of a transducer [51]

In the near field, the beam is roughly cylindrical and is of the same diameter as the transducer crystal. Beyond the near field i.e. in the far-field, the beam spreads out like a cone (Fig 1-6) [49]. The angle of the cone (-6 dB half-beam spread angle) can be calculated from Eq. 1-2.

$$\sin\frac{\alpha}{2} = \frac{0.514 \times c}{D \times f} \tag{1-3}$$

Where;

$\alpha/2$ = Half angle of beam spread

f = Frequency

D = Transducer crystal diameter

c = Sound velocity in the medium

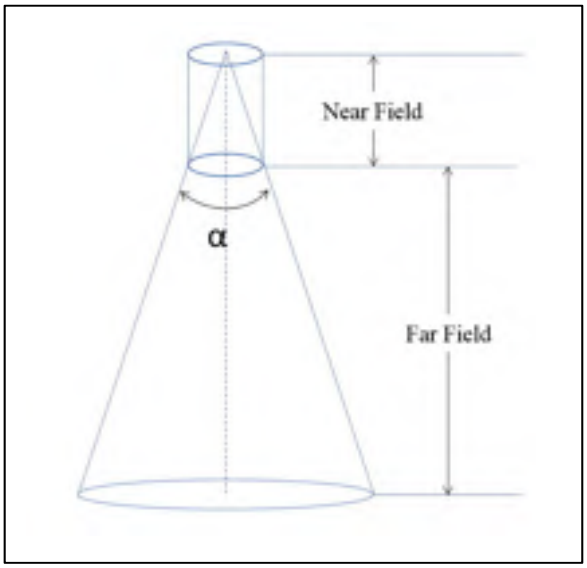

Figure 1-6 Ultrasonic beam spread

1.6.4 Phased-array probe

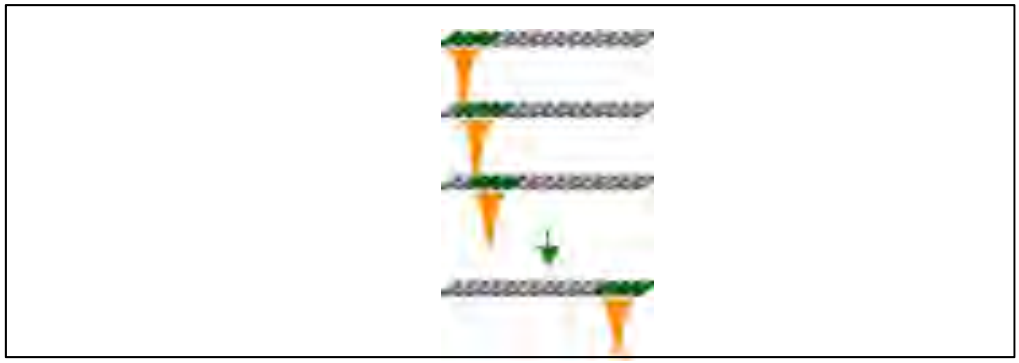

Figure 1-7 Schematic view of electronic scanning of a phased array probe [50]

A phased array probe is made up of multiple transducer elements. They work together as a large single element transducer. Each element has its own pulse and receiver circuit, and an ultrasonic system control all of them independently. The system activates each element by appropriate timing or phasing to achieve scanning function such as electronic scanning as shown in Fig. 1-7. The electronic scanning is performed by moving a beam in the inspecting area, which in turn activates different apertures. It also allows a mechanical scanning axis to be replaced electronically [51].

1.6.5 Gate

Gates are devices that are used at time base locations. They are applied to monitor the signal's horizontal position and amplitude percentage within a time window. Depending upon the signal's location, the electronic gates are moved. Modern UT flaw detectors utilize the gated signal to calculate and display flaw depth and also produce C-scan images [51].

1.6.6 Displays

There are different ways that ultrasonic testing data can be displayed.

- A-scan: It is the most basic presentation of ultrasonic data. In this display, echo's amplitude and transit time are plotted by a vertical and horizontal axis, respectively.

- B-scan: This type of scan presents a cross-sectional view of the inspected part. In the B-scan, the vertical axis displays time-of-flight, the travel time of the sound beam, and the horizontal axis presents the probe's position. Therefore, a B-scan is capable of determining the depth and the extent of the reflectors.
- C-scan: It is a plan view of the test piece parallel to the scanning surface. By using conventional probes, a C-scan is obtained, while a probe is moved back and forth and indexed to scan the entire test piece. In a phased array system, the probe is moved physically along the scan-axis while the beam electronically scans along the index axis. The data is displayed as a top view of the test piece, similar to an x-ray image. The colours represent the gated signal amplitude or the time of flight at each point in the test piece mapped to its x-y position [52].

1.6.7 Ultrasonic test procedure

In this section, the ultrasonic test procedure is presented. The tests are done, keeping in mind the tool and bag side of the CFRP coupons.

1.6.8 Ultrasonic setup

The Ultrasonic setup used in the current work is defined by the specifications which are provided in Tables 1-3 to 1-6. The ultrasonic phased-array testing is conducted by immersion technique. Fig. 1-8 demonstrates the flaw detector setup and its components.

Table 1-3 Equipment specification

UT System	Topaz 32/128 PR (ZETEC)
Software version	Ultra Vision 3.6R7T3

Table 1-4 Phased array probe parameters

Frequency	5 MHz
Number of elements	64
Pitch (primary axis)	0.6 mm
Element width (secondary axis)	10 mm
Total active aperture length	38.3 mm
Water column	110 mm

Table 1-5 General parameters

Voltage	75 V
Pulse duration	50 ns
Rectification	bipolar (Full Wave Rectification)
Filter	None
General gain	0 dB

Table 1-6 Phased array parameters

Electronic scanning	Linear 0°
Aperture	16 elements
Focalization	none

(a)

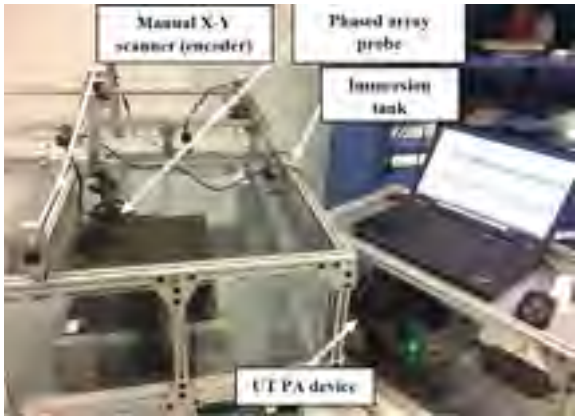

(b)

Figure 1-8 Ultrasonic immersion tank setup

In the test method, the coupon and the transducer are submerged in a water tank. The water acts as the coupling medium. An encoder is used for locating the probe position in the scan and index axes, as shown in Fig. 1-8. A normal scan is performed on both sides of the samples. Fig. 1-9 shows a typical A-scan acquired on a test coupon. The gate is set from immediately after the front surface echo until past the back wall echo so that TOF or thickness C-scan view is produced.

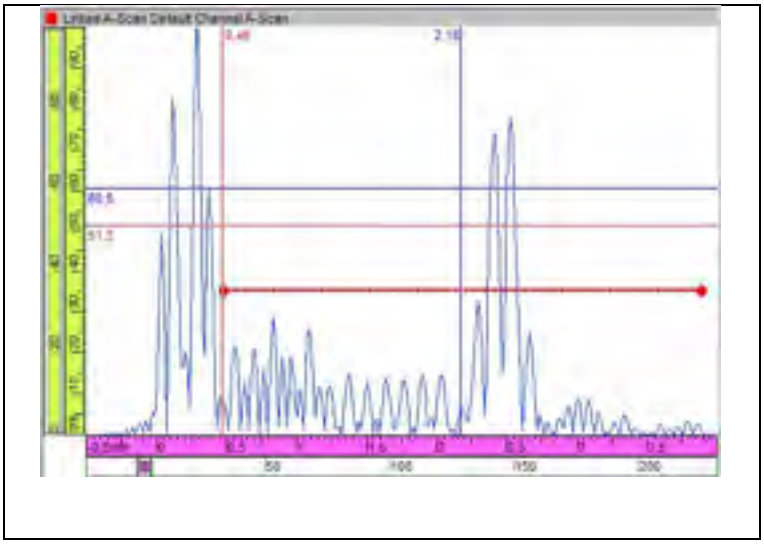

Figure 1-9 TOF technique's gate setup

1.6.9 Ultrasonic testing results

The ultrasonic testing is performed from the tool and bag (impact) sides. The C-scan time-of-flight results show how the delamination is extended in different layers, Fig. 1-10, Fig 1-12 and Fig. 1-14 (a and b). The damage sizes for the three coupons are mentioned in Table 1-7. The B-scan views through Y axis (Scan axis) are shown in Fig. 1-11, Fig. 1-13 and Fig. 15 (a and b). They demonstrate the damages are local, such that no fibres are broken around the impacted zone. A double-helix pattern is also observed in which conical delamination is formed through the thickness [21], [53].

Table 1-7 Flaw sizing by time-of-flight ultrasonic testing

Coupon	Impact (J)	Indication area (mm^2) Tool side	Indication area (mm^2) Bag side
SC 1.1-E2	10	479.3	455.6
SC 1.1-E3	20	594.9	539.8
SC 1.1-E4	25	554.4	550.8

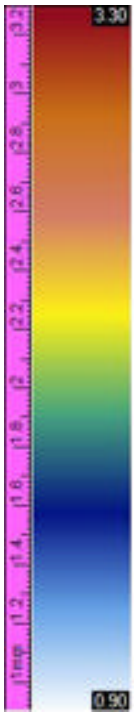

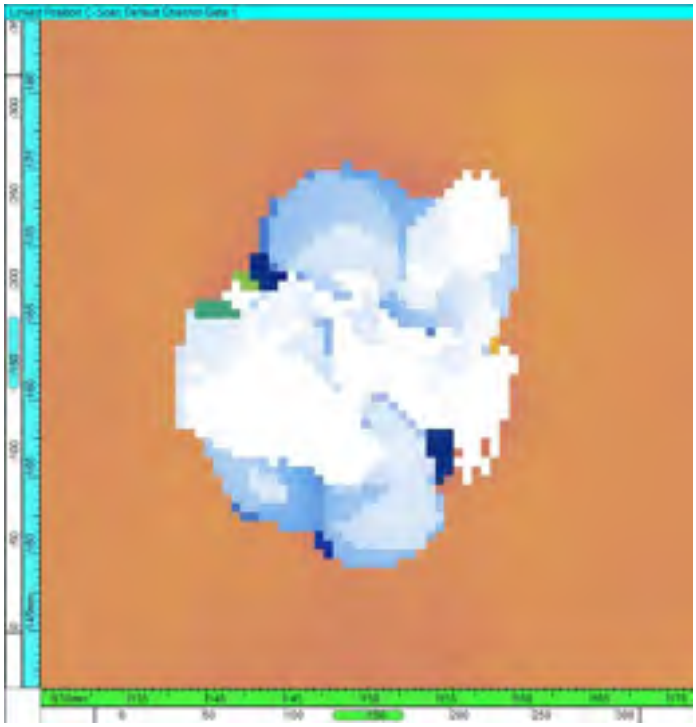

(a)

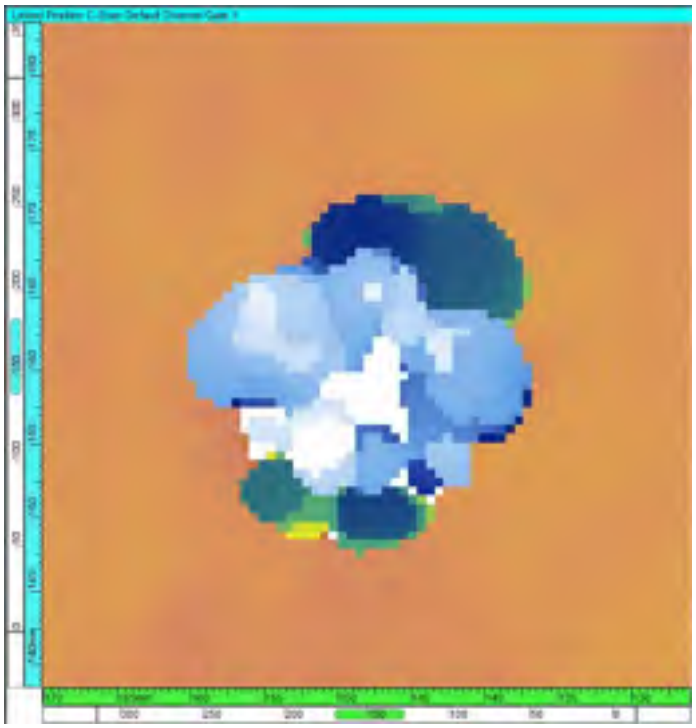

(b)

Figure 1-10 E2, C-scan of the defect from the (a) tool and (b) bag side

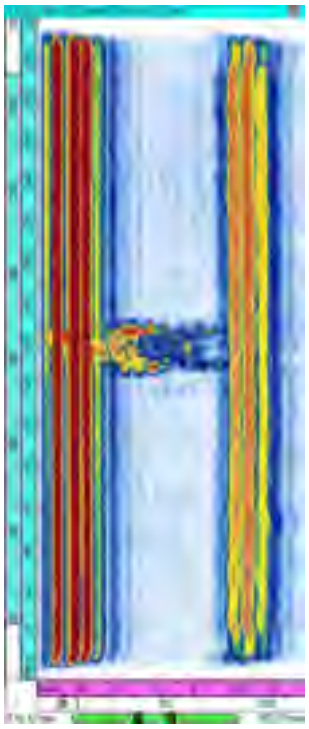

(a)

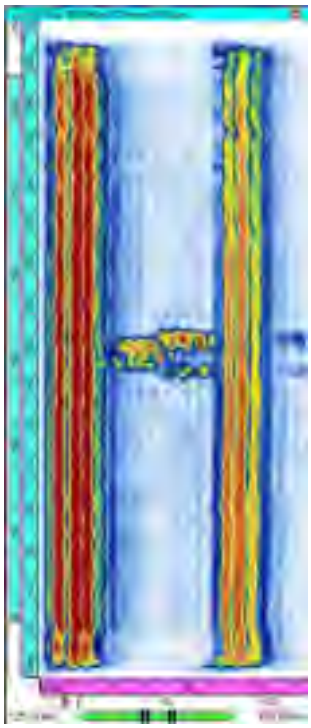

(b)

Figure 1-11 E2, B scan of the defect from
(a) the tool and (b) bag side

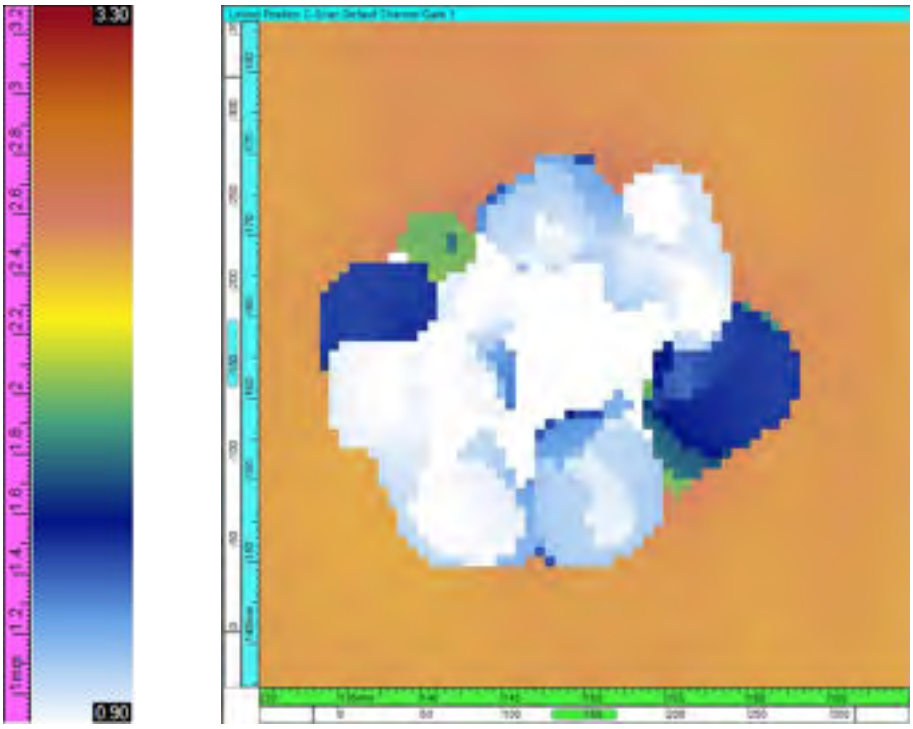

(a)

(b)

Figure 1-12 E3, C-scan of the defect from the (a) tool and (b) bag side

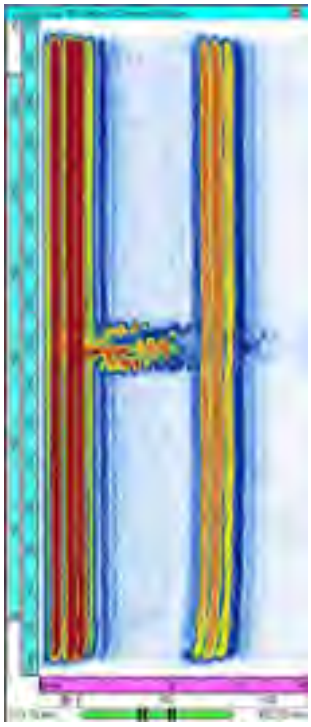

(a)

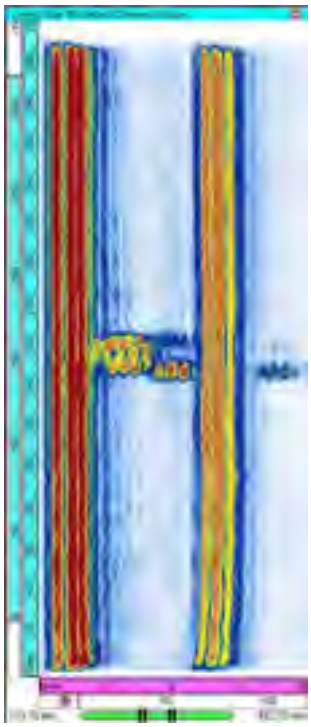

(b)

Figure 1-13 E3, B scan of the defect from (a) the tool and (b) bag side

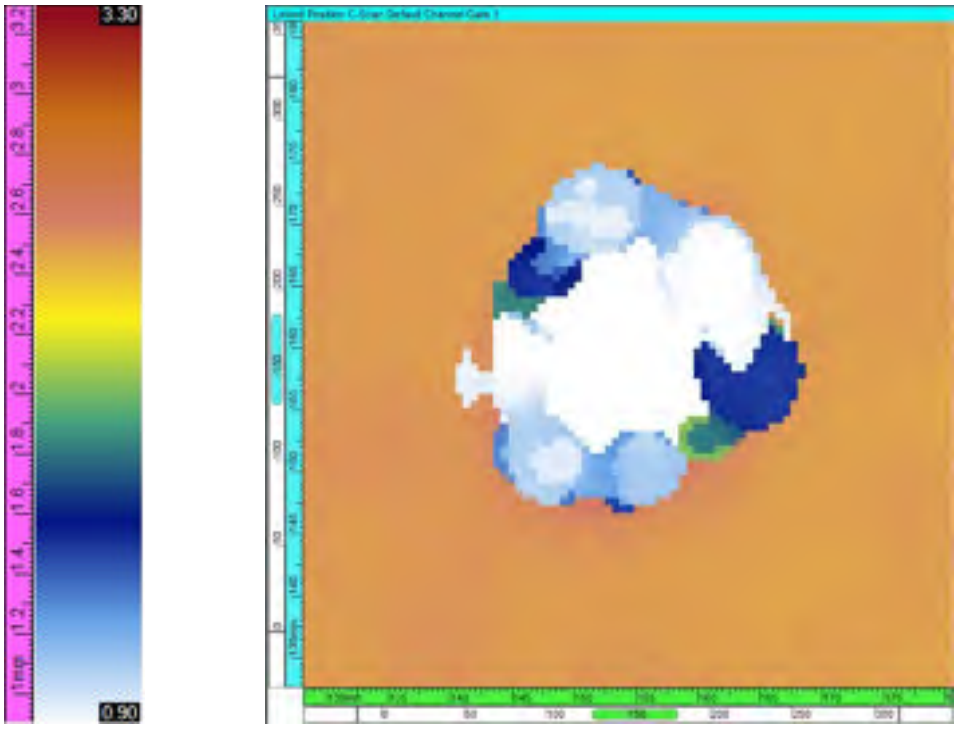

(a)

(b)

Figure 1-14 E4, C-scan of the defect from the (a) tool and (b) bag side

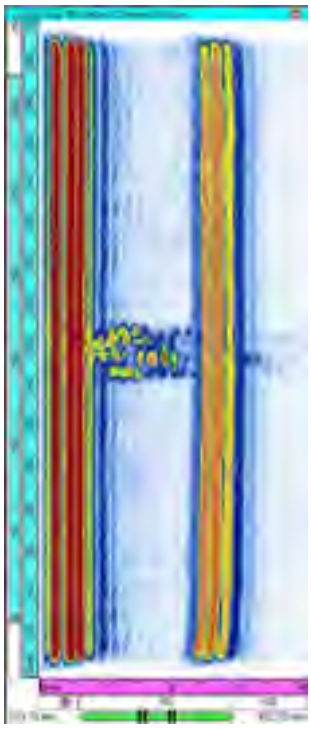

(a)

(b)

Figure 1-15 E4, B scan of the defect from (a) the tool and (b) bag side

CHAPTER 2

INFRARED THERMOGRAPHY TESTING

2.1 Overview

In this chapter, active infrared thermography techniques, are examined in reflection and transmission modes to evaluate low-velocity impact damage in CFRP. In a reflection mode, thermograms are recorded after stimulating the sample's surface with a heat pulse. In the thermograms, the contrast of defect/no-defect could be increased by Fast Fourier Transform (FFT) processing. Finally, transmission pulse thermography is performed to measure the variation of diffusivity due to the levels of impact damage.

2.2 Introduction

Active Infrared thermography (IRT), as an NDT method, is based on thermal contrast which is recorded from the surface of the test specimen after thermal stimulating. The contrast appears due to the thermal properties differences between the subsurface defect and the sound material. This field of NDT is expanding from civil or electronic components to an inspection of artworks or composite materials [54]. IRT of aerospace components has been used for several years. The main advantages of thermography over conventional NDT techniques are its full-field results, fast inspection rate, and the absence of safety concerns.

Most of the common damage scenarios occurring in aerospace components, including delamination, debond, water ingress, core crushing, and impact damage, can be detected and quantified by using active thermographic techniques [55]. In this section, some fundamental aspects of active IRT are discussed.

2.2.1 Infrared Radiation (IR)

Electromagnetic spectrum can be classified according to the wavelength of the radiation in a vacuum. Frequency bands like gamma rays, x-rays, ultraviolet, visible light, infrared,

microwaves, radar rays, radio waves, and broadcast bands are parts of this spectrum, Fig. 2-1. The electromagnetic spectrum band in the range of 0.74 µm to 1000 µm corresponds to infrared radiation, which lies in between the visible and the microwave spectra. Infrared radiation wavelengths are longer than visible light and can be recognized as heat. Objects with a temperature above zero kelvin emit infrared radiation. IR radiation is a function of the object's temperature. Therefore, measuring emitted infrared radiation of an object can be used to quantify the body temperature.

Basically, the relation between temperature and emitted infrared radiation is defined by the concept of blackbody [56].

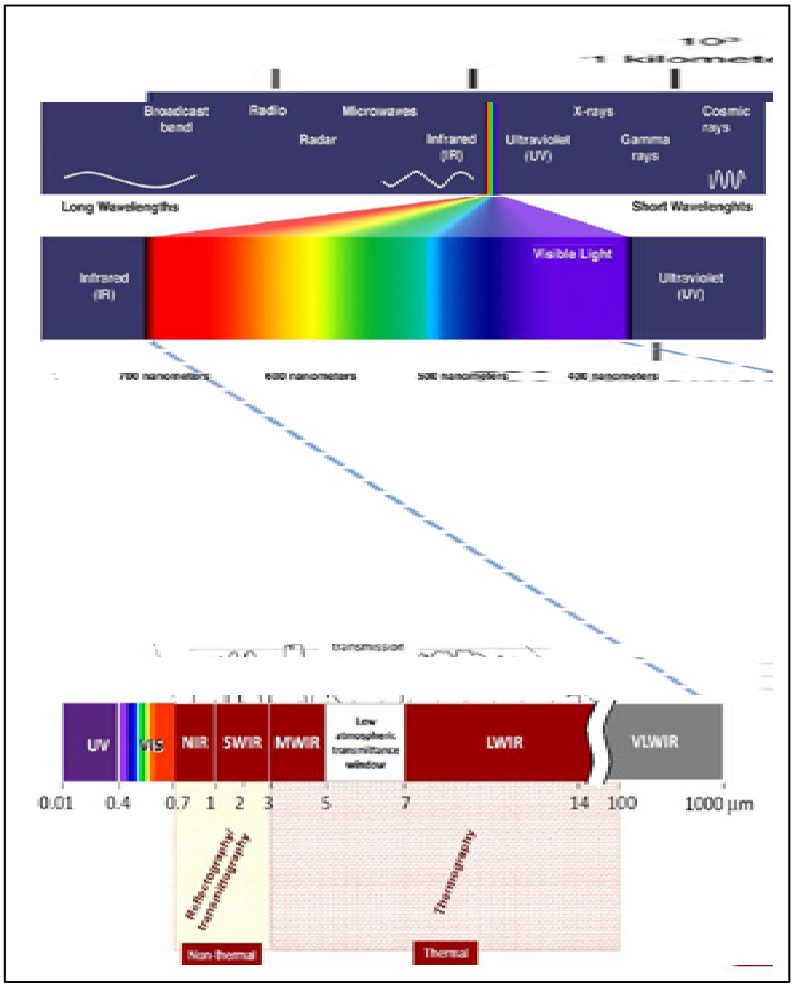

Figure 2-1 Electromagnetic bands [56]

2.2.2 Blackbody radiation

The radiometry in IR thermography is based on the blackbody concept and the Planck's law [34]. A blackbody is an ideal physical body that absorbs all incident radiation(s) regardless of direction and wavelength. Besides, it is a perfect radiator. As depicted in Fig. 2-2, the emitted radiation is a function of the wavelength and temperature but independent of the direction [56]. Planck's law describes the spectral radiance, $N_{\lambda,b}$, from a blackbody in thermal equilibrium as:

$$N_{\lambda,b}(\lambda,T)=\frac{2hc^2}{\lambda^5(\exp\frac{hc}{\lambda KT}-1)} \qquad (Wm^{-2}sr^{-1}\mu m^{-1}) \tag{2-1}$$

Where λ is the wavelength $[\mu m]$, T is the temperature $[K, Kelvin]$ of a blackbody, $h=6.63\times10^{-34}$ $[Js]$ is the Planck's constant and Boltzman's constant is $K=1.381\times10^{-23}[J/K]$. However, real objects have limited absorbance, and only a part of the energy will be radiated from their surface. This portion of the blackbody spectral radiance is given by a surface property called emissivity ε. Eq. (2-2) estimates the spectral radiance for real object:

$$N_{\lambda}(\lambda,T)=\varepsilon N_{\lambda,b}(\lambda,T) \tag{2-2}$$

Emissivity, ε, depends on wavelength, temperature, viewing angle and surface condition [34]. Due to the link between wavelength and temperature, the most effective radiometry is carried out for the wavelength at which the emission is the most intense. The pick of a blackbody spectral radiance, in the moderate temperature, is in the range of infrared radiation, Fig. 2-2 [57]-[58].

In general, the IR spectral bands can be divided into four bands:

- Near-infrared radiation band (NIR, from 0.75 to 1 μm)
- Short-wave Infrared radiation band (SWIR, from 1 to 2.5 μm)
- Mid-wavelength infrared Radiation band (MWIR, from 3 to 5 μm)

- Long-wavelength infrared Radiation band (LWIR, from 7 to 14 μm)

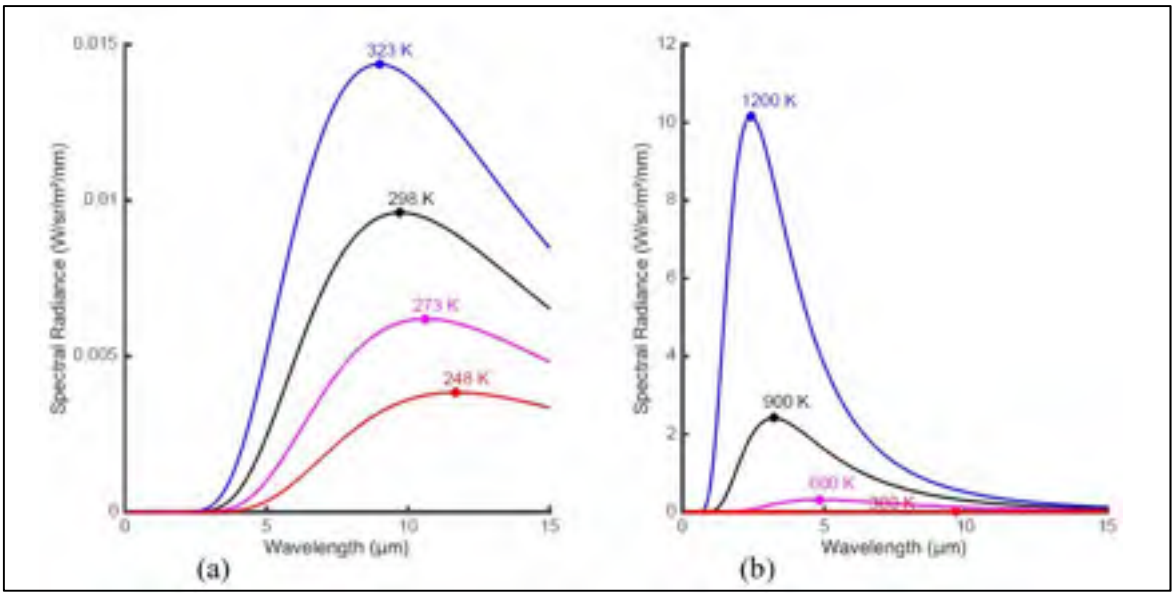

Figure 2-2 Planck's law curves for ideal blackbody radiation at moderate temperature (a), and higher temperature sources radiate much more intensely and peak spectral response is shifted toward smaller wavelenghts [57]

Two of these various bands, MWIR and LWIR, represent the practical bands in infrared thermography. Fig. 2-1 is showing, where IR is absorbed by different air particles, due to lower absorption in these two ranges, more radiation is allowed to reach the sensor of the camera. Therefore, it leads to a better assessment of the object's temperature by its IR radiation [56].

2.2.3 IR sensors

Infrared detectors are classified into thermal types and quantum types. Thermal detectors (uncooled sensors) use the infrared energy as heat, and their photosensitivity is less dependent on wavelength than quantum detectors. The thermal detectors do not require cooling, although they have a slow response time. In contrast, quantum detectors (cooled sensors) have higher detection performance and faster response speed, although their photosensitivity is dependent on wavelength. In general, quantum detectors must be cooled for accurate measurement [59].

The principle involves directly measuring the incident photon. The photonic excitation is measured by a change of electrical conductivity or a generated voltage in the sensors [34].

2.2.4 Infrared Thermography approaches

The term of IRT as an NDT method covers a wide range of applications and many inspection procedures, as explained in the following sections.

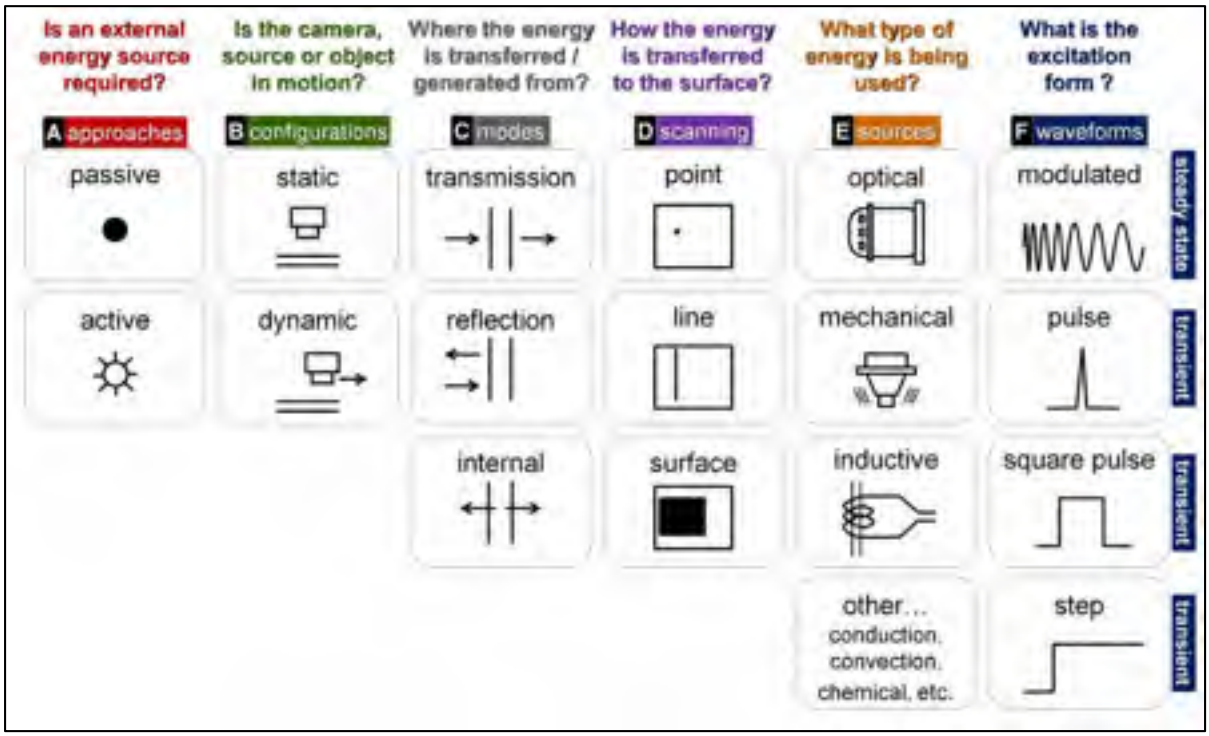

Figure 2-3 Variety of IRT scenario [60]

Fig. 2-3 presents a diagram showing the different parameters that need to be selected to design an NDT inspection scenario [60]:

1) Approaches:

- Passive: Test materials or parts are naturally at different (higher or lower) temperatures than their background. The inspection procedure does not intervene in the thermal equilibrium of the system.

- Active: An external source is needed to stimulate a thermal contrast on the object surface. The inspection procedure imposes a transient in the thermal equilibrium of the system, or it stimulates its harmonic response at a specific frequency.

2) Configurations:

- Static: The camera, the object and the source remain fixed during the inspection.
- Dynamic: At least one of these three elements is moving during the inspection.

3) Modes:

- Reflection: Energy is transmitted to the test specimen from the same side as the data are recorded.
- Transmission: Energy is delivered to one side of the specimen while data are captured from the opposite side.
- Internal: Heat is generated inside the test part, while data can be collected from either surface.

4) Scanning:

- Point scanning: A single point of the object's surface is heated at a time. To obtain a full 2D image, the system needs to perform a raster scan (step and index axes) over the object's surface.
- Line scanning: The heating source is focused on a line on the surface being inspected. To obtain a full 2D image, the system needs to move the line along a single scanning axis.
- Surface scanning: An entire area of the inspected object is heated at once. A full 2D image can be obtained without the need to move the source with respect to the object.

5) Sources:

- Optical: such as photographic flashes and halogen lamps
- Mechanical: such as sonic or ultrasonic excitation
- Inductive: such as eddy current induction

6) Waveform

- Modulated: thermal waves modulated at a given frequency
- Pulse: a short pulse of a few milliseconds
- Step: constant heat flux suddenly applied to the object surface
- Square pulse: a long pulse of several seconds

2.3 Pulse thermography

As mentioned before, infrared thermography can be divided into two primary approaches, passive and active. In the passive approach, test materials are at a different temperature than ambient. Whereas, in the case of the active approach, an external stimulation source is necessary to induce thermal contrasts. Active thermography as a non-destructive testing method (NDT) offers non-contact, full-field, and subsurface detection [28], [54], [55], [61]. Modes of active thermography can be classified by the arrangement of a sample, an infrared camera, and a thermal stimulation source. Practically, in most of the cases, the advantages of thermography non-destructive testing are demonstrated in a one-side procedure, which is called reflection mode.

Pulse thermography is a reflection method in which a thermal pulse stimulates the surface of the test part. While the thermal energy diffuses through the material in a three-dimensional manner, explained by the Fourier diffusion equation [62], the temperature of the cooling surface is recorded at regular time intervals by a thermal camera. The captured thermograms form a 3D matrix of pixels and whose intensity corresponds to the temperature evolution of the pixel during the post-flash time, Fig. 3-4 [63]. For a sound area, the temperature of the surface decays as the square root of time [34].

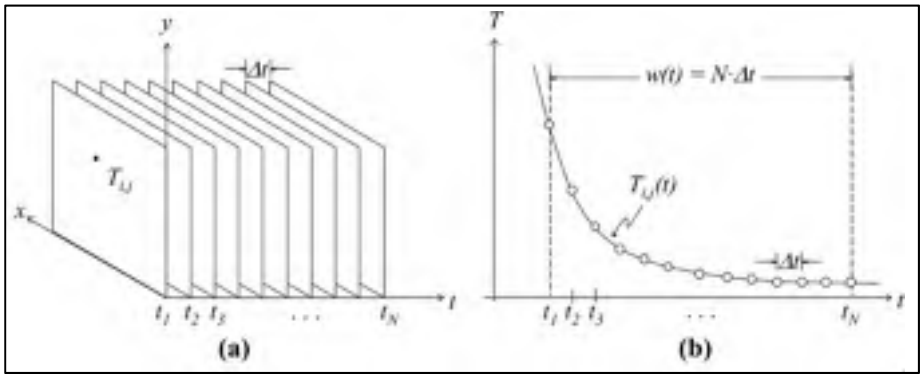

Figure 2-4 (a) Temperature 3D matrix on the time domain, and (b) temperature profile for a non-defective pixel on coordinates (i,j) [63]

2.3.1 Thermogram sequence

The complete thermogram sequence is composed of five distinctive elements depicted in Fig. 2-5 [63].

- Cold image: At the time t_0, before the heat reaches the specimen's surface, a cold image is captured. The cold image can be used to remove spurious reflections due to non-unitary emissivity and to reduce fixed pattern artifacts.
- Saturated thermogram: During the application of a heat pulse, the captured thermogram are saturated in temperature. The acquired data are out of the calibration scale, and no accurate measurement can be conducted from them.
- Early Recorded Thermogram (ERT): Although the usable thermogram sequence starts at the ERT, defects are usually not yet visible at that time. This is because the surface temperature evolution has not affected by the discontinuity yet.
- Thermogram sequence: All subsequent thermogram are of interest for defect inspection.
- Last Recorded Thermogram (LRT): As the last thermogram of the thermogram sequence, temperature variations are considered negligible from this point in time.

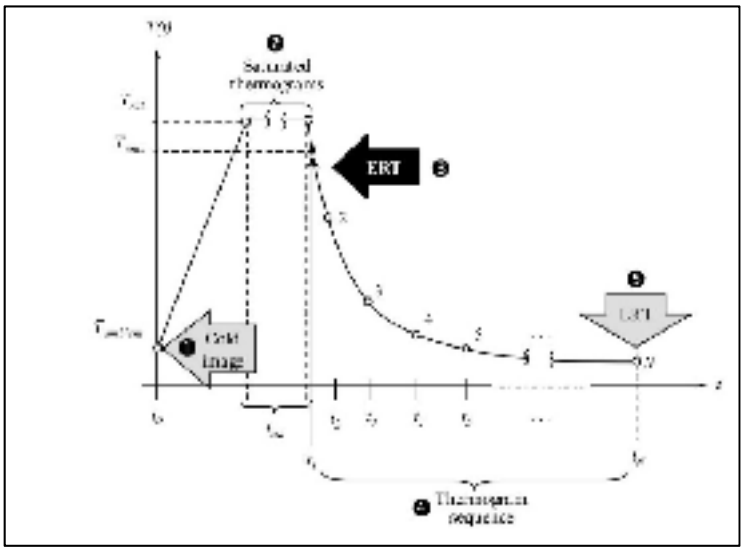

Figure 2-5 Complete thermogram sequence [62]

2.3.2 Flaw detection

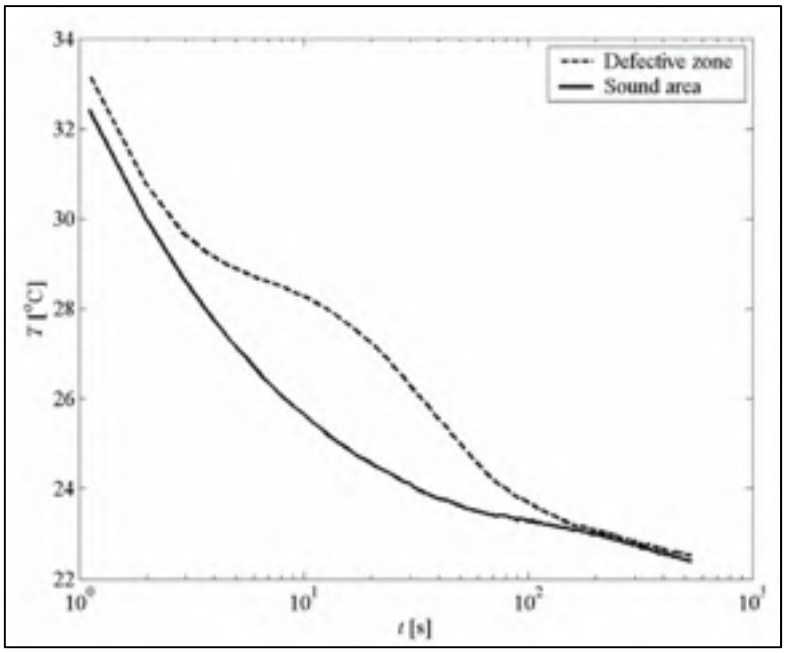

Figure 2-6 Defect detection from temperature profiles [62]

Fig. 2-6 presents a temperature profile, after applying a heat pulse, for a sound area and an artificial defect, a flat-bottom hole at a depth of 1 mm, in a plexiglass plate. In the first instance, the temperature decay curves for both the defective and the sound areas behave in a similar way. Although there is a difference in their temperature due to non-uniform heating at the surface. In this period, the heat energy does not reach the discontinuity yet. Since the material ability to exchange heat with its surroundings, thermal effusively, is much higher for plexiglass than the air, the sound area acts as a better thermal sink. Accordingly, once the thermal gradient has arrived at the bottom hole, the surface temperature will be higher over the defect compared to the sound area. It continues until the stabilization time.

Raw PT data, however, has some uncertainties to analyze. Therefore, a variety of post-processing techniques have been developed to enhance IR signatures [64].

2.4 Pulse Phased Thermography (PPT)

Indication signals can be degraded by many factors such as noise, external heating, cooling sources and uneven characteristics of the object's surface. Therefore, raw infrared images are not usually appropriate. A solution in these situations is applying a post-processing method such as pulsed phase thermography (PPT) [36].

PPT is based on the phase delay of thermal images. Non-uniform heating and surface emissivity variations have a negligible impact on the phase data. Moreover, phase data is more likely to respond to differences in material thermal properties rather than geometrical features [31]. The experimental procedure to perform a PPT is the same as PT. For the post-processing, once the temperature data has been captured, the entire sequence can be processed, at the pixel level, using the one-dimensional Discrete Fourier Transform (DFT), Eq. (2-2).

$$F_n = \sum_{k=0}^{N} T(k) e^{2\pi jkn/N} = \mathrm{Re}_n + \mathrm{Im}_n \, j \qquad (2\text{-}2)$$

Where j is an imaginary number, n designates the frequency increment and Re and Im are the real and the imaginary parts of the transform, respectively. For NDT applications, Eq. (2-2) is not practical due to massive computation time. The Fast Fourier Transform (FFT) algorithm is used instead because it reduces the complexity of computing and significantly speeds up the transformation process [63]. With the real and imaginary parts of the transform, phase delay ϕ, for a pixel becomes available as follows:

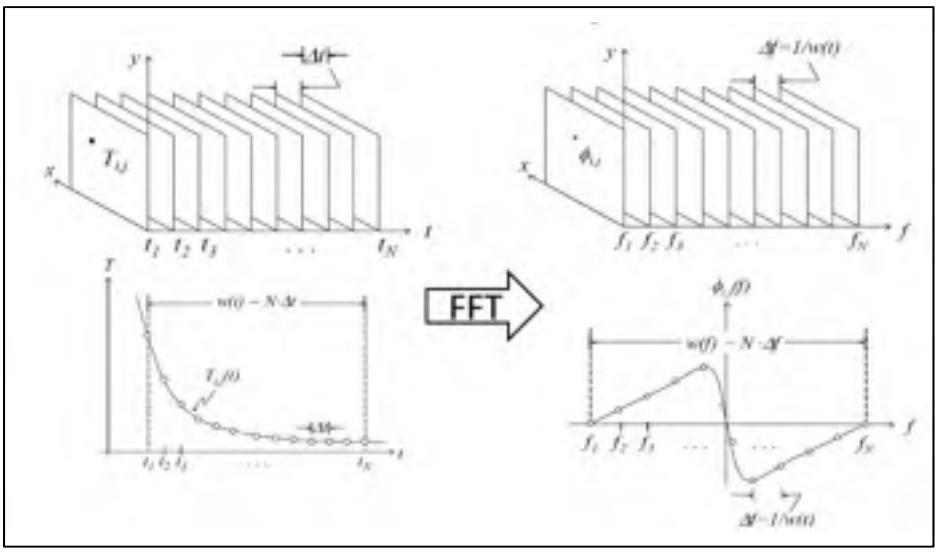

Figure 2-7 Transformations of thermogram to phasegram [31]

$$\phi = \tan^{-1}\left(\mathrm{Im}_n / \mathrm{Re}_n\right) \tag{2-3}$$

The procedure is applied for all the pixels on the sequence to form phase maps or phasegrams, as shown in Fig. 2-7 [31].

2.5 Transmission mode

To measure the thermal diffusivity of materials, Parker proposed a technique based on the analysis of recorded thermal image sequences caused by the transmission of heat pulses through the sample [30].

2.5.1 Methodology

In this method, a heat pulse is applied to the front surface of the test part, and the rising temperature is monitored from the test part's backside. If the heat losses are neglected, the normalized temperature of the back surface is given by

$$U(L,t) = 1 + 2\sum_{n=1}^{\infty}(-1)^n \exp(-n^2 \pi^2 \alpha t / L^2)$$
$$U(L,t) = \Delta T(L,t) / \Delta T_m \quad (2\text{-}4)$$

$U(L,t)$: dimensionless parameters
α : thermal diffusivity
L : specimen thickness
Where;
$\Delta T(L,t)$: temperature increase at time t
$\Delta T_m(L)$: maximum temperature rise

Parker suggested to use the time ($t_{1/2}$) at which the temperature rises at half of its maximum (ΔT_m) to estimate the material's diffusivity. Indeed, Eq. 2-5 gives a simple relation between the two.

$$\alpha = \frac{0.139 L^2}{t_{1/2}} \quad (2\text{-}5)$$

When thermal diffusivity is calculated with the pulse method, there are thermal losses that are inevitable. Therefore, the partial time method is proposed to measure thermal diffusivity without making restrictive assumptions about heat losses [65].

In this method, three intermediate thermal diffusivities are calculated per equations 2-8, 2-9 and 2-10. These equations use variables $t_{1/3}$, $t_{2/3}$, $t_{1/2}$ and $t_{5/6}$ that are the times of 1/3, 2/3, 1/2 and 5/6 of the maximum temperature at the rear surface after the stimulation. Eq. 2-6, 2-7 and 2-8 should result in almost the same value as α. Therefore, it is suggested that the average of the mentioned values are calculated in the thermal diffusivity map [65].

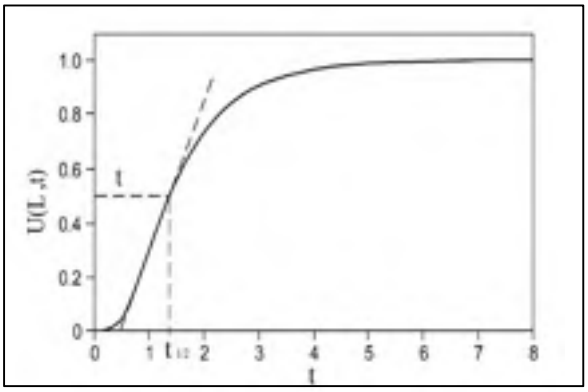

Figure 2-8 Dimensionless temperature history on the rear surface [32]

$$\alpha_{1/3} = \frac{L^2}{t_{5/6}}\left[0.818 - 1.708\left(\frac{t_{1/3}}{t_{5/6}}\right) + 0.885\left(\frac{t_{1/3}}{t_{5/6}}\right)^2\right] \tag{2-6}$$

$$\alpha_{1/2} = \frac{L^2}{t_{5/6}}\left[0.954 - 1.581\left(\frac{t_{1/2}}{t_{5/6}}\right) + 0.558\left(\frac{t_{1/3}}{t_{5/6}}\right)^2\right] \tag{2-7}$$

$$\alpha_{2/3} = \frac{L^2}{t_{5/6}}\left[1.131 - 1.222\left(\frac{t_{2/3}}{t_{5/6}}\right)\right] \tag{2-8}$$

2.6 Experimental procedure

As mention before, two modes of IRT are conducted in this study. The following parts present the applied test procedures and test setups.

2.6.1 Reflection mode procedure and test parameters

In this experiment, the acquisition is conducted using a cooled Telops camera, TEL-1000 MW MCT 640 × 512 pixel array, 3.6 μm to 4.95 μm spectral range and 16 μm pitch detector. Moreover, two Hensel photographic flash lamps, each generating a 3 kJ heat pulse in 4 ms are used. The lamps were placed at 0.8 m away from the sample, at 45° from a normal angle of the

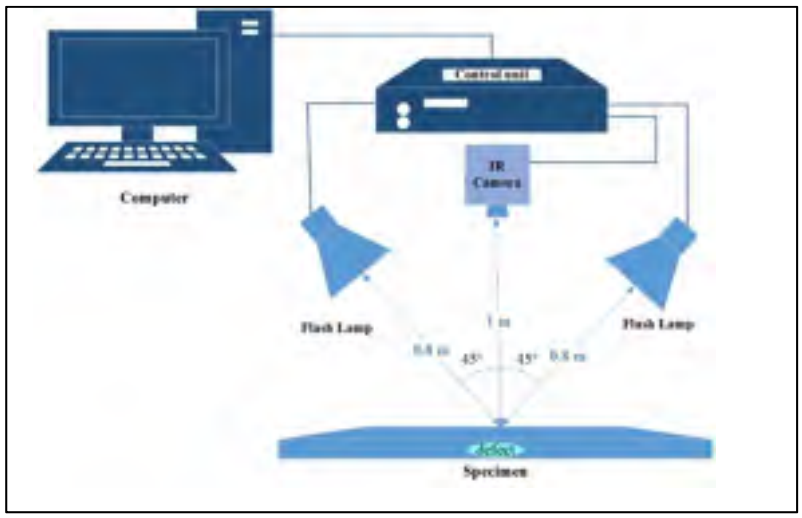

Figure 2-9 IRT reflection mode

specimen's surface and the distance between the camera and sample is 1m at the normal angle, Fig. 2- 9 and 2-10. The frames are recorded for 20 seconds in the cooling process at a frequency of 50 Hz. Matlab and IR-view [66] are used to process raw temperature data.

Figure 2-10 IRT reflection setup

2.6.2 Transmission mode procedure and test parameters

In this technique, a short pulse is applied to heat the rear surface (tool side), and the temperature rise on the front surface (impact side) is recorded, Fig. 2-11. For all inspections, an MWIR camera, Fig 2-12, (FLIR Phoenix, InSb, 3-5 μm, 640 × 512 pixels) was used to record the temperature profiles. In the pulsed thermography inspection, two photographic flashes (with a pulse duration of 2 ms and producing 6.4 kJ per flash) were used to heat the samples. Images were recorded in transmission mode. The distance from the samples to the lamps is 0.6 m, and 0.8 m to the camera. The acquisition rate was 50 Hz, and the sequence has 1000 images. Matlab and IR-view, as a Matlab graphic user interface, for the NDT are used.

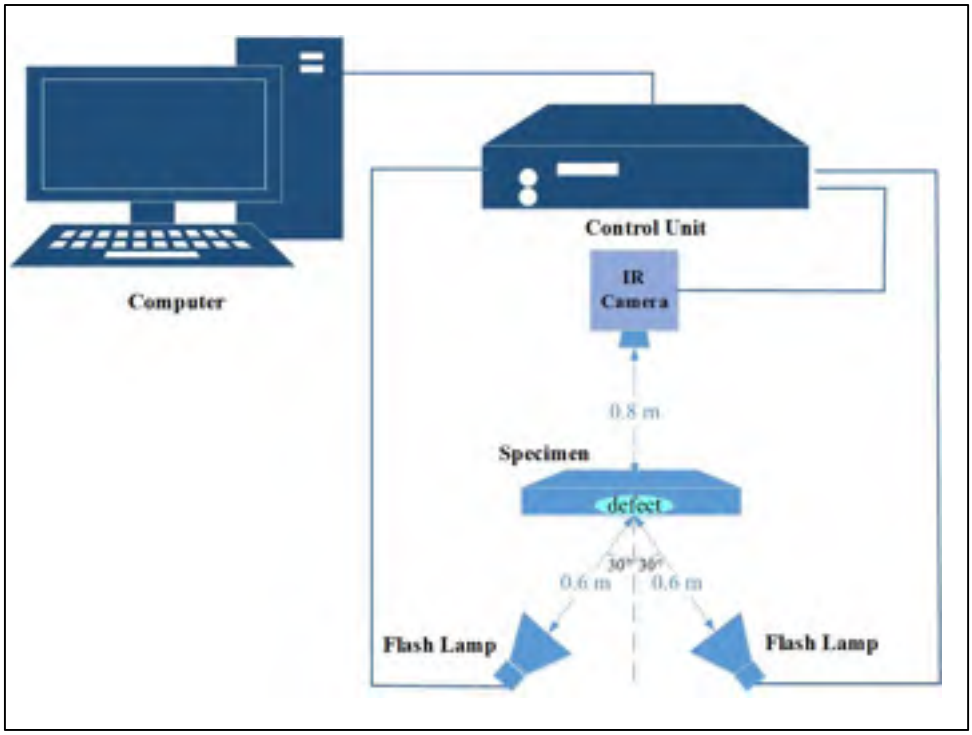

Figure 2-11 IRT transmission mode

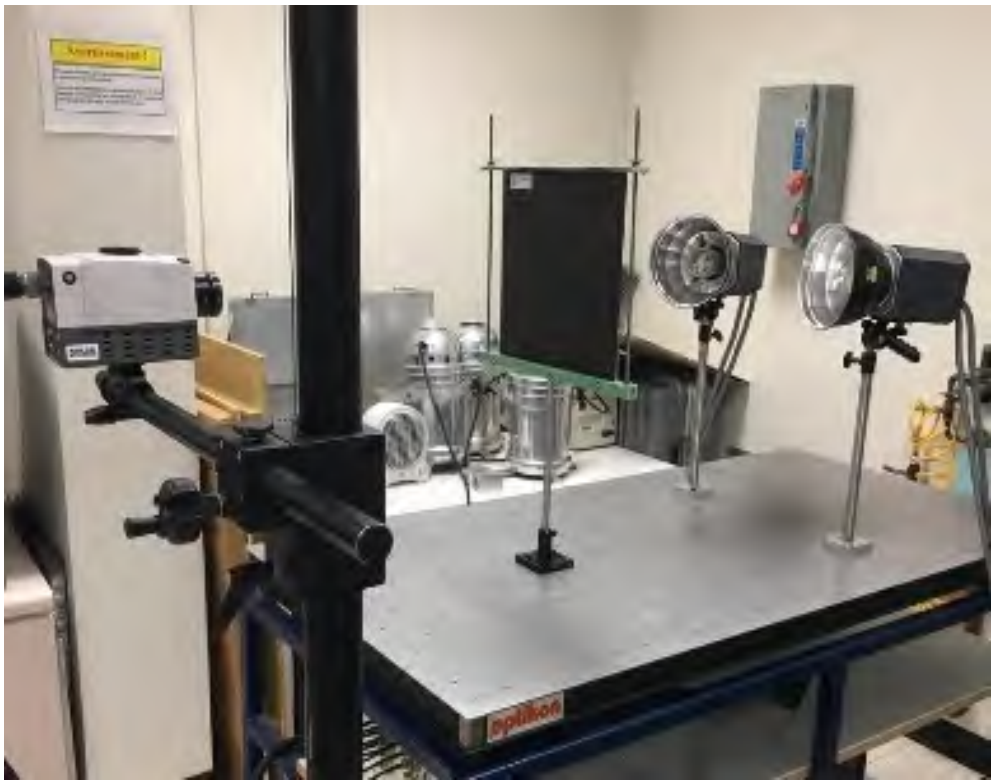

Figure 2-12 IRT transmission setup

2.7 Infrared thermography results

2.7.1 Reflection mode

Temperature profiles in Fig. 2-13 corresponds to a sound area, at the center of the not impacted sample (E), and the damaged zone in E2, E3 and E4 coupons. The sound area (E) temperature decreases until stabilization is reached, after which, the temperature changes are negligible. Theoretically, temperature decay curves for both the defective and the sound area should behave similarly at the first instants, ERT. At that time, the heat has not reached the defect yet. Accordingly, once the thermal pulse reached the defective area, the surface temperature will be higher above the defective zone. This situation remains from this moment to the stabilization time.

It should be noted that some uncertainties are shown in the practical thermal evolution. For instance, the temperature should be the same in the first instance for all the samples, which is

an indication of non-uniform thermal heating. The non-uniformity can be due to equipment ageing, external heating and cooling source and uneven optical properties of the surfaces [63]. For the next acquisition points, thermogram sequences, the temperature is higher for the severer impact damages. To plot the profiles, cold images are subtracted from the thermograms. The thermogram profiles are plotted by selecting 15 × 15 pixels at the impacted area and the center of the non-impacted sample, Fig 2-14 to Fig. 2-16. The thermal values are obtained by taking an average of the pixels' temperature.

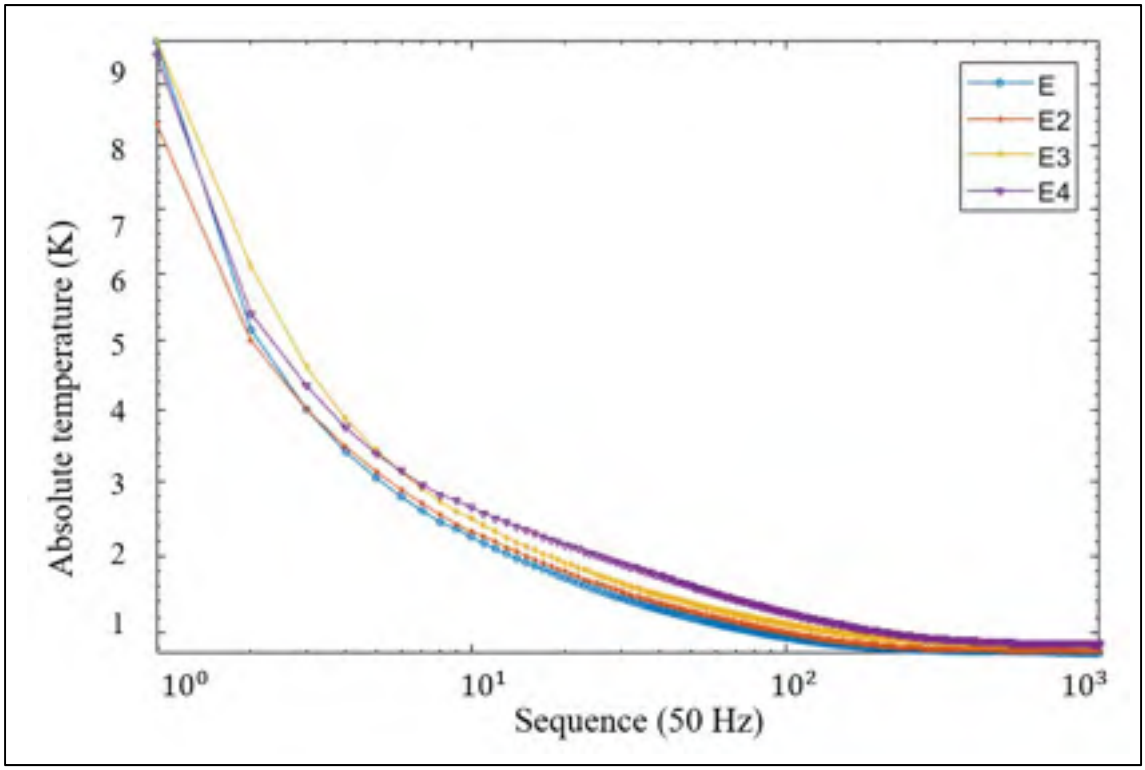

Figure 2-13 pixel intensity profiles correspond to raw thermogram

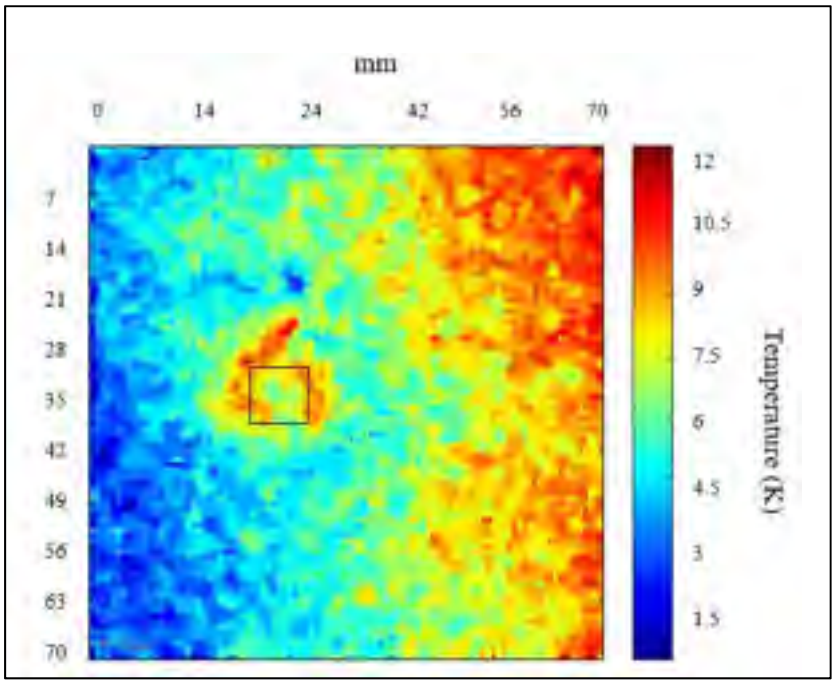

Figure 2-14 E2 raw thermogram at t = 0.66s

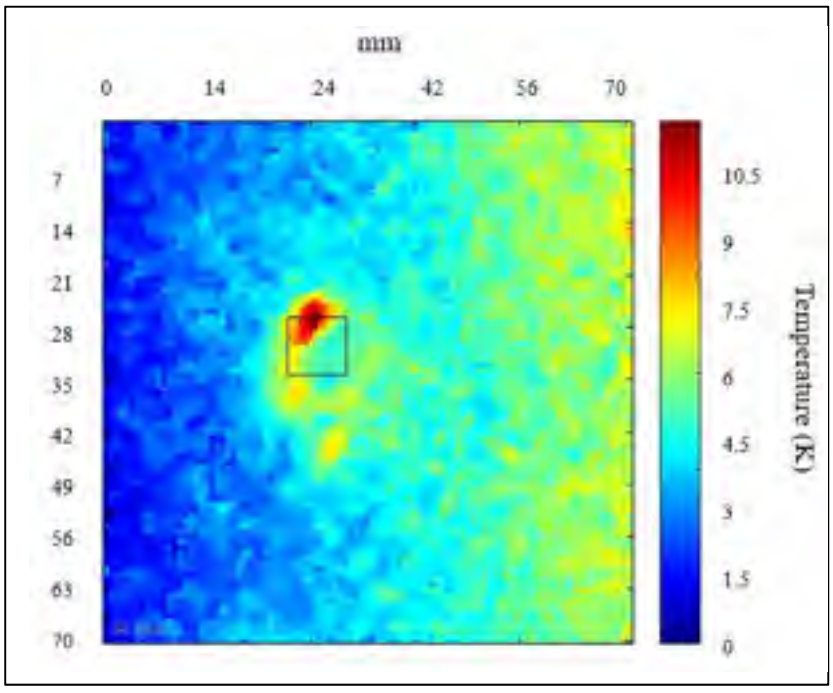

Figure 2-15 E3 raw thermogram at t = 0.66s

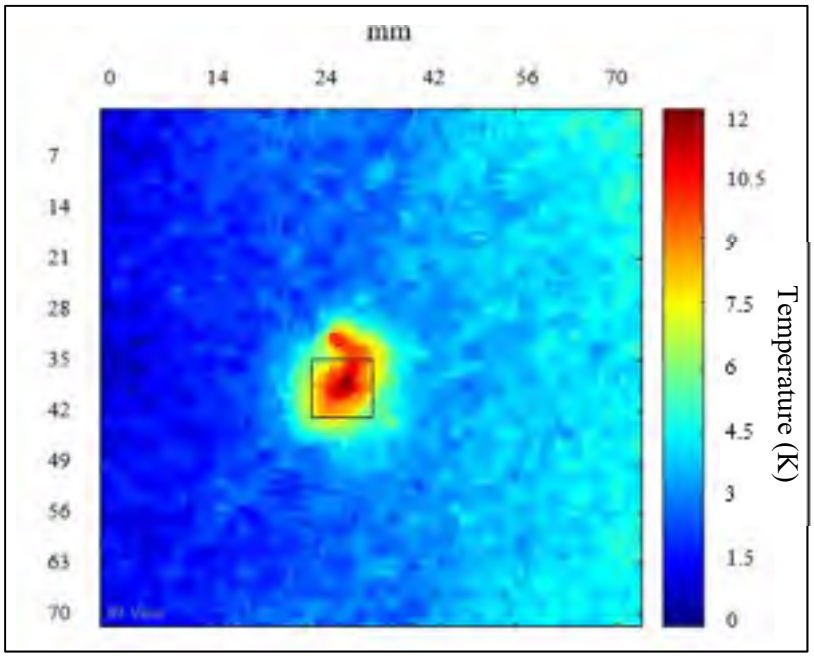

Figure 2-16 E4 raw thermogram at t = 0.66s

The experimental results of PT are shown in Fig. 2-14 to Fig. 2-16. The thermograms are captured after 0.66s, while the temperature scales are relative to the minimum in each region of interest. The defects are not visible clearly in PT thermograms other than E4. In this case, the indications sizing of E2 and E3 are not applicable. Additionally, the non-uniform heating of the specimen affects the quality of the thermograms.

2.7.2 Pulse phase thermography

Fig. 2-17 is showing phase shift versus frequency profile of the damaged area, in E2, E3, E4, and sound area, E. The phased graphs are calculated for the three identified 15 × 15 pixel square in Fig. 2-18 to Fig. 2-20 and at the center of sample E. While, the sampling frequency is f_s = 50 Hz, and the truncation window is selected as $w(t)$ = 20 s [63], [67].

Contrary to thermograms, phasegrams are quite insensitive to reflections from the environment. Also, unlike temperature data, the phase is practically undisturbed by non-uniform heating [63], [53].

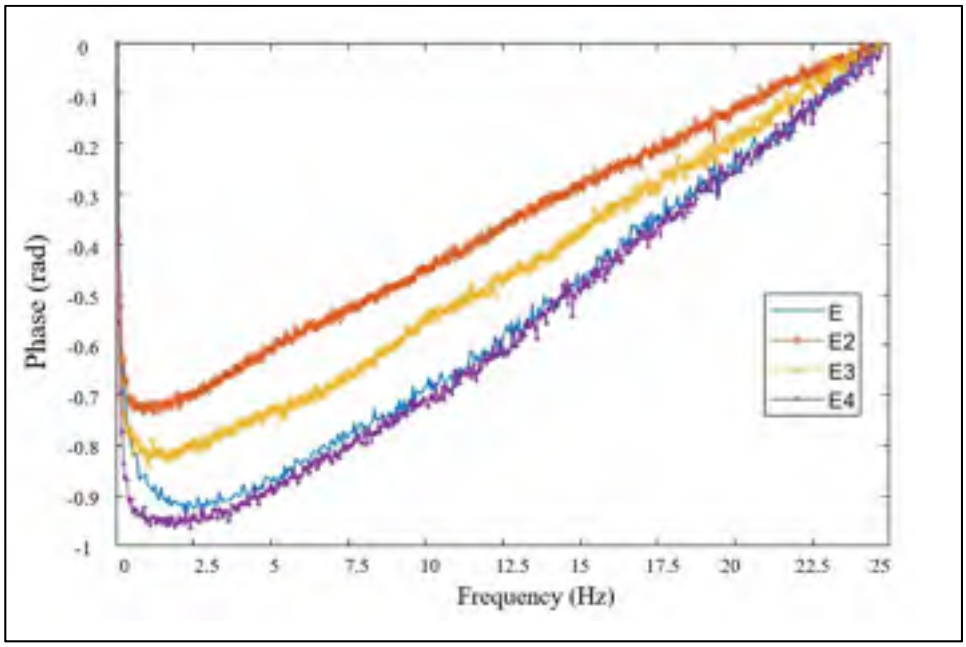

Figure 2-17 Phase graph of defective and non-defective (reference) area in E2, E3, E4, and E as a non defective sample

For PPT, the phasegrams was captured in the frequency of 0.2 Hz. To increase the phasegram quality, a median filter is applied by IR-view software [68]. As can be seen, the effect of non-uniform heating is removed in the graph, and all the defects are clearly visible in the phasegrams. Table 2-1 presents the size of the indications, whereas the flaw sizing is conducted according to ASTM E2582-07 [69]. Fig 2-21 to Fig. 2-26 presents the sizing conducted through the marked line, in Fig. 2-18 to Fig. 2-20, based on full-width of half-amplitude at the pixel size of 0.7 mm. Since the irregular boundaries of the multiple delaminations produce complex heat diffusion through the thickness, it may cause underestimate damage sizing in the PPT result.

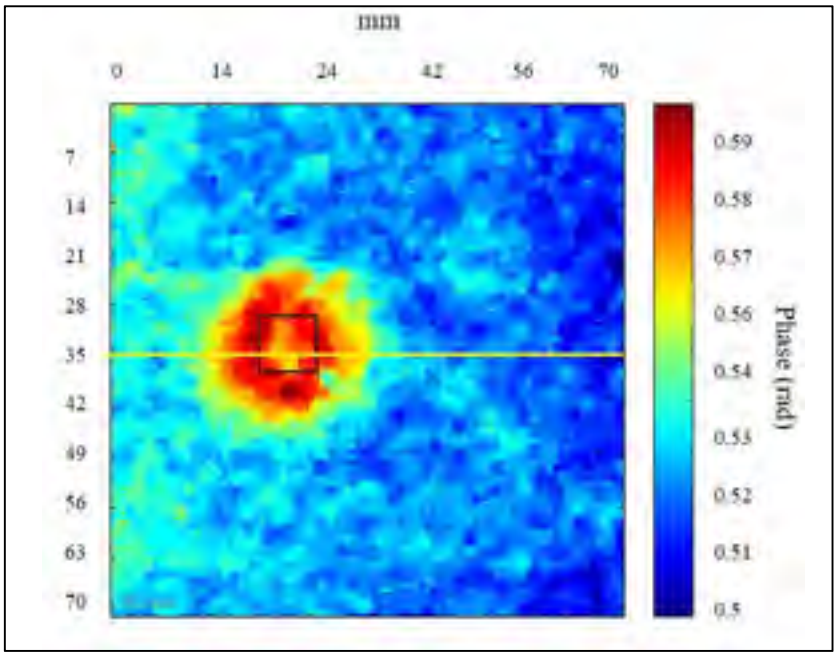

Figure 2-18 E2 Phasegram, at the frequency of 0.2 Hz

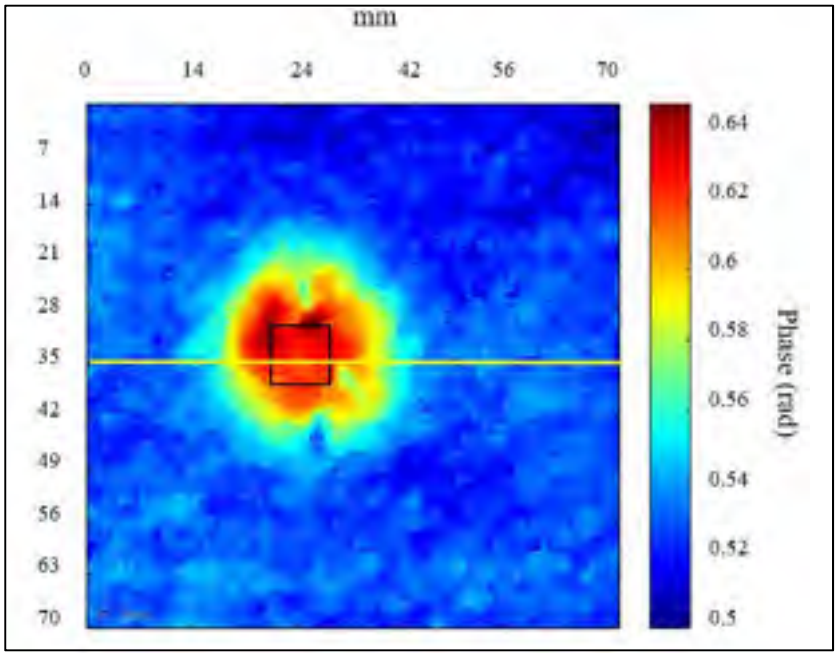

Figure 2-19 E3 Phasegram, at the frequency of 0.2 Hz

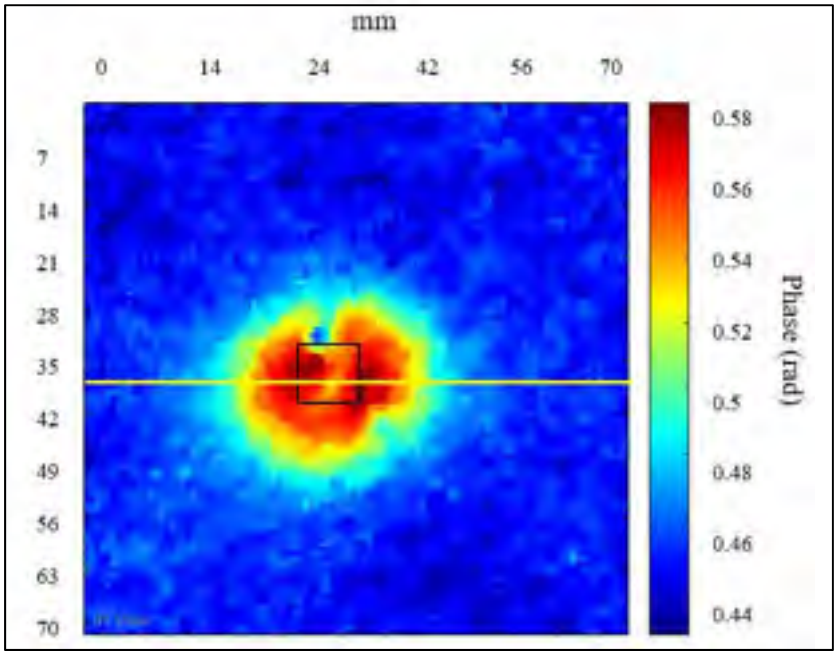

Figure 2-21 E4 Phasegram, at the frequency of 0.2 Hz

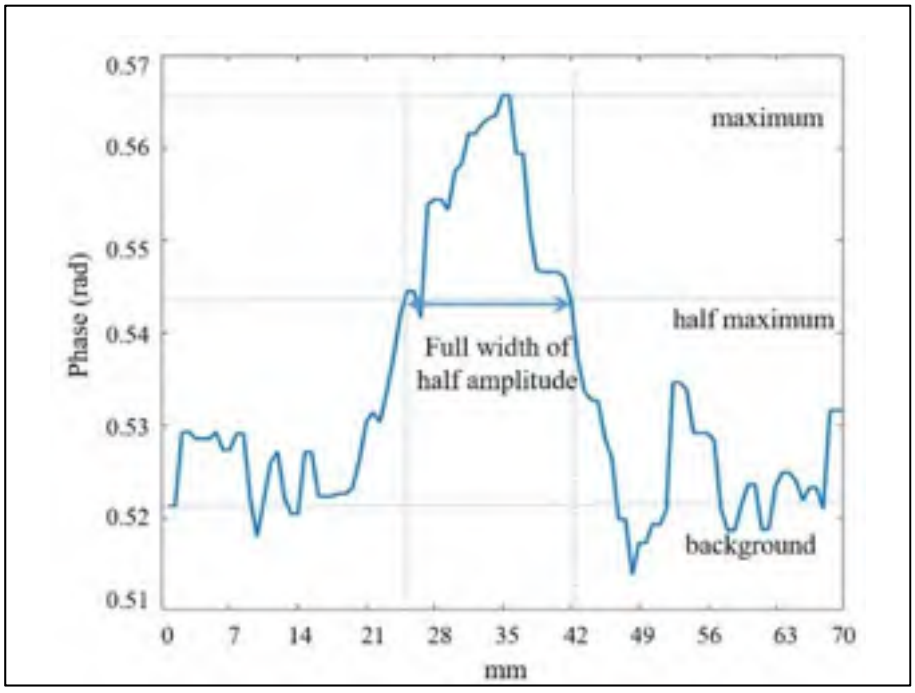

Figure 2-20 E2, indication sizing by full-width of half-amplitude

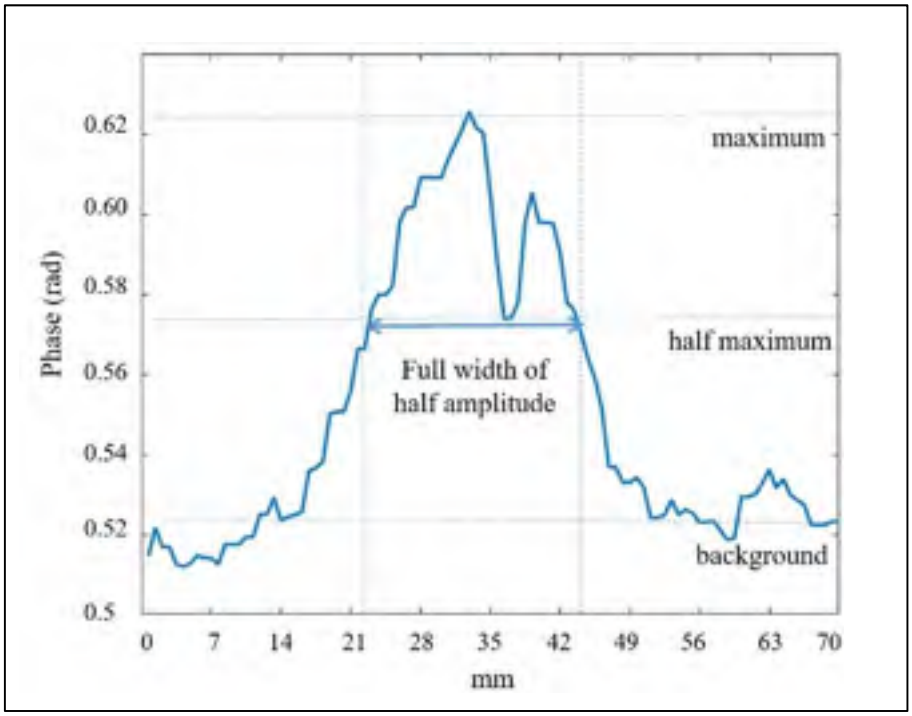

Figure 2-22 E3, indication sizing by full-width of half-amplitude

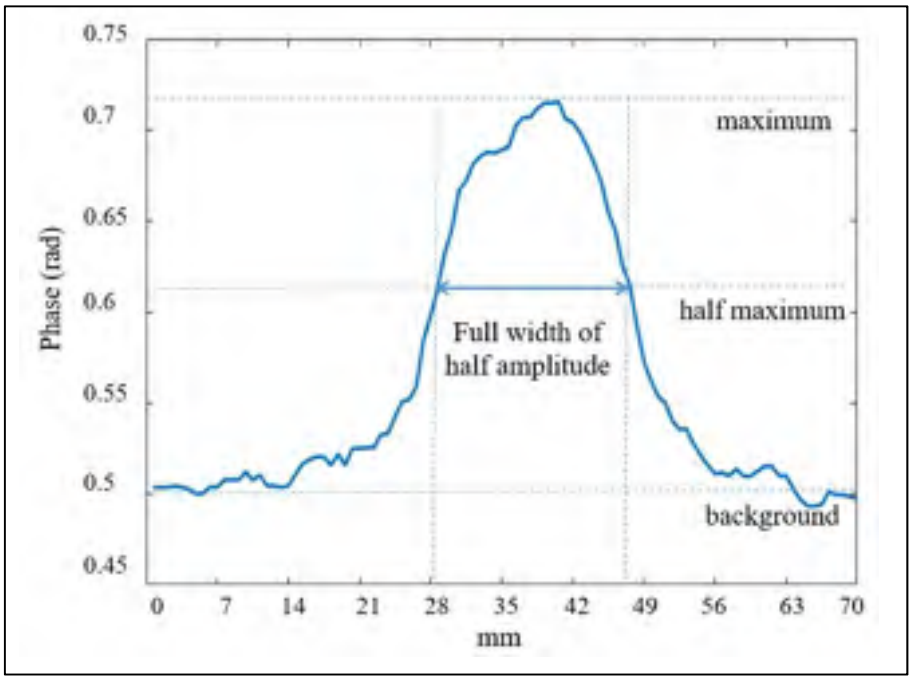

Figure 2-23 E4, indication sizing by full-width of half-amplitude

Table 2-1 Indication sizing by PPT

Coupons	PPT
	Area (mm^2)
E2	265
E3	346
E4	314

2.7.3 Transmission mode [8]

During applying IRT transmission technique, the back surface thermograms are captured. They reveal indications of the damages as areas with the temperature slightly less than the surroundings. After the processing, the thermographs by applying Eq. (2-6), (2-8), (2-9) and (2-10) thermal diffusivity map is obtained for the damaged area, Fig. 2-24 to Fig. 2-26. The map is constituted by taking an average of the values obtained from the diffusivity relations [65].

For quantitative interpretation, the thermal diffusivity values for each sample are determined. Fig. 2-27, to Fig. 2-30 illustrates the thermal diffusivity of the sound area (E) and impacted area in E2, E3, E4 samples. The experimental results show that the thermal diffusivity decreases with the level of impact damage. Table 2-10 presents the thermal diffusivity of the Samples. To do so, thermal profiles are plotted by selecting 15×15 pixels at the damaged area and the center of the non-damaged sample, identified in Fig. 2-22 to Fig. 2-24. The thermal values are obtained by taking an average of the selected pixels intensity.

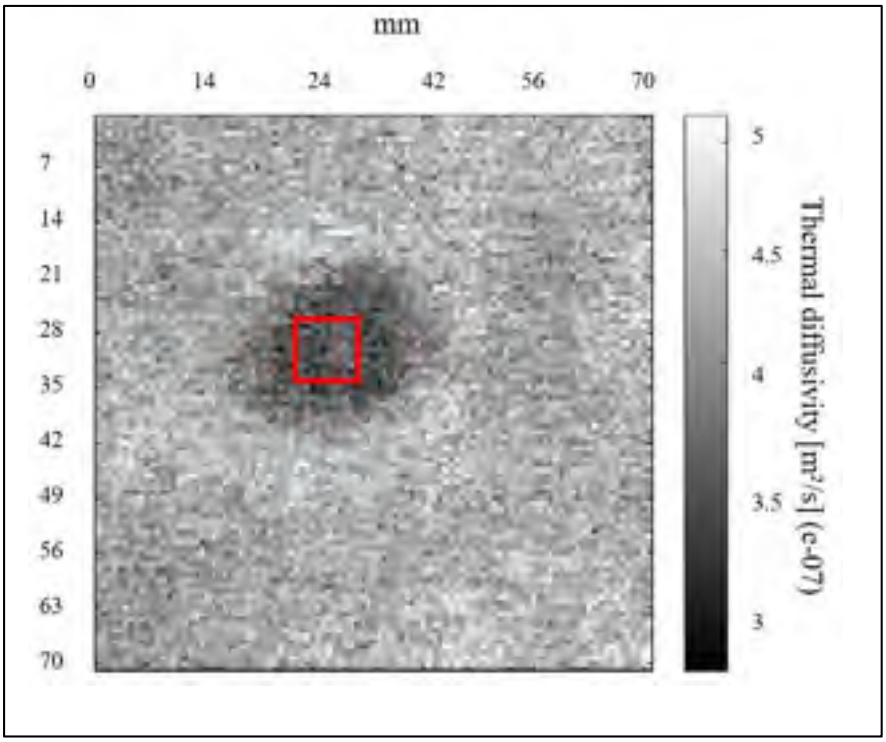

Figure 2-24 E2, diffusivity map

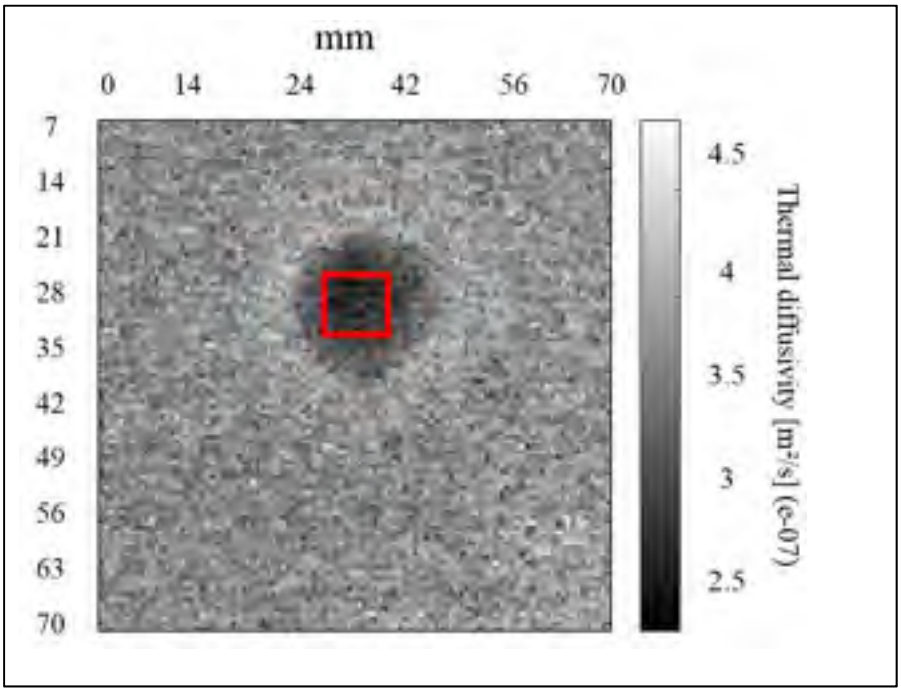

Figure 2-25 E3, diffusivity map

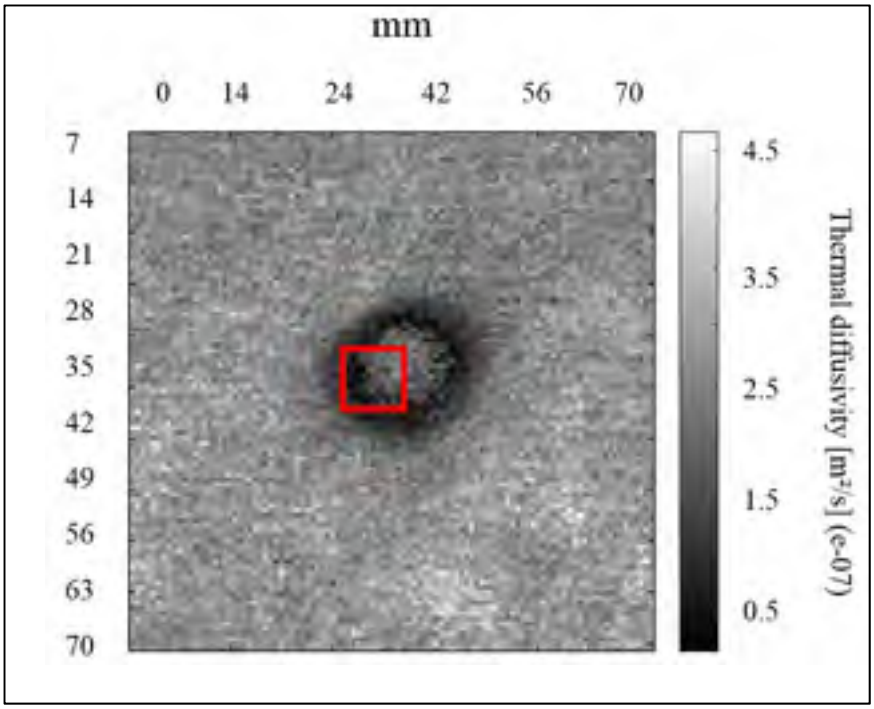

Figure 2-26 E4, diffusivity map

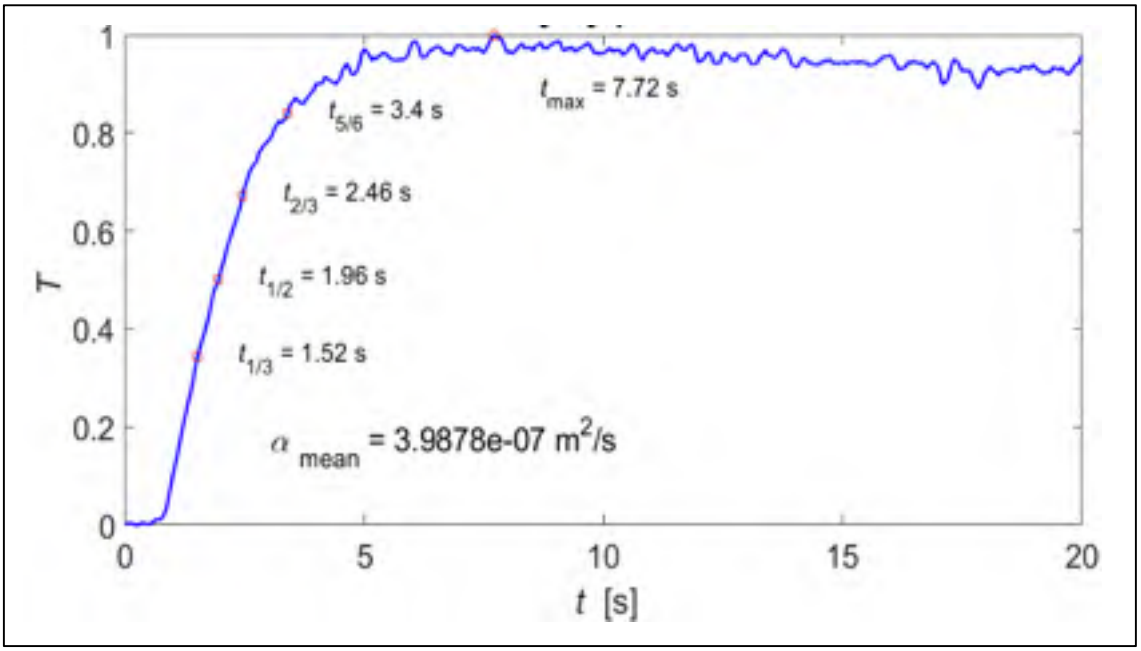

Figure 2-27 Applying a partial method to determine thermal diffusivity for the defective area in E

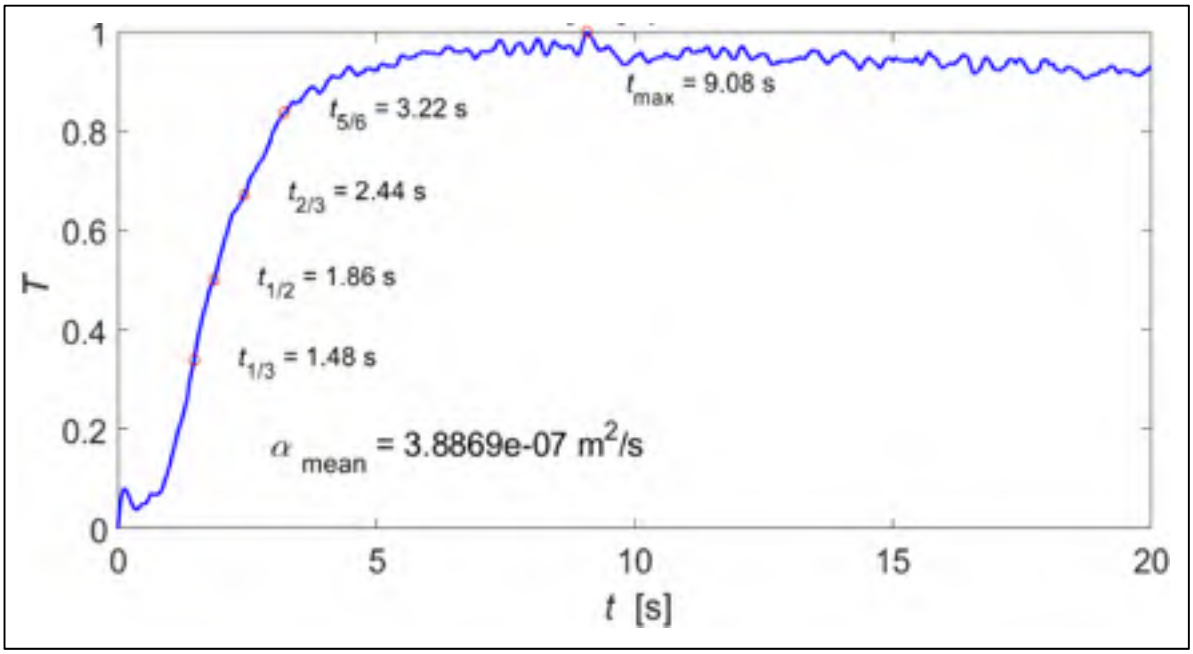

Figure 2-28 Applying a partial method to determine thermal diffusivity for the defective area in E2

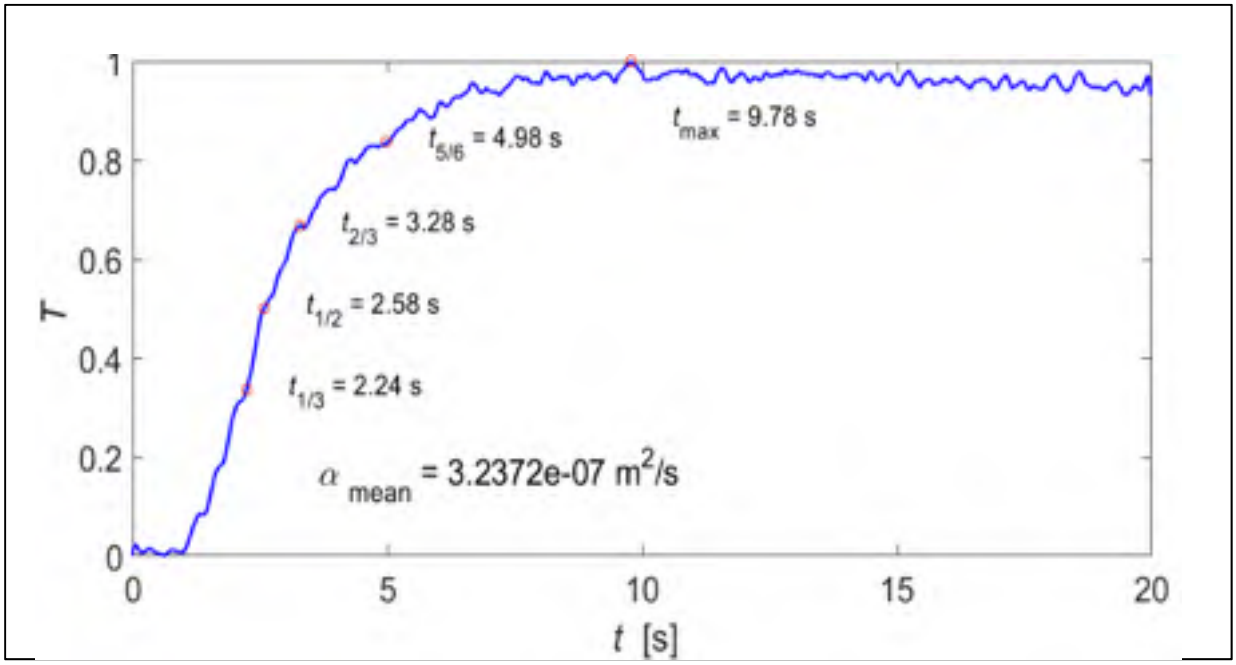

Figure 2-29 Applying a partial method to determine thermal diffusivity for the defective area in E3

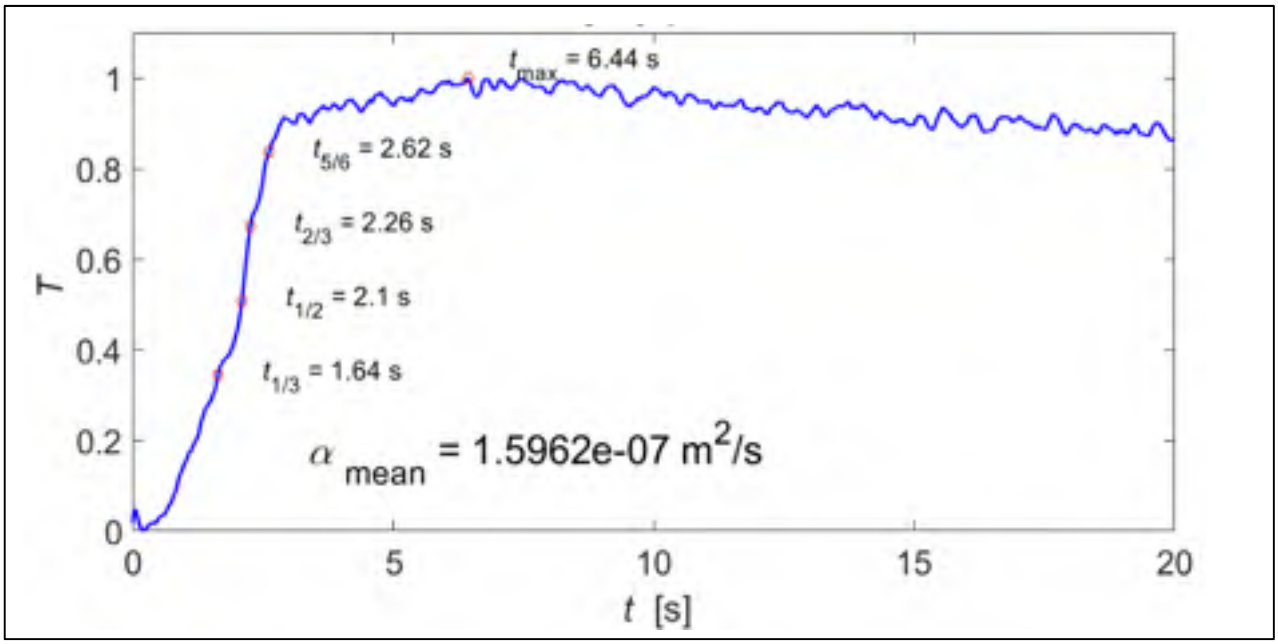

Figure 2-30 Applying a partial method to determine thermal diffusivity for the defective area in E4

Table 2-2 Thermal diffusivities for E, E2, E3, E4

Sample	E	E2	E3	E4
Thermal diffusivity [m²/s] (e-07)	3.987	3.886	3.237	1.596

CHAPTER 3

SHEAROGRAPHY TESTING

3.1 Overview

In this chapter, a shearography test procedure is applied to evaluate the impact damage in the three CFRP coupons. The results include wrapped and unwrapped phase shearogram, show that shearography is able to detect and size the damaged area. By means of the unwrapped phase map, the size of indications are measured. In the measurement, through the shearing direction, full-width of half-amplitude represents the diameter of the damaged areas while the wrapped shearograms illustrate, relatively, the severity of impact damages.

3.2 Introduction

Digital shearography is a full-field and real-time method to evaluate the integrity of composites materials. The applications of shearography are extended to strain measurement, material characterization, residual stress evaluation, leak detection, vibration studies and 3-D shape measurement [70]. However, one of the significant applications of the method is non-destructive testing on the composite structure [71]. Shearography is developed for aircraft applications. Airbus applied shearography for several CFRP inspection solutions. In the inspections, detection of in-service damage such as stringer debonding and impact damages are feasible [72]. This optical method is based on the interference of the laser speckle pattern to figure out the spatial derivative of surface displacement. The principle of speckle interferometry involved the comparison of speckle patterns which are recorded before and after an applied loading. Correlating the variation of the spackle patterns gives a fringe pattern. Besides, a processing method is needed to make a phase map from the fringe pattern. This phase map would be equivalent to a spatial derivative of surface displacement, where the discontinuity in laminated composites is visualized as anomalies of the strain on the surface [39].

3.3 Background

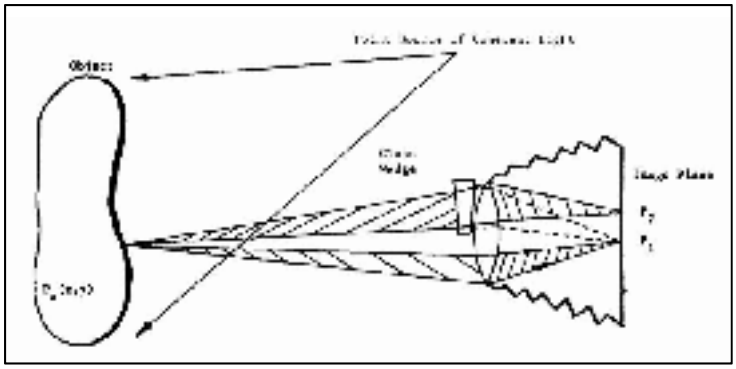

Figure 3-1 Schematic diagram of shearography, the rays from two adjacent point are brought to meet in the image plane [71]

Firstly, Hung introduced a schematic diagram of shearography. In the setup, a thin glass wedge placed in the iris plane of a lens. The wedge covers one half of the lens aperture. Therefore, scatter rays from one point on the illuminated surface, $P_0(x,y)$, mapped into two points, P_1 and P_2, in the image plane. Indeed, the optical configuration brings the scattered rays from one point on the object's surface to meet with those scattered from an adjacent point in the image plane. After a deformation in the test object, the pattern is changed, slightly. By subtracting the deformed from the un-deformed patterns, a shearography image is obtained. The image corresponds to the surface displacement gradient, of the deformed object [25].

Shearography testing has noticeable improvements by deploying practical optical configuration, such as a Michelson optical configuration, as a shearing device [73]. In the other development, in digital shearography, a video sensor is applied for data acquisition, while the data are processing by a computer [74]. Also, shearography has gained more flexibilities to environmental disturbances, including thermal drift, vibration, and rigid-body motion [75]. Therefore, it is adapted as a non-destructive testing method in automotive, rubber and aerospace industries to provide a proper structure evaluation method. In the following sections, the fundamental terms of shearography are discussed.

3.3.1 Principle of a digital shearography

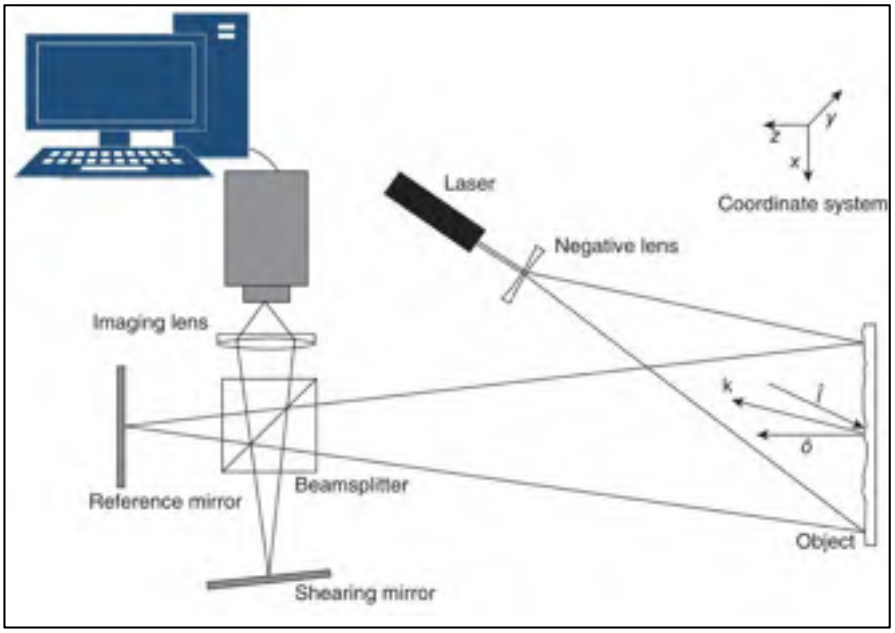

Figure 3-2 Schematic diagram of digital shearography. A Michelson configuration is used for shearing devices [39]

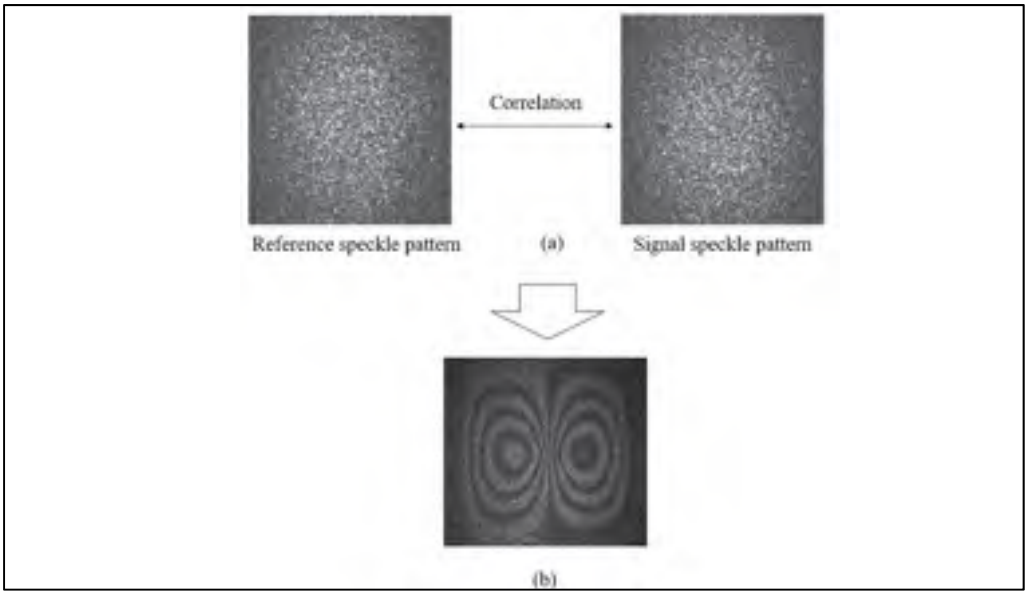

Figure 3-3 (a) Correlation of interferometric speckle patterns corresponded to before and after deformation, results in a fringe pattern, (b). The fringes show the displacement gradient of the object's surface [39]

Fig. 3-2 illustrates a schematic diagram of a digital shearography test. An expanded coherent light illuminates a test object while an optical component is placed in front of the camera lens. In the optical device, two non-parallel scattered rays, from two different points of the object, are brought to interfere with each other. The interference patterns are formed in an image sensor and recorded by a camera. If the illuminated surface is optically rough, the surface diffusely reflects the light. The interference of the scattered rays produces a random pattern known as a speckle pattern. By deforming the object, the speckle pattern is changing slightly. In a digital shearography test, the two sequential speckle patterns are compared. The patterns correspond to one before and another after the test object deformation. The difference between the two speckle patterns forms an interpretable fringe pattern. The pattern figures out surface displacement derivatives. Fig. 3-3 (a) and (b) shows the fringe formation process.
The fringe lines identify the place of the subsurface defects, where they form anomalies on the surface [39].

3.3.2 Fringe interpretation

In a shearography setup, when coherence light is scattered from the test surface, a granular pattern is formed in the camera sensor. It is because of the constructive and destructive interference of scattered light. The intensity distribution of the speckle pattern is given by:

$$I = I_0\left[1 + \mu\cos\phi\right] \tag{3-1}$$

Where;

I_0: is the background intensity of the speckle pattern

μ : amplitude of modulation of the speckle pattern

ϕ : is a random phase angle

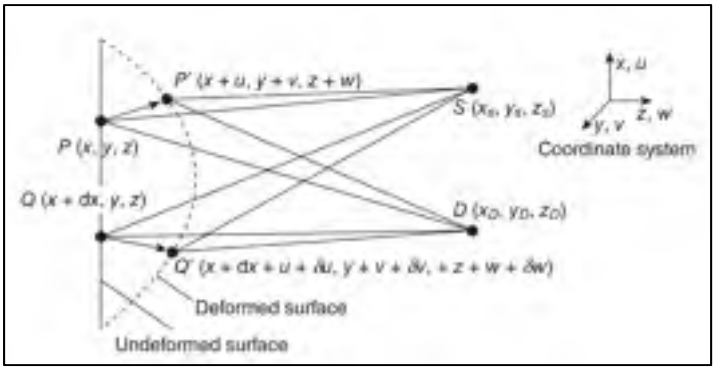

Figure 3-4 Diagram for derivation of optical path length change due to surface deformation [39]

In the same way, after the object deformation, the intensity distribution of the speckle pattern is changed to I'

$$I' = I_0\left[1 + \mu\cos\phi + \Delta\right] \tag{3-2}$$

Where;

Δ : is the phase change due to the surface deformation.

Computing the subtraction of the intensities of the two speckle patterns yields Eq. 3-3

Where;

$$I_d = 2I_0\left[\mu\sin\left(\phi + \frac{\Delta}{2}\right) + \sin\left(\frac{\Delta}{2}\right)\right] \tag{3-3}$$

I_d : is the intensity difference of a pixel due to the deformation

Eq. 3-3 shows the formation of a fringe pattern. When the function is minimized in $\Delta = 2n\pi$, where n is fringe order, the intensity corresponds to dark fringes, and the bright fringes are linked to half fringe orders.

3.3.3 Interpretation of the fringe pattern

As mentioned before, in a shearography test, an interferometric speckle is created by two laterally displaced by a shearing device. The optical component transfers scattered light from

each point on the object's surface to the image sensor, through two different paths. Therefore, the arriving light, at each pixel in the image sensor, is made up of light scattered from two points on the test surface [76]. In Fig. 3-4, point P on the object surface, placed at coordinates (x, y, z), is illuminated by a coherent light source located at S. The coherent light is scattered from P and follows a path through the shearing device. It will reach the detector at (x_D, y_D, z_D) coordinates, point D.

In the same way, light scattered from an adjacent point, Q at $(x+dx, y, z)$ coordinates, is received by the pixel D. Practically, P and Q are separated by a shearing distance, dx, and follows a different way to arrive at pixel D. After a slight deformation in the test object, P is shifted to P′ at $(x+u, y+v, z+w)$, where (u, v, w) is a displacement vector. While Q is shifted to Q′, $(x+dx+u+\delta u, y+v+\delta v, z+w+\delta w)$. The change in the light path length due to the deformation for the point P is given by
Where:

$$
\begin{aligned}
SP &= \left[(x-x_s)^2+(y-y_s)^2+(z-z_s)^2\right]^{1/2} \\
PD &= \left[(x-x_D)^2+(y-y_D)^2+(z-z_D)^2\right]^{1/2} \\
SP' &= \left[(x+u-x_s)^2+(y+v-y_s)^2+(z+w-z_s)^2\right]^{1/2} \\
P'D &= \left[(x+u-x_D)^2+(y+v-y_D)^2+(z+w-z_D)^2\right]^{1/2}
\end{aligned}
\tag{3-4}
$$

Eq. 4-4 can be simplified by Eq. 4-9 as:

$$\Delta L_P = Au + Bv + Cw \tag{3-5}$$

Where A, B and C are components of sensitivity vector, k, dependent on the observation

$$\Delta L_P = (SP' + P'D) - (SP + PD) \tag{3-6}$$

and illumination positions, Fig. 3-5.

k Defined as :

$$k = \hat{o} - \hat{i} \tag{3-7}$$

$$\Delta L_Q = A(u + \delta u) + B(v + \delta v) + C(w + \delta w) \tag{3-8}$$

When $\hat{o}$ is the observation angle, and $\hat{i}$ is the illumination angle, Fig. 3.2.
For Q, Eq. 4-8 gives the change in the light path length, similarly:
Therefore, the difference in changing the path length for Q and P is expressed as

$$\Delta L_Q - \Delta L_P = A\delta u + B\delta v + C\delta w \tag{3-9}$$

If the sheared distance is small compared to the observation and illumination distances, the difference in displacement between P and Q can be approximated by derivative displacement. As a result, for the optical phase difference of light from the adjacent points stated as:

$$\Delta = \frac{2\pi}{\lambda}\left(k_x \frac{\partial u}{\partial x} + k_y \frac{\partial v}{\partial x} + k_z \frac{\partial w}{\partial x} \right) dx \tag{3-10}$$

where k_x, k_y and k_z are the cartesian components of the sensitivity vector, k [76].

3.3.4 Out-of-plane sensitive shearography

In the Michelson optical configuration, the beam splitter separates the received light in two. Where half of the light is transited to the reference mirror and half reflected by the shearing mirror, Fig 3-5.

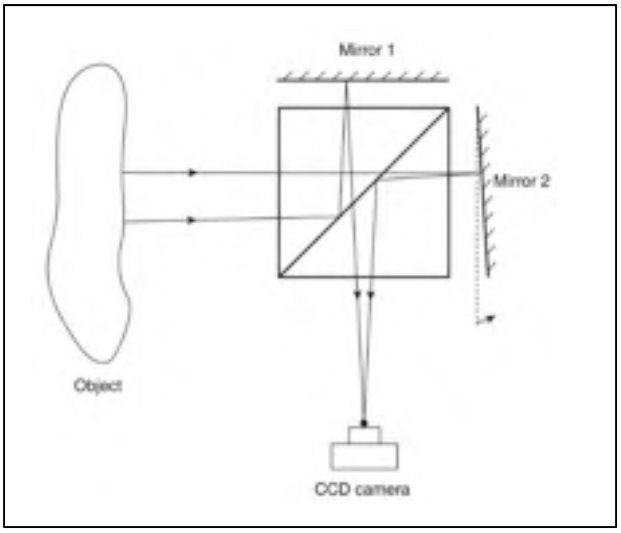

Figure 3-5 Michelson shearing interferometer
as a shearing device [39]

The shearing mirror is tilted at a slight angle. It results in an image that is shifted, laterally, relative to the one reflected from the reference mirror. The reflected images from the two mirrors form an interferometric speckle pattern at the camera sensor [76].

In most NDT applications, only the out-of-plane information is required. It means, in a shearogram, the measurement is isolated to obtain an out-of-plane component [77]. This information can be achieved by using an optical configuration so that each of A and B is approximately equal to zero. It will be obtained when the illumination and observation angle are collinear. In the case, Eq. 3-10 is reduced to Eqs. 3-11 and 3-12 [75].

$$\Delta_x = \frac{4\pi}{\lambda}\frac{\partial w}{\partial x}dx \tag{3-11}$$

$$\Delta_y = \frac{4\pi}{\lambda}\frac{\partial w}{\partial y}dy \tag{3-12}$$

Many developments have adopted shearography from a qualitative inspection tool into a system suitable for quantitative surface strain measurement [75]. The following sections describe a process in which the deformation phase-change Δ is directly determined.

3.3.5 Fringe phase determination

Phase stepping is a technique for quantitative measurement shearography. Due to a much higher contrast in shearograms, it is also applied for qualitative inspection. The phase stepping includes the recording of a series of speckle patterns with a specific phase difference and combining them by applying a phase stepping algorithm. The result would be a wrapped phase image. Phase stepping can be achieved by using a Michelson shearing interferometer when the reference mirror is imbedded on a piezo-electric transducer. In the method, by superimposing known phases, additional equations are generated Eq. 3-13. Even though there are several phase-shift algorithms, the four-frame algorithm is described here. Digitizing four speckle patterns with a $\pi/2$ phase-shift increment generates the following four equations [76]:

$$\begin{aligned} I_1 &= I_0\left[1+\mu\cos(\phi+0)\right] \\ I_2 &= I_0\left[1+\mu\cos(\phi+\pi/2)\right] \\ I_3 &= I_0\left[1+\mu\cos(\phi+\pi)\right] \\ I_3 &= I_0\left[1+\mu\cos(\phi+3\pi/2)\right] \end{aligned} \tag{3-13}$$

Therefore, the random phase ϕ is given as:

$$\phi = \arctan\left(I_4 - I_2\right)/(I_1 - I_3) \tag{3-14}$$

For the deformed speckle pattern:

$$\phi' = \phi + \Delta = \arctan\left(I_4' - I_2'\right)/(I_1' - I_3') \tag{3-15}$$

The obtained phases are wrapped into the range of $-\pi$ and $+\pi$. Finally, the deformation phase-change, Δ, is calculated by the following equation [78]

$$\Delta = \begin{cases} \phi' - \varphi & for \quad \phi' \geq \phi \\ \phi' - \varphi + 2\pi & for \quad \phi' \leq \phi \end{cases} \tag{3-16}$$

Different unwrapping algorithms have been developed to obtain the phase change distribution [39], [77], [76].

3.4 Shearography procedure and test parameters

In the shearography test procedure [53], a DANTEC Q-800 portable shearography system with eight lasers of 120 mW at a wavelength of 660 nm is used. The data are analyzed by ISTRA4D X 86 software. A heating lamp of 750 W is used to apply a thermal load for 15 seconds so as to induce deformation required for making the shearograms. The reference patterns are capture just after the heating time, and signal patterns are collected 10 seconds after the heating period. The heating source is placed at 0.5 m away from the sample at 45° from a normal angle of the specimen's surface. While the distance between camera and sample is 0.4 m at the normal angle, Fig 3-7.

Figure 3-7 Shearography test schematic

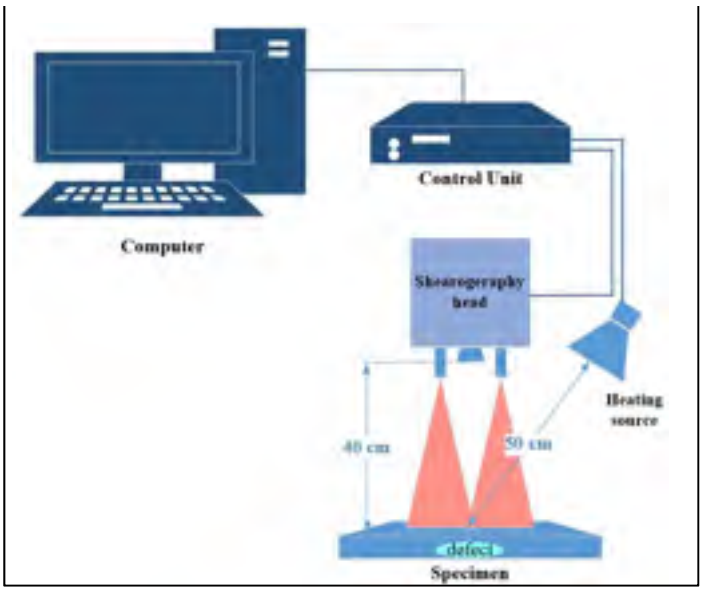

Figure 3-6 Shearography setup

3.5 Shearography results

The test results, unwrapped maps, demonstrate that all the impact damages are detectable in the test procedure, Fig. 3-8 to Fig. 3-10. The wrapped phase shearograms, Fig. 3-11 to Fig. 3-13, prove that the intensity of the impacts is corresponding to the fringe density. It can be considered as a promising feature of evaluation impact damage by shearography test [53]. To size, the indications, full-width half amplitude for the defective area in the shearing direction is applied. The indication sizes are 319 mm² for 10 J, E2, 389 mm² for 20 J, E3, and 419 mm² for 25 J, E4, impact energy for 2.4 mm shearing distance. Fig. 3-14 to Fig.3-16 are showing the indications central rows, through the yellow lines, or the variation of out-of-plane displacement gradient. The indication measurements are conducted on the unwrapped maps by the pixel size of 0.42 mm, Table 3-1. The shearograms prove that the size of the defects is related to the impact levels.

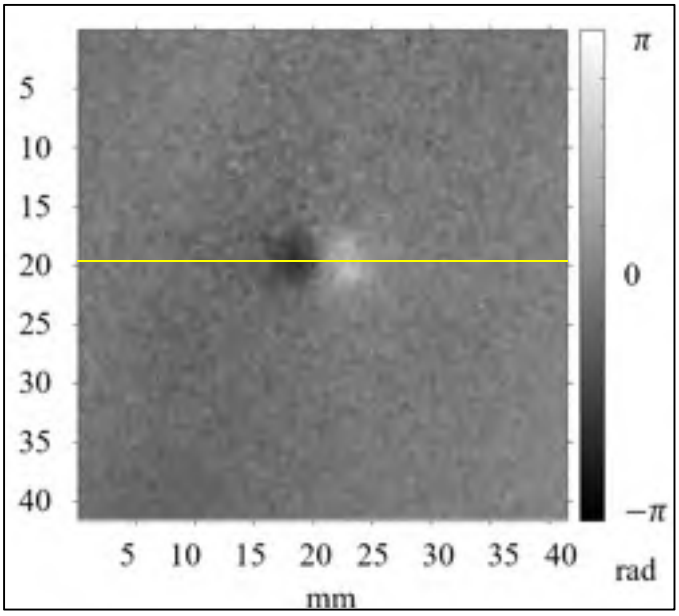

Figure 3-8 E2, unwrapped phase shearography result

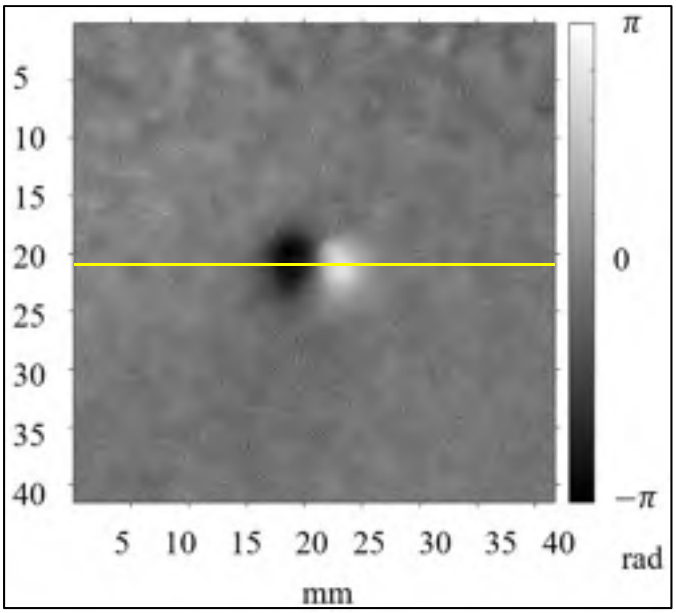

Figure 3-9 E3, unwrapped phase shearography result

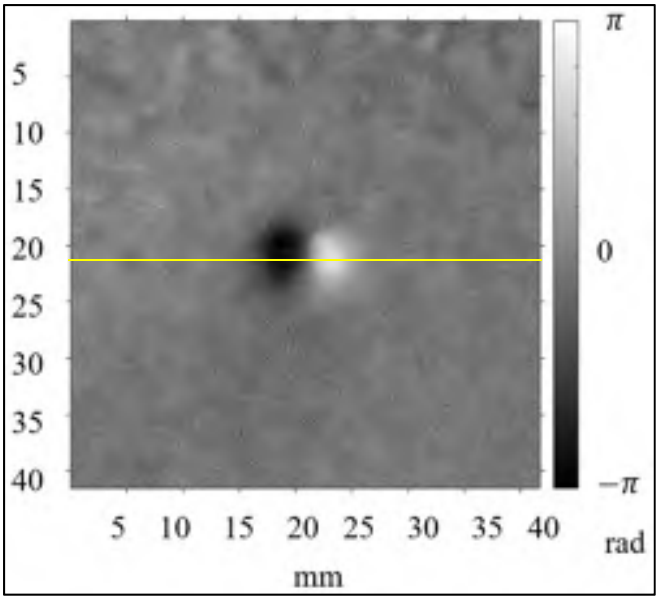

Figure 3-10 E4, unwrapped phase shearography result

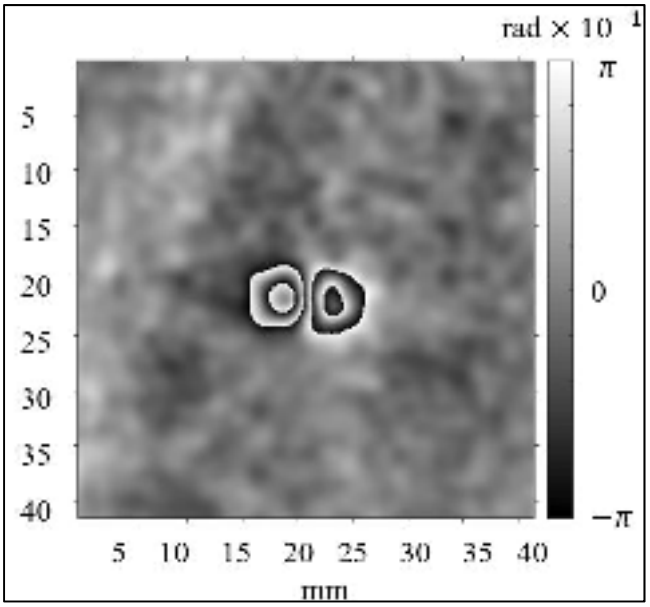

Figure 3-11 E2, wrapped phase shearography result

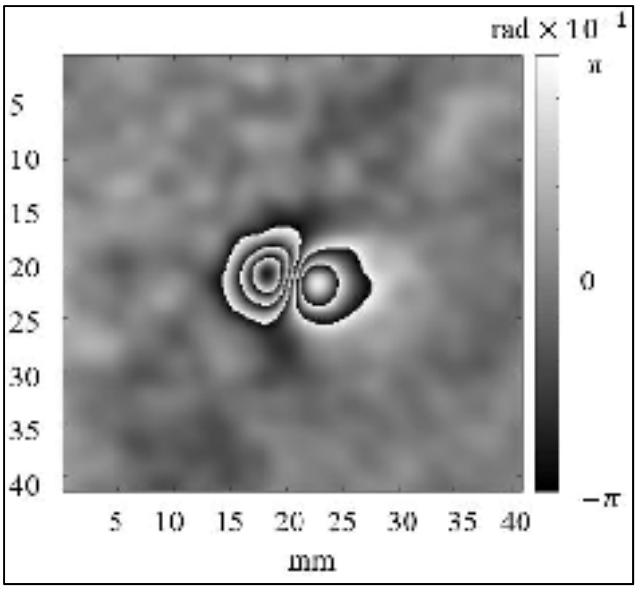

Figure 3-12 E3, wrapped phase shearography result

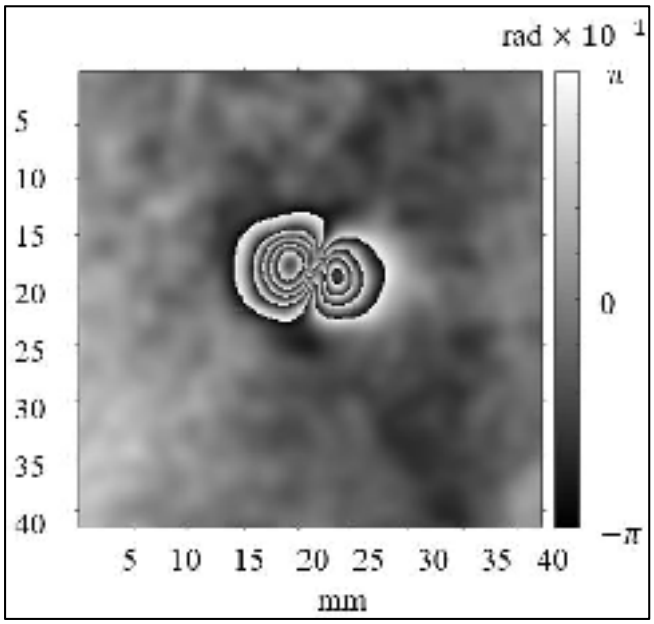

Figure 3-13 E4, wrapped phase shearography result

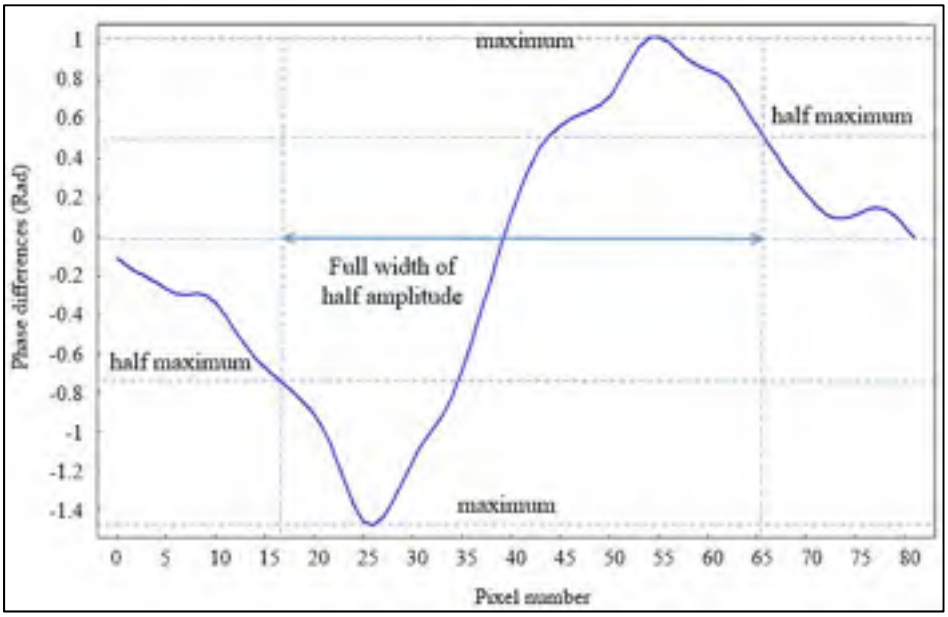

Figure 3-14 E2, indication sizing by full-width of half-amplitude

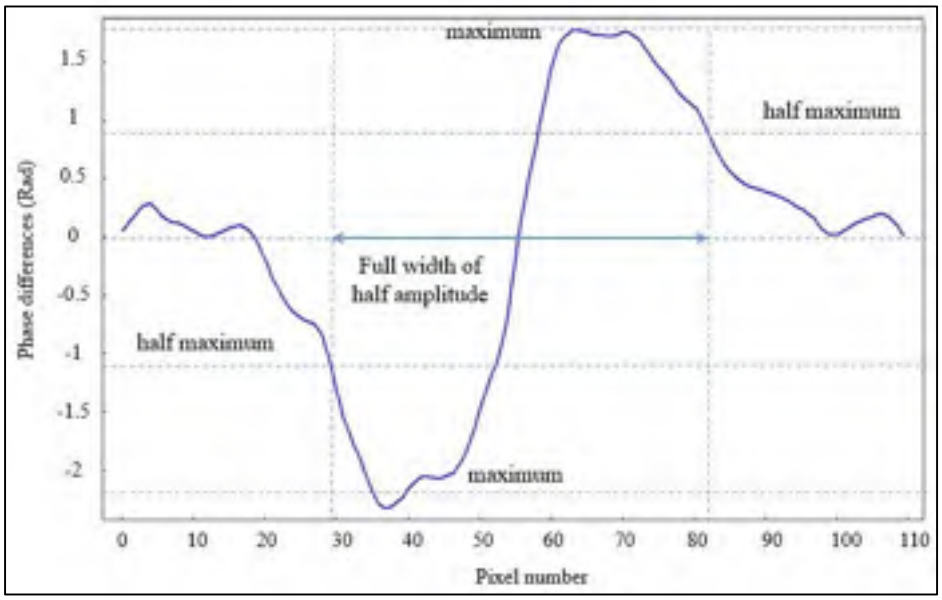

Figure 3-15 E3, indication sizing by full-width of half-amplitude

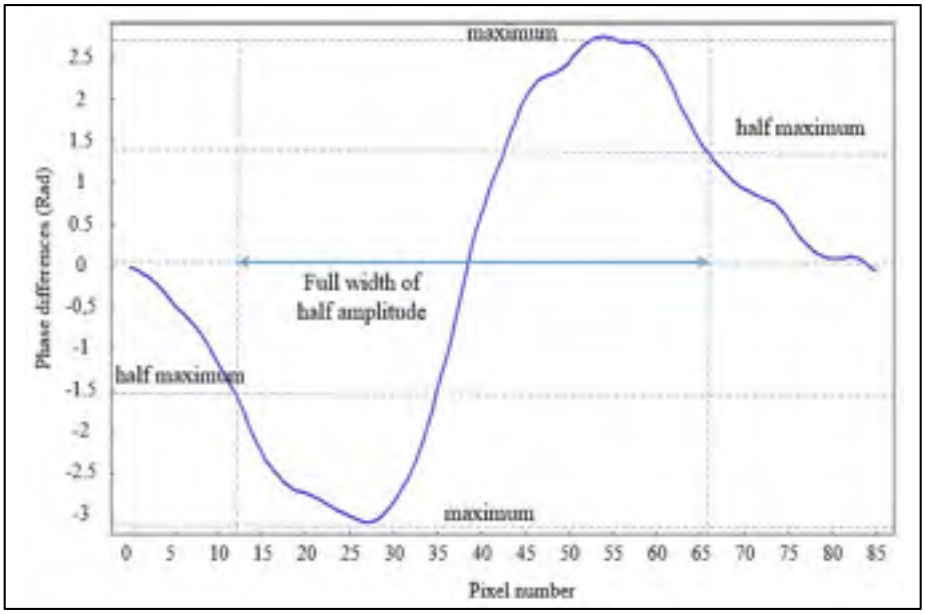

Figure 3-16 E4, indication sizing by full-width of half-amplitude

Table 3-1 Indication sizing in shearography

Coupons	Shearography
	Area (mm^2)
E2	319
E3	389
E4	419

CHAPTER 4

NDT SIMULATION

4.1 Overview

Due to the inhomogeneous nature of the CFRP, in the case of IRT and shearography testing, a complete comprehension of the test's physics is a challenging task. Therefore FEM tools are used to enable inspectors and researchers to predict the signals of a real test. This prediction has been applicable by analyzing the thermal and structural behaviour of the specimen in the test conditions.

In this study, numerical modelling simulations are made based on experimental tests. In this regard, ANSYS, as an FEM analysis tool software, is deployed to simulate the thermography and shearography. Besides, MATLAB is used to calculate phased thermograms and shearograms. In this practice, it is tried to simulate test models based on the real test that has been conducted in the experimental part of the study. Lastly, discussion and conclusions are made about the impact of test parameters on the NDT signals.

4.2 Introduction

As mention before, due to difficulties in the analysis of thermo-mechanical NDT signal in the composite material, a combination of Finite Element Modeling (FEM), signal prediction, and the experimental test is conducted. This is an appropriate tool to provide effective defect detection procedures in the NDT methods [79], [44].

Damage in a composite material caused by low-velocity impact mostly contains the matrix cracks, delamination, and fibre breakages. The delamination is known as the primary cause of the thermo-mechanical signal in the thermography and shearography test [61], [80]. In this regard, to evaluate the influence of different test parameters on the test signals, debonding is modelled as the essential feature of impact damage. The active thermography simulation results allow optimizing the test parameters, such as thermal pulse parameters, thermogram observation time and frequency. In the case of shearography, a proper NDT procedure depends

on some factors such as loading methods, boundary conditions, the shear amount and its direction. In a real test, knowing a proper arrangement of all these parameters is essential to avoid trying various procedures to find an optimal technique. It would be achievable by having an accurate numerical model of the tests [56], [81].

Basically, the simulation results, compared to experimental, do not have to be the same values. Numerous causes make the differences between experiment and simulation results. These factors can be included a combination of non-uniform heating, emissivity variations, environmental factors, and imperfect thermo-mechanical boundary condition. However, qualitatively, they are supposed to behave in a particular way. This can lead to the validation of the simulation result, and consequently, optimization of the test parameter is achievable by the simulated model.

The following steps are required to generate the numerical test model [56]:

- Geometry generation
- Defining material properties
- Defining mesh configuration
- Identify boundary conditions and contacts
- Obtain the result
- Processing the result

In this work, the finite element simulations are carried out using the ANSYS R19.2 Academic package. The software provides the possibility of manually defining layers on simple or complex composite geometry and layer-level analysis. By comparing the ability of different commercial software, it is found that; the most often used commercial softwares, such as ABAQUS, COMSOL and ANSYS, have the ability to analyze such simulations properly. Therefore base on the industrial partners' preference, ANSYS is applied in the research. Hardware configuration to run the software is Intel ® Xeon ® 3.30 GHz and 16.0 GB RAM. The software package contains an ANSYS Composite PrePost (ACP) module. It allows for solving the transient heat transfer and static structural problems for layered composites, Fig. 4-1.

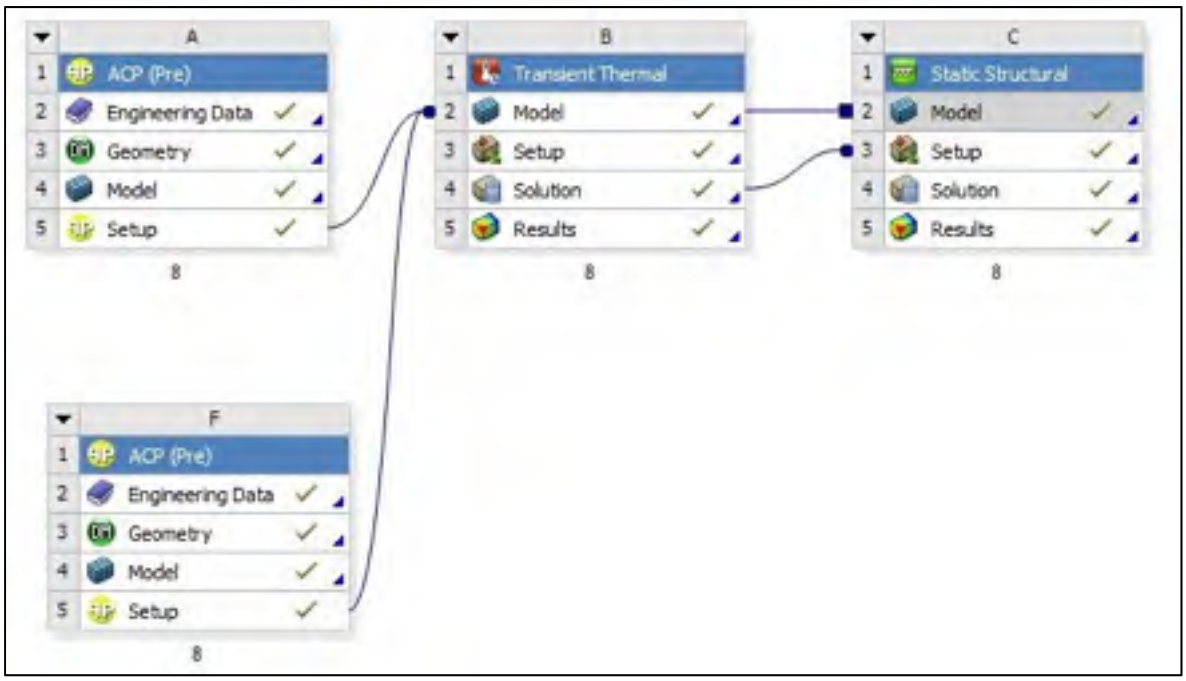

Figure 4-1 ANSYS modules used for the shearography simulation

4.3 Geometry generation and material properties:

ACP module can produce a model of a laminar composite, layer by layer. In the model, the fibre direction and layer thickness are defined according to the real samples, Fig 4-2. Therefore, all of the specimen dimensions used in the model. The dimensions of the sample are 300 mm × 300 mm, and 2.4 mm for the thickness. The diameter of the delamination is considered by 25 mm, which can be defined in different depths.

Moreover, the thermo-mechanical properties of the anisotropic composite model are defined in the software. Table 4-1 presents the properties of a layer in which the fibres are extended along the x-direction [82], [83].

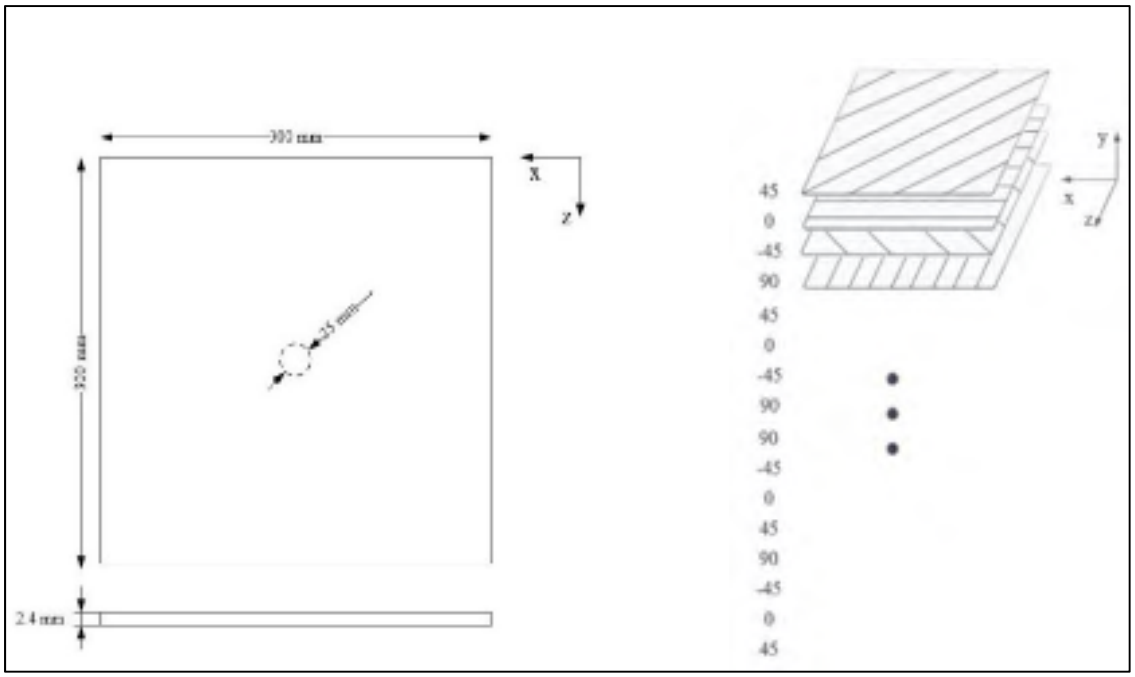

Figure 4-2 Model dimensions and configuration

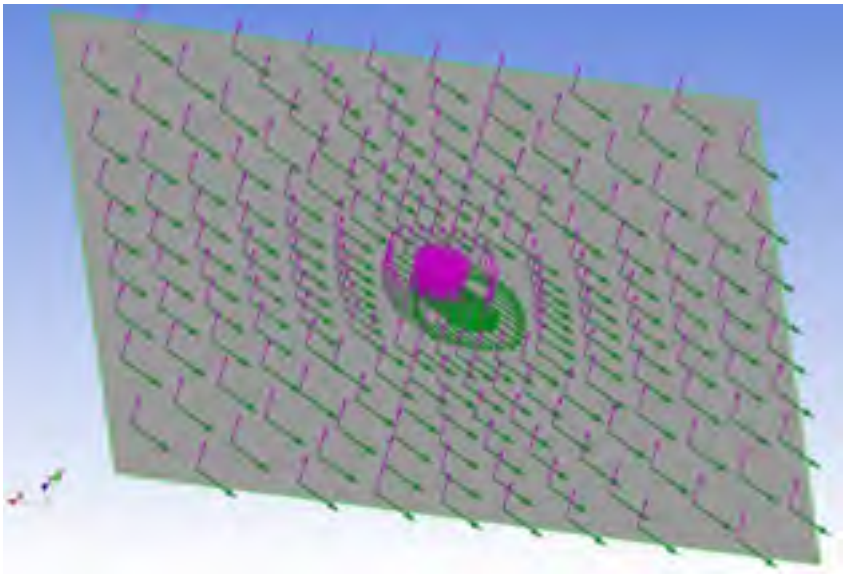

Figure 4-3 ANSYS Composite PrePost environment, in a particular layer, it is showing the direction of fibers, in green, and layup, in purple,

Table 4-1 Thermo-mechanical properties of a layer in which the fibres are extended along the x-direction. E: Young's modulus, G: Poisson's ratio, γ: shear modulus, K: thermal conductivity, C_p: specific heat and α: thermal expansion coefficient value

Properties	Value	Properties	Value
E_x	1.6e5 MPa	K_x	4.2 W/mK
E_y	9000 MPa	K_y	0.7 W/mK
E_z	9000 MPa	K_z	0.7 W/mK
G_{xy}	0.2 MPa	C_p	840 J/kg K
G_{zy}	0.046 MPa	α_x	-7.9e-7 1/K
G_{xz}	0.2 MPa	α_y	3.59e-5 1/K
γ_{xy}	6900	α_z	3.59e-5 1/K
γ_{yz}	4300		
γ_{xz}	3800		

4.4 Meshing

In order to obtain a good description of the heat transfer and strain measurement process in the debonded area, mapped meshing is applied instead of automatic meshing to create a fine mesh in the area, Fig. 4-4. In the mesh configuration, 5632 hexahedral elements, SOLID186, are used.

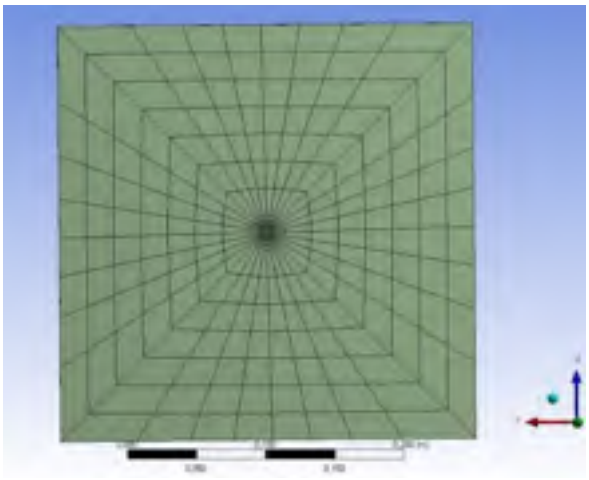

Figure 4-4 Mesh configuration

4.5 Boundary condition

To simulate thermal boundary conditions, heat flux is induced in the y-direction to one surface, and the natural convection coefficient in the ambient temperature of 293.27 K is considered for all surfaces by 10 $Wm^{-2}K^{-1}$.

In the case of shearography simulation, the same as thermography, for signal prediction, loading is required. The conditions of appropriate loading vary from case to case. The proper loading condition must produce local strains around the defects. In such a case, strain anomalies are produced on the surface over the defected area. Hence in this simulation, for the mechanical constraints, the boundary condition is defined which the object can undergo out-of-plane (y-direction) deformation, Fig. 4-5. Therefore, two roller boundary conditions are defined at each of two opposite edges, Edge1 and Edge 2, to limit the motion in x and y directions. To avoid rigid body movement (rotation) a corner is limited to move in the z-direction (Point 1). To initiate the deformation, a small amount of pressure, -10 Pa is applied to the heated surface. Fig. 4-5 shows the deformation of the modelled panel after applying the thermal load. To simulate the debonded area, frictionless contact is defined [84], and for the region, thermal conductancy of 1 $Wm^{-2}K$ is applied to make a thermal interface in the area.

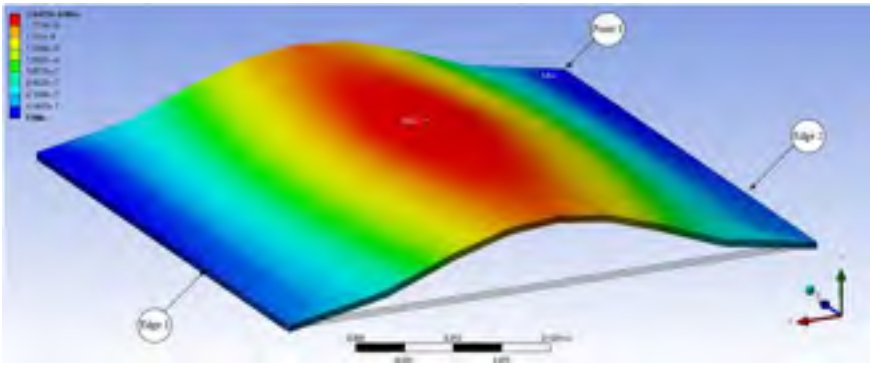

Figure 4-5 Deformation of the simulated model after applying thermal load

4.6 Thermography simulation and results

In the simulation of pulsed thermography, the test consists of a brief thermal stimulation, 65 ms, by applying a heat pulse into the test object's surface. After the heat energy stimulates a surface, temperature profile for a non-defective panel decays by the cooling time, at the center point of the heated surface, Fig. 4-6. In this graph, the other temperature profiles correspond to a point at surface over the debonded region in different layers, 2^{nd},4^{th}, 8^{th} and 12^{th}. In this method, defect detection is based on thermal contrast between defected and non-defected areas. Basically, the temperature evolution of a point at the surface, over defect or sound area, gradually is stabilized after the heat pulse. In this way, the temperature for the shallower delamination is more elevated in the acquisition points, while the temperature decreases abruptly for the deeper defects. PPT is conducted for the thermal signals by Matlab software. The profiles in this graphic correspond to the positive part of the phase spectra. The phase delay data along frequency are plotted for a sampling frequency of 50 Hz and 20 s truncation window. Fig. 4-7 shows the phase profiles for debonding in different layers and the sound area. With considering the sound graph as a reference, It can be seen that shallower delamination has higher contrast compared to the deeper ones. The simulated profiles can be validated by ideal debonding in the specific layers.

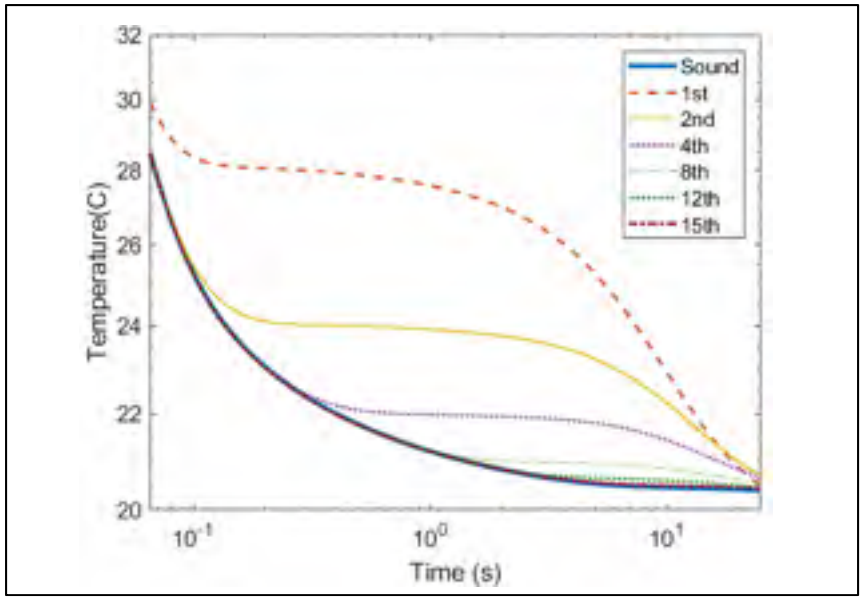

Figure 4-6 Cooling curve of the surface over the defected area and sound area of the simulated laminate after heat pulse

The next practice shows how the size of the truncation window, $w(t)$, affects the resulting spectra. This is illustrated in Fig. 4-8. The profiles in this graphic correspond to the positive part of the phase spectra for a debonding in the 8th layers, calculated by FFT for five truncation windows. As can be seen, for a constant sampling frequency (f_s =20 Hz), there is a loss of information related to the use of smaller w(t), especially at low-frequency components [63].

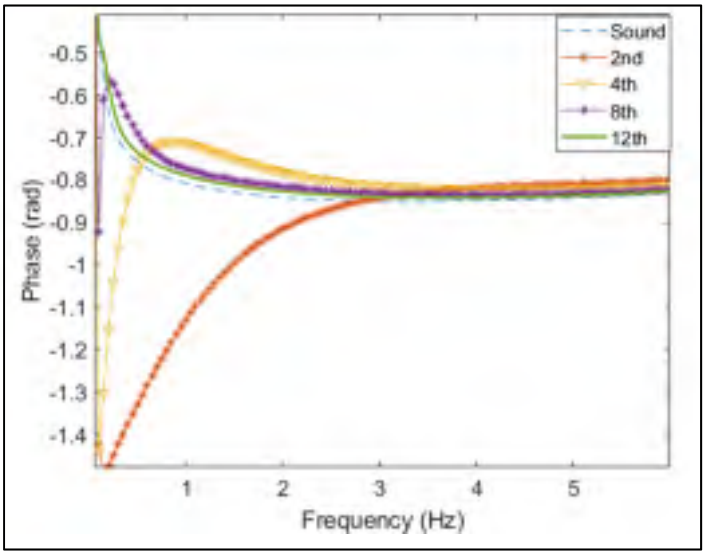

Figure 4-7 Phase profiles for debonding in different layers and sound area

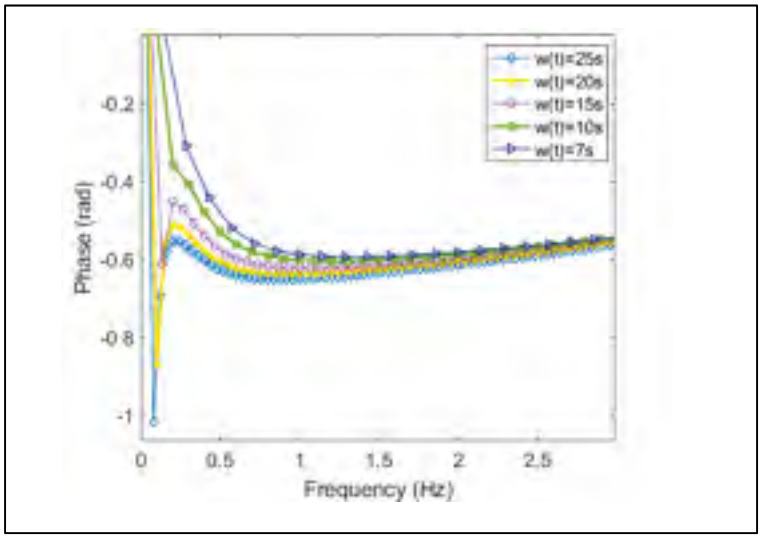

Figure 4-8 Impact of the size of the truncation window on phase for a delamination at 8th layer, fs=3 Hz

4.7 Shearography simulation

The improvement of shearography test procedures has become an improvement in the practical use of stimulating the test object that would reveal flaws. Theoretically, the stressing should be similar to in-service stresses. Therefore, flaws that are critical for the loading would be indicated. The critical factor in developing a particular loading is constraining the rigid-body motion in the object during the test; the motion leads to degradation of fringe quality [39]. The method that is used in this simulation does not cause the rigid-body motion. In this simulation, the thermal load is applied to induce deformation in the model. A surface of the model is subject to a square heat flux of 1000W/m² in 5 s to stimulate the model.

As explained before, a shearogram is the phase difference, which is corresponded to the out of plane displacement difference between two points separated by the shear distance. To simulate the phase image, firstly, the out of plane displacement is subtracted from a sheared version of itself. These values are converted into the phase difference value. The difference is identified by Eq. 4-1 [85]. Where;

w : the out-of-plane displacement

i : pixel number in the shearing direction

δ : shearing amount

$$\Delta\phi = \frac{4\pi}{\lambda}(w(i) - w(i - (\delta i)) \tag{4.1}$$

Fig. 4-10 is showing a typical procedure of calculating phasegram after applying heat pulse to a composite model.

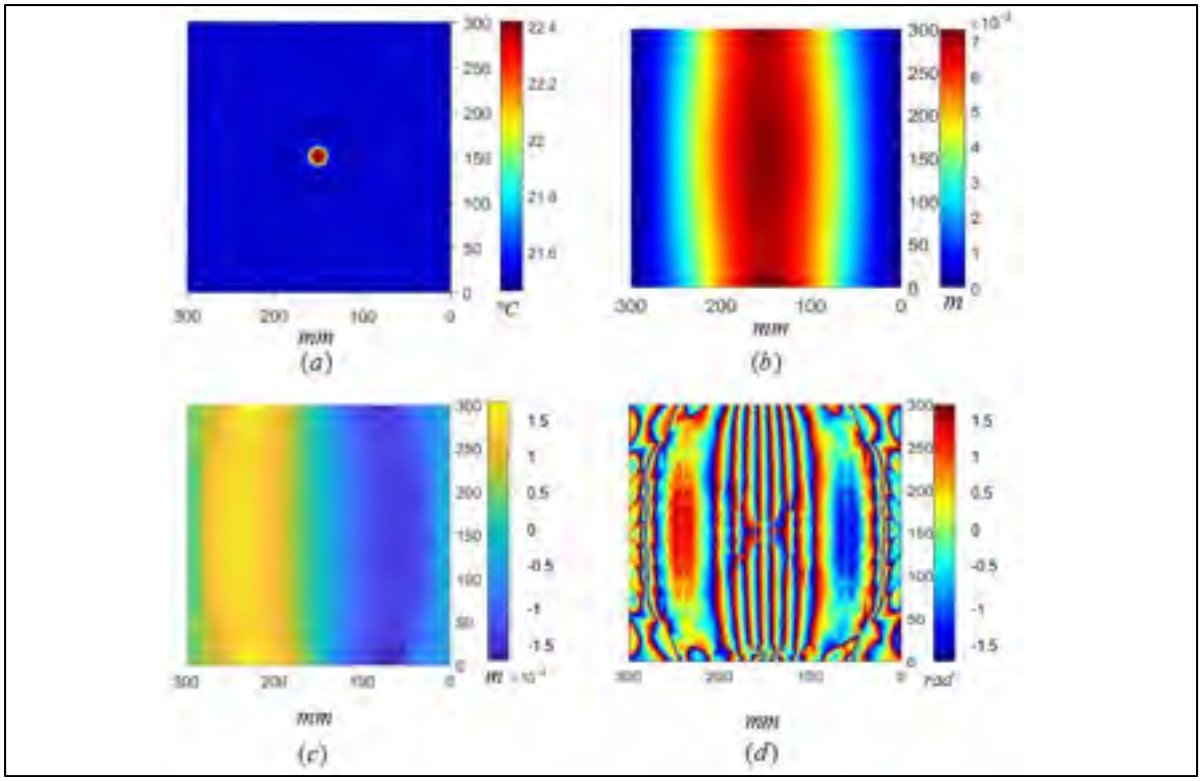

Figure 4-7 Procedure of simulating a phased shearogram, (a) thermogram after applying a thermal pulse, (b) out-of-plane displacement map after deformation, (c) sheared version of the deformation map in the vertical direction, (d) wrapped phased shearogram

4.8 Shearography simulation result

Indication in a shearography test, fringe anomaly, is formed by the flaw's response to the applied load. It depends on flaw nature, shape, size, location, and the conditions of applied load at the flaw's location. In this study, a model used to describe the response of the debonded area in a laminate panel, which is constrained at two edges.

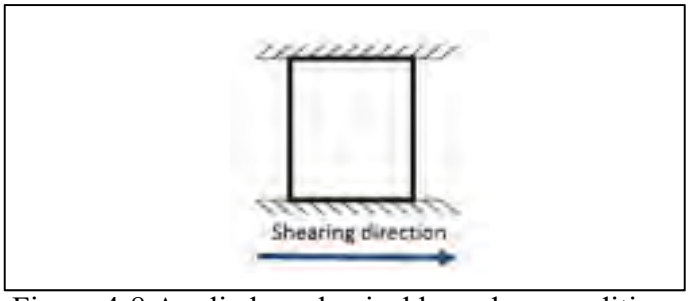

Figure 4-8 Applied mechanical boundary condition

When the thermal load is applied, the debonded area behaves as a plate under a deflection. Theoretically, The derivative map of the out of plane displacement looks in the form of a butterfly. In the deboned area, the size of the area is approximately equal to the size of the indication and the fringe density corresponds to the depth of the debonded area [81], [70], [86]. The simulation results, Fig. 4-9 to Fig. 4-11, show the indications of debond areas in various layers, 4th, 8th, and 12th. It should be noted that the one closest to the surface has the highest fringe density. In the phase shearograms, the phase is wrapped between $-\pi$ and π. The phase shearogram corresponds to the model are plotted where the shearing amount is 6 mm in the x-direction (horizontal direction). Defects in the fourth and eighth layers are detectable in the phase maps. Whereas the deepest defect, in the twelfth layer, is not revealed clearly. Fig. 4-12 to Fig. 4-14 display the shearogram for the defects in shear amount of 8 mm. They demonstrate the impact of the larger shear amount on detectability. The graphics are showing with a larger shearing amount, the detectability is improved at the defect position. However, the measuring result is more effected by information at both the defect and the sound area. Therefore, it makes locating and sizing of the defect more tricky.

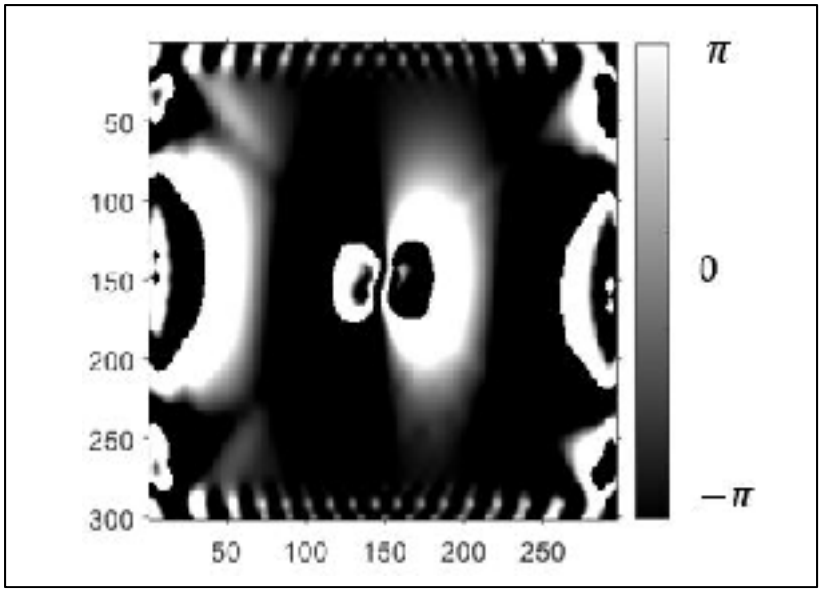

Figure 4-9 Fringe patterns depicting the deflection-derivatives of a rectangular plate clamped along its boundaries and subjected to square heat pulse, delamination is placed at 4th layer, it is sheared 6 mm in x-direction

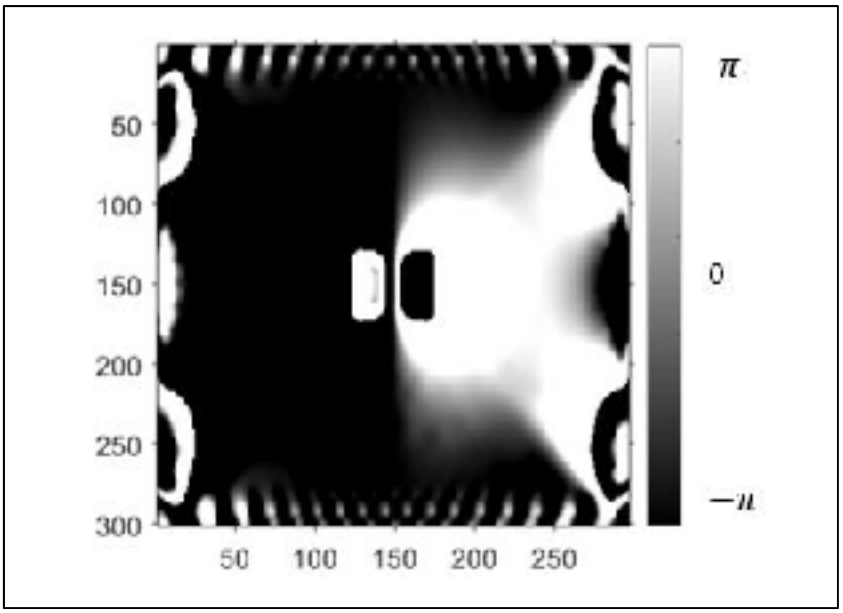

Figure 4-10 Fringe patterns depicting the deflection-derivatives of a rectangular plate clamped along its boundaries and subjected to square heat pulse, delamination is placed at 8th layer, it is sheared 6 mm in x-direction

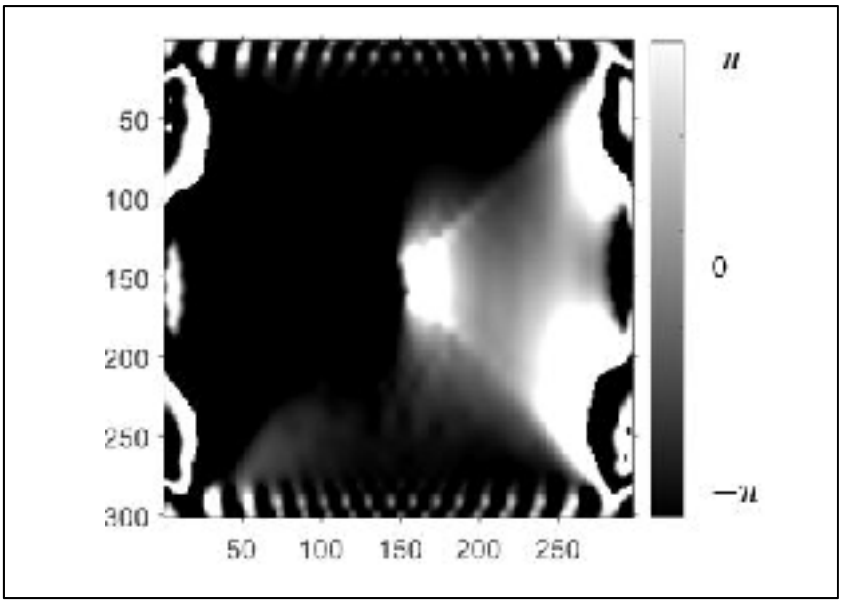

Figure 4-11 Fringe patterns depicting the deflection-derivatives of a rectangular plate clamped along its boundaries and subjected to square heat pulse, delamination is placed at 12th layer, it is sheared 6 mm in x-direction

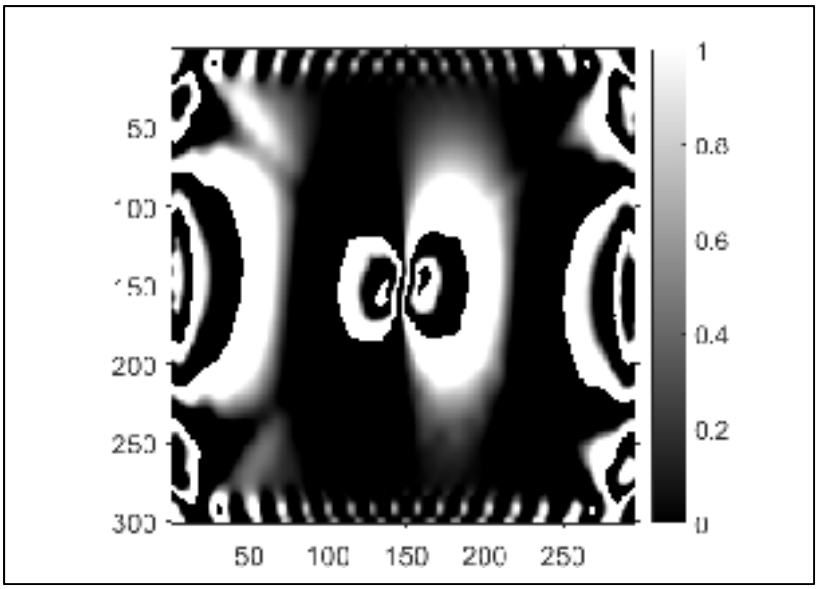

Figure 4-12 Fringe patterns depicting the deflection-derivatives of a rectangular plate clamped along its boundaries and subjected to square heat pulse, delamination is placed at 4th layer, it is sheared 8 mm in x-direction

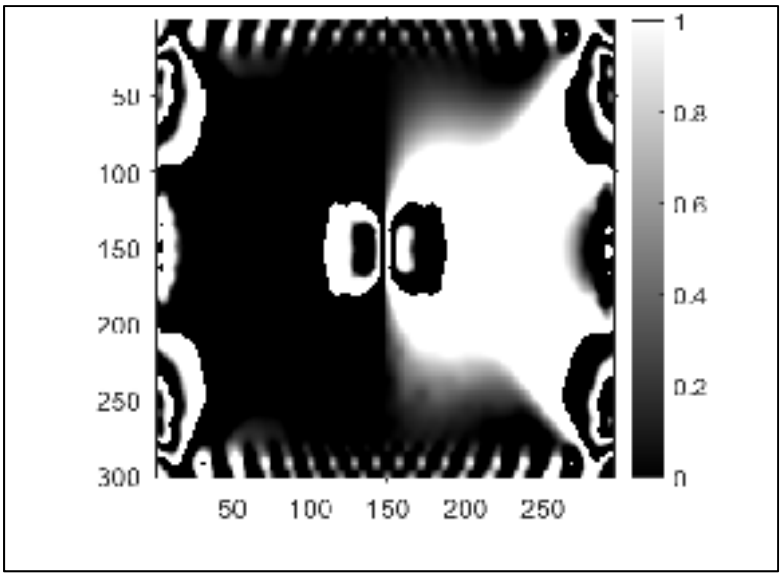

Figure 4-13 Fringe patterns depicting the deflection-derivatives of a rectangular plate clamped along its boundaries and subjected to square heat pulse, delamination is placed at 8th layer, it is sheared 8 mm in x-direction

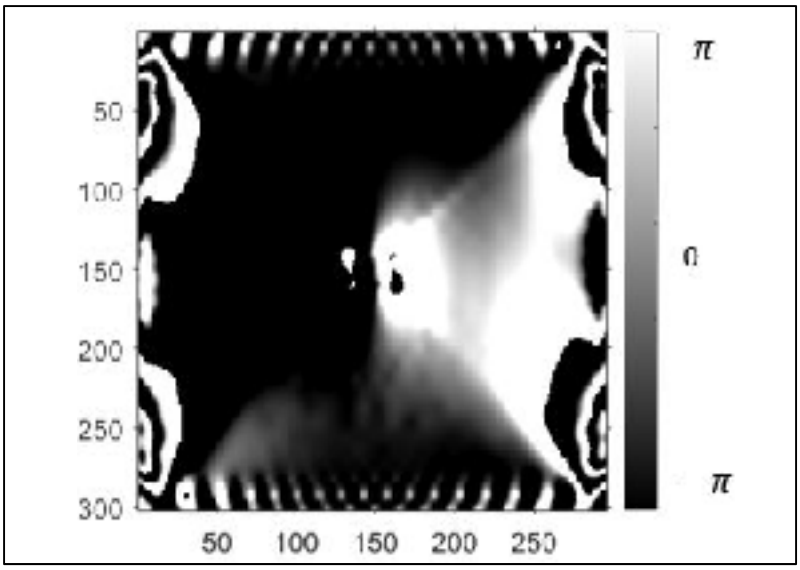

Figure 4-14 Fringe patterns depicting the deflection-derivatives of a rectangular plate clamped along its boundaries and subjected to square heat pulse, delamination is placed at 12th layer, it is sheared 8 mm in x-direction

CONCLUSION

CFRP has been increasingly used in aerospace structures owing to their mechanical properties. Low-velocity impact, a known cause of premature failure in aerostructures, is a typical damage scenario in CFRP. It is susceptible to cause transverse cracks, matrix cracks, and multiple interlaminar delamination. To reveal and evaluate this damage, adequate NDE methods are needed at different stages of fabrication, maintenance, and service.

In this thesis, three NDT methods were conducted to study their features in terms of detecting and sizing impact damaged area. The methods were applied to CFRP laminates with different levels of impact damage. The size and shape of the indications for each method had been investigated.

The complete understanding of the test's physics is a challenging task in the case of IRT and shearography testing. Therefore mathematical simulation was used to predict the indications and signals of real tests. This prediction has been applicable by analyzing the thermal and structural behaviour of the specimen in a virtual test.

The conclusion is, the applied techniques can be used as reliable methods to detect these levels of impact damages in the CFRP laminates. Conducting phase thermography and shearography led to the high-resolution images for all the damaged samples in a relatively fast process. In the case of shearography, the results showed, with the same size of impactor, the fringe density of the indications are proportional to the values of impact energy. This capability is a promising feature of shearography to evaluate the severity of impact damage.

Regarding the shape and the damage size, UT results have more visual detail about the shape of the defect. Although shearography sizing was closer to the UT results, phase thermography and shearography underestimated damage sizes with the full width of half amplitude sizing technique. It seems that the technique is not a precise method to size the impact damage for the two NDT methods.

Due to the difficulties in the analysis of the NDT signal in the composite material, FEM for signal prediction is conducted. The results showed that it can be an appropriate tool to provide effective defect detection procedures in the NDT methods. In this work, PPT simulation was conducted for the thermal signals. The results proved for a specific sampling frequency and

truncation window, the phase profiles have higher contrast for shallower delamination compared to the deeper ones. The next practice explained how the size of the truncation window, w, affects the results. The data illustrated that there is a loss of information related to the use of smaller w.

In the case of shearography, simulation results revealed that the closest delamination to the surface has the highest fringe density. Besides, with the increasing shearing amount, detectability is improved at the defect position. However, the measuring result can be affected by information at both the defect and the sound area. Therefore, using a higher shearing amount can decrease locating and sizing accuracy.

According to the experimental results, these techniques were able to detect the damages and measured their extents of the areas. In the measurement, there are differences in the indications' size values for each method. Therefore, in the future works, using criteria other than full-width of half-amplitude can be examined. Besides, microscopic images of damages can validate the results.

To possess a quantitative and more realistic simulation, in the future works, we will feed the real values of samples' material properties, and the test parameters to the mathematical model. In such a case, the estimation of the detection reliability as a function of size and shape is achievable. As a result, the simulation can be lead to the probability of detection (PoD) evaluation.

The other suggested study can be focused on is the quantitative shearography. It can be a precise tool to estimate the severity of impact damage. It would be applied in different component geometry and mechanical boundary conditions. Evaluating the technique needs to provide ideal test conditions such as accurate mechanical boundary conditions and loadings.

Investigation on impact damage, which has an accidental morphology, requires numerous test specimens. In this regard, conducting the tests on a wide variety of damage sizes, shapes, and severities are necessary. Besides evaluating the impacted samples with different thicknesses and surface curvatures should be considered. As a matter of fact, the limitation in the variety of test samples is a factor that can affect the reliability of the test results.

LIST OF BIBLIOGRAPHICAL REFERENCES

[1] A. Miner and S. Jones, "Design , Testing , Analysis , and Material Properties of Carbon Fiber Reinforced Polymers," 2016.

[2] M. Kalanchiam and M. Chinnasamy, "Advantages of composite materials in aircraft structures," *World Acad. Sci. Eng. Technol.*, vol. 71, no. 11, pp. 597–601, 2012.

[3] M. E. Ibrahim, "Nondestructive evaluation of thick-section composites and sandwich structures: A review," *Compos. Part A Appl. Sci. Manuf.*, vol. 64, pp. 36–48, 2014.

[4] B. Kreculj, D., Rašuo, "Review of Impact Damages Modelling in Laminated Composite Aircraft Structures," *Tech. Gaz.*, vol. 20, no. 3, pp. 485–495, 2013.

[5] Z. Zhang and M. Richardson, "Nondestructive Testing of Composite Materials," *Handb. Multiph. Polym. Syst.*, vol. 1, pp. 777–796, 2011.

[6] J. Baaran, "Visual Inspection of Composite Structures EASA-Research Project/2007/3 Final Report," 2009.

[7] T. W. Shyr and Y. H. Pan, "Impact resistance and damage characteristics of composite laminates," *Compos. Struct.*, vol. 62, no. 2, pp. 193–203, 2003.

[8] D. Kreculj and B. Rašuo, "Review of Impact Damages Modelling in Laminated Composite Aircraft Structures," vol. 3651, pp. 485–495, 1848.

[9] H. Kim, "Impact damage formation on composite aircraft structures," *Fed. Aviat. Adm. JAMS 2012 Tech. Rev. Meet.*, pp. 1–58, 2012.

[10] A. J. F. A. T. F. Der and G. D. O. Atf, "Boeing Composite Airframe Damage Tolerance and Service Experience."

[11] F. Léonard, J. Stein, C. Soutis, and P. J. Withers, "The quantification of impact damage distribution in composite laminates by analysis of X-ray computed tomograms," *Compos. Sci. Technol.*, vol. 152, no. 2017, pp. 139–148, 2017.

[12] R. H. Bossi, *ASNT Industry Handbook: Aerospace NDT*, 1st ed. American Society for Nondestructive Testing., 2014.

[13] C. J. Hellier, *HANDBOOK OF NONDESTRUCTIVE EVALUATION*, no. c. McGRAW-HILL.

[14] "The impedance method of non-destructive inspection," *NDT Int.*, vol. 17, no. 2, pp. 59–65, 1984.

[15] G. De Angelis, M. Meo, D. P. Almond, S. G. Pickering, and S. L. Angioni, "A new technique to detect defect size and depth in composite structures using digital shearography and unconstrained optimization," *NDT E Int.*, vol. 45, no. 1, pp. 91–96, 2012.

[16] S. K. Dwivedi, M. Vishwakarma, and P. A. Soni, "Advances and Researches on Non Destructive Testing: A Review," *Mater. Today Proc.*, vol. 5, no. 2, pp. 3690–3698, 2018.

[17] T. Nishida, T. Shiotani, H. Asaue, and A. Sagradyan, "Czech Society for Nondestructive Testing 32 nd European Conference on Acoustic Emission Testing Tomography Algorism Based on Excited Elastic Wave," no. November, pp. 353–362, 2016.

[18] K. Koyama, H. Hoshikawa, and G. Kojima, "Eddy Current Nondestructive Testing for Carbon Fiber- Reinforced Composites," *J. Press. Vessel Technol.*, vol. 135, no. 4, p. 041501, 2013.

[19] S.Gholizadeh, "A review of non-destructive testing of composite materials," *NDT Int.*, vol. 15, no. 2, pp. 75–86, 2016.

[20] Q. Shen, M. Omar, and S. Dongri, "Ultrasonic NDE Techniques for Impact Damage Inspection on CFRP Laminates," *J. Mater. Sci. Res.*, vol. 1, no. 1, pp. 1–16, 2011.

[21] M. H. Sherafat, N. Quaegebeur, P. Hubert, L. Lessard, and P. Masson, “Experimental Model of Impact Damage for Guided Wave-Based Inspection of Composites,” *J. Nondestruct. Eval. Diagnostics Progn. Eng. Syst.*, vol. 1, no. 4, p. 040801, 2018.
[22] J. W. Newman, “Aerospace NDT with Advanced Laser Shearography ,” *17th World Conf. Nondestruct. Test.*, p. 6, 2008.
[23] F. W. Spencer, “Visual Inspection Research Project Report on Benchmark Inspections. U.S. Department of Transportation, Federal Aviation Administration,” no. September, 1996.
[24] A. M. Amaro, P. N. B. Reis, M. F. S. F. De Moura, and J. B. Santos, “Damage detection on laminated composite materials using several NDT techniques,” *Insight Non-Destructive Test. Cond. Monit.*, vol. 54, no. 1, pp. 14–20, 2012.
[25] Y. Y. Hung, “Shearography: A New Optical Method For Strain Measurement And Nondestructive Testing,” *Opt. Eng.*, vol. 21, no. 3, 1982.
[26] H. Fernandes, C. Ibarra-Castanedo, H. Zhang, and X. Maldague, “Thermographic Non-destructive Evaluation of Carbon Fiber-Reinforced Polymer Plates After Tensile Testing,” *J. Nondestruct. Eval.*, vol. 34, no. 4, pp. 1–10, 2015.
[27] M. P. G. R. Dubé, L. Scheed, J. Lewandowski, L. Mouret, “Comparison of Three Ndt Techniques for the Inspection of Aeronautic Composite Structures,” pp. 3–4.
[28] A. D. P. and P. W., “Thermal imaging of composites,” *J. Microsc.*, vol. 201, no. 2, pp. 163–170, 2001.
[29] S. G. P. Darryl P. Almond, Stefano L. Angioni, “Research on Embedded JavaScript Interpreter,” *J. Converg. Inf. Technol.*, vol. 7, no. 11, pp. 150–158, 2012.
[30] V. Vavilov, A. Chulkov, A. Smotrov, S. Smotrova, and A. Moskovchenko, “Characterizing impact damage in GFRP/CFRP composites by determining thermal effusivity/diffusivity,” *Meas. Sci. Technol.*, vol. 30, no. 3, p. ab018e, 2019.
[31] C. Ibarra-Castanedo and X. P. Maldague, “Defect depth retrieval from pulsed phase thermographic data on Plexiglas and aluminum samples,” *Thermosense XXVI*, vol. 5405, no. May, p. 348, 2004.
[32] S. Pawlak, “Application of IR Thermography with Thermal Diffusivity Analysis for Detection of Plies Displacement in CFRP Composites,” *J. Mater. Eng. Perform.*, vol. 27, no. 12, pp. 6545–6551, 2018.
[33] and X. M. L.-D. Théroux, J. Dumoulin, “Square Heating Applied to Shearography and Active Infrared Thermography Measurements Coupling: From Feasibility Test in Laboratory to Numerical Study of Pultruded CFRP Plates Glued on Concrete Specimen,” *Strain*, vol. 50, no. 5, pp. 389–403, 2014.
[34] X. P. Maldague, “Introduction to NDT by Active Infrared Thermography,” *Mater. Eval.*, vol. 6, no. 9, pp. 1060–1073, 2002.
[35] A. M. Koshti, “NORMALIZED TEMPERATURE CONTRAST PROCESSING IN INFRARED FLASH THERMOGRAPHY,” 2019.
[36] P. Venegas *et al.*, “Image and Data Processing Techniques Applied to Infrared Thermographic Non- Destructive Inspections of Aeronautical Composite Components,” *4th Int. Symp. NDT Aerosp.*, pp. 1–8, 2012.
[37] V. P. Vavilov and D. D. Burleigh, “Review of pulsed thermal NDT: Physical principles, theory and data processing,” *NDT E Int.*, vol. 73, pp. 28–52, 2015.
[38] Y. H. Huang, S. P. Ng, L. Liu, C. L. Li, Y. S. Chen, and Y. Y. Hung, “NDT&E using shearography with impulsive thermal stressing and clustering phase extraction,” *Opt. Lasers*

Eng., vol. 47, no. 7–8, pp. 774–781, 2009.
[39] Y. Y. Hung, L. X. Yang, and Y. H. Huang, "Non-destructive evaluation (NDE) of composites: Digital shearography," *Non-Destructive Eval. Polym. Matrix Compos. Tech. Appl.*, pp. 84–115, 2013.
[40] A. Davis, "Recent developments in simulation," p. 318, 2002.
[41] "IIW-2363-Simulation-of-NDT.pdf." .
[42] J. Dumoulin, X. Maldague, C. De Beaulieu, and A. I. Thermography, "Applied To Ndt of Reinforced Concrete Structure By Glued Cfrp," pp. 88–95, 2014.
[43] L. Théroux, J. Dumoulin, and X. Maldague, "Thermography and Shearography coupling applied to NDT of CFRP tissue bonding interface on concrete by numerical simula- tions," no. 1, pp. 11–16.
[44] D. Buchta, C. Heinemann, G. Pedrini, C. Krekel, and W. Osten, "Combination of FEM simulations and shearography for defect detection on artwork," *Strain*, vol. 54, no. 3, pp. 1–11, 2018.
[45] F. Mabrouki, M. Genest, G. Shi, and A. Fahr, "Numerical modeling for thermographic inspection of fiber metal laminates," *NDT E Int.*, vol. 42, no. 7, pp. 581–588, 2009.
[46] *www.boeing.com/commercial/aeromagazine/articles/qtr_4_06/article_04_2.html*. .
[47] T. Herrera Marcano, A. Cachada, T. Rocha-santos, A. C. Duarte, and N. Roongtanakiat, "Visual Inspection Rrelaiability for Composite Aircraft Structure," 2009.
[48] P.-C. OSTIGUY *et al.*, "Selection of Structural Features for the Systematic Study of Guided Wave Propagation and Interaction with Damage," no. January, 2015.
[49] S. Te, "Back to Composite Standards," *ASTM Int. Des. D*, vol. i, no. C, pp. 4–6, 2011.
[50] M. A. G. RODRIGO, "the Ultrasonic Pulse-Echo Immersion Technique and Attenuation Coefficient of Particulate Composites," *Thesis-matlab*, 2013.
[51] P. A. Meyer, J. W. Anderson, and K. Branson, "www.NDT.net." .
[52] "https://www.olympus-ims.com."
[53] O. A. Ali Khademi Far, Martin Viens1, Hakim Bendada, Louis-Daniel Théroux, "Non-destructive evaluation of impact damage in carbon fibre reinforced polymer using infrared thermography, shearography and ultrasonic testing," in *NDT in Canada*, 2019.
[54] C. Ibarra-Castanedo, J. R. Tarpani, and X. P. V. Maldague, "Nondestructive testing with thermography," *Eur. J. Phys.*, vol. 34, no. 6, 2013.
[55] C. Ibarra-Castanedo *et al.*, "Infrared thermography: principle and applications to aircraft materials," *Nondestruct. Test. J.*, 2008.
[56] Haydar Abdolnabi Thajeel, "Numerical modeling of infrared techniques via ANSYS," Missoury University, 2014.
[57] S. Marinetti, Y. A. Plotnikov, W. P. Winfree, and A. Braggiotti, "Pulse phase thermography for defect detection and visualization," pp. 1–9.
[58] R. S. Allison, J. M. Johnston, G. Craig, and S. Jennings, "Airborne optical and thermal remote sensing for wildfire detection and monitoring," *Sensors (Switzerland)*, vol. 16, no. 8, 2016.
[59] S. S. D. Hamamatsu Photonics K.K, "Characteristics and use of infrared detectors," *Small*, p. 43, 2004.
[60] C. Ibarra-Castanedo, J. R. Tarpani, and X. P. V. Maldague, "Nondestructive testing with thermography," *Eur. J. Phys.*, vol. 34, no. 6, 2013.
[61] D. A. Derusova, V. P. Vavilov, and S. S. Pawar, "Evaluation of equivalent defect heat generation in carbon epoxy composite under powerful ultrasonic stimulation by using infrared

thermography," *IOP Conf. Ser. Mater. Sci. Eng.*, vol. 81, no. 1, 2015.
[62] C. Ibarra-castanedo *et al.*, "Thermographic nondestructive evaluation: overview of recent progress," *Thermosense Proc. SPIE Vol. 6939*, no. April 2003, 2003.
[63] C. Ibarra-Castanedo and X. Maldague, "Pulsed phase thermography reviewed," *Quant. Infrared Thermogr. J.*, vol. 1, no. 1, pp. 47–70, 2007.
[64] V. P. Vavilov and D. D. Burleigh, "Review of pulsed thermal NDT: Physical principles, theory and data processing," *NDT E Int.*, vol. 73, pp. 28–52, 2015.
[65] S.-O. Gnessougou, N. Poulin, C. Ibarra-Castanedo, X. Maldague, A. de Champlain, and É. Robert, "Thermal Diffusivity Measurements With Flash Method at Different Depths In a Burned Composite Material," no. January, 2018.
[66] M. T. Klein, C. Ibarra-Castanedo, X. P. V. Maldague, and A. Bendada, "A straightforward graphical user interface for basic and advanced signal processing of thermographic infrared sequences," *Thermosense XXX Proc. SPIE Vol. 6939*, vol. 6939, p. 9, 2008.
[67] S. S. Pawar and K. Peters, "Through-the-thickness identification of impact damage in composite laminates through pulsed phase thermography," *Meas. Sci. Technol.*, vol. 24, no. 11, 2013.
[68] H. Zhang *et al.*, "Thermographic Non-Destructive Evaluation for Natural Fiber-Reinforced Composite Laminates," *Appl. Sci.*, vol. 8, no. 2, p. 240, 2018.
[69] ASTM, "E2582-07 Standard Practice for Infrared Thermography of Composite Panels and Repair Patches used in Aerospace Applications," *ASTM Int.*, vol. i, no. July, pp. 1–6, 2014.
[70] Y. Y. Hung and H. P. Ho, "Shearography: An optical measurement technique and applications," *Mater. Sci. Eng. R Reports*, vol. 49, no. 3, pp. 61–87, 2005.
[71] A. Zambrano Leal, "Sociedad de control y profesión docente. Las imposturas de un discurso y la exigencia de una nueva realidad," *Antimicrob. Agents Chemother.*, vol. 53, no. 95, pp. 45–52, 2012.
[72] "In Reply: BEHAVIOUR THERAPY," *Br. J. Psychiatry*, vol. 111, no. 479, pp. 1009–1010, 1965.
[73] D. Francis, R. P. Tatam, and R. M. Groves, "Shearography technology and applications: A review," *Meas. Sci. Technol.*, vol. 21, no. 10, 2010.
[74] L. X. Y. and Y. Y. Hung, "Digital Shearography for Nondestructive Evaluation and Application in," no. 248.
[75] D. Francis, D. Masiyano, J. Hodgkinson, and R. P. Tatam, "A mechanically stable laser diode speckle interferometer for surface contouring and displacement measurement," *Meas. Sci. Technol.*, vol. 26, no. 5, pp. 1–7, 2015.
[76] Y. Y. H. and L. X. YANG, *Non-destructive evaluation (NDE) of composites: digital shearography*, no. 1. Elsevier Ltd, 2013.
[77] W. Steinchen, L. Yang, and L. X. Yang, *Digital Shearography: Theory and Application of Digital Speckle Pattern Shearing Interferometry*. SPIE-International Society for Optical Engineering, 2003.
[78] W. Steinchen, L. Yang, and L. X. Yang, *Digital Shearography: Theory and Application of Digital Speckle Pattern Shearing Interferometry*. 2007.
[79] E. Corso Krutul and R. M. Groves, "Opto-mechanical modelling and experimental approach to the measurement of aerospace materials using shearography and thermal loading," *Model. Asp. Opt. Metrol. III*, vol. 8083, p. 80831C, 2011.
[80] Y. Li, W. Zhang, Z. W. Yang, J. Y. Zhang, and S. J. Tao, "Low-velocity impact damage characterization of carbon fiber reinforced polymer (CFRP) using infrared thermography,"

Infrared Phys. Technol., vol. 76, pp. 91–102, 2016.
[81] X. Chen, "Computational and Experimental Approach for Non-destructive Testing by Laser Shearography," 2014.
[82] R. Joven, R. Das, A. Ahmed, P. Roozbehjavan, and B. Minaie, "Thermal properties of carbon fiber-epoxy composites with different fabric weaves," *Int. SAMPE Tech. Conf.*, no. January 2012, 2012.
[83] M. De Freitas and L. Reis, "Failure mechanisms on composite specimens subjected to compression after impact," *Compos. Struct.*, vol. 42, no. 4, pp. 365–373, 1998.
[84] K. M. Fard, A. Sayyidmousavi, Z. Fawaz, and H. Bougherara, "Finite element buckling analysis of laminated composite sandwich panels with transversely flexible core carrying attached elastic strip," *J. Sandw. Struct. Mater.*, vol. 14, no. 6, pp. 715–733, 2012.
[85] and X. M. L.-D. Théroux, J. Dumoulin, "Square Heating Applied to Shearography and Active Infrared Thermography Measurements Coupling: From Feasibility Test in Laboratory to Numerical Study of Pultruded CFRP Plates Glued on Concrete Specimen," *Strain*, vol. 50, no. 5, pp. 389–403, 2014.
[86] E. Corso Krutul and R. M. Groves, "Opto-mechanical modelling and experimental approach to the measurement of aerospace materials using shearography and thermal loading," *Model. Asp. Opt. Metrol. III*, vol. 8083, no. May 2011, p. 80831C, 2011.
[87] R. Gondaliya, "Improving Damage Tolerance of Composite Sandwich Structure Subjected to Low Velocity Impact Loading : Experimental Analysis Paper Number : 1510 Title : Improving Damage Tolerance of Composite Sandwich Structure Subjected to Low Velocity Impact Loading : E," no. September, 2016.